

Source-dependent variations of M7 earthquakes in the Los Angeles Basin

Dissertation
von
Haijiang Wang

der Fakultät für Geowissenschaften
Ludwig-Maximilians-Universität München

April 2007

Erstgutachter: Prof. Heiner Igel

Zweitgutachter: PD Dr. Gert Zoeller, University of Potsdam

Tag der mündlichen Prüfung:

Zusammenfassung

Deterministic earthquake scenario simulations are playing an increasingly important role in seismic hazard and risk estimation. The numerical calculation of the complete 3D wavefield in the observed frequency band for a seismically active basin remains a computationally expensive task. This expense restricts seismologists either to calculating source models with homogeneous media (e.g., Gallovič and Brokešová, 2004, 2007a,b), or to calculating single source scenario in 3D media (e.g., Olsen and Archuleta, 1996; Olsen, 2000; Ewald et al., 2006) while the complex effects of the media and the source on the ground motion are getting more and more attention. At the same time, with the development of the instrument, ground rotation introduced by an earthquake becomes a more and more important topic. Our aim is to provide a tool with which we can calculate a large number of different finite-source scenarios for a particular fault or fault system located in a 3D structure which will enable us to estimate ground motion (translation and rotation) variations due to source and 3D structure. In order to avoid having to run numerical expensive 3D code for each kinematic source scenario we propose the concept of “numerical Green’s functions” (NGF): a large seismic fault is divided into sub-faults of appropriate size for which synthetic Green’s functions at the surface of the seismically active area are calculated and stored. Consequently, ground motions from arbitrary kinematic sources can be simulated for the whole fault or parts of it by superposition.

To demonstrate the functionalities of the method a strike-slip NGF data base was calculated for a simplified vertical model of the Newport-Inglewood fault in the Los Angeles basin. As a first example, we use the data base to estimate variations of surface ground motion (e.g., peak ground velocity (PGV)) due to hypocentre location for a given final slip distribution. The results show a complex behavior, with dependence of absolute PGV and its variation on asperity location, directivity effect and local under-surface structure. Hypocentral depth may affect peak ground velocity in a positive or negative way depending on the distance from the fault and the receiver location with respect to basin structure.

Finite-fault source inversions reveal the spatial complexity of earthquake slip over the fault plane. In this study, several possible earthquake scenarios of Mw 7.0 are simulated with different quasi-dynamic finite source models for the Newport-Inglewood fault in the Los Angeles basin. We investigate the effects of the various slip histories on peak ground velocities and the related variations in ground motion prediction for our study area. The results confirm that the fault perpendicular components of motion are dominated by directivity effects while the fault parallel component is influenced both by the slip distribution and the basin structure.

There are theoretical considerations suggesting that observations/calculations of the rotation part of earthquake-induced ground motions may provide additional information for earthquake risk hazard analysis after reports on rotational effects on structures (like twisting of tombstones or statues). For the first time, we carry out a systematic study of earthquake scenario simulations in 3D media with a specific focus on the rotational part of the motions.

We simulate several M7 earthquakes with various hypocentre locations and slip histories on the Newport-Inglewood fault embedded in the 3D Los Angeles Basin. We investigate source and basin structure effects on the rotational components of ground motion (e.g., peak ground rotation rates and their variation, horizontal gradients) and compare with the effects on translations.

Igel et al. (2005) shows a similarity of the observed waveforms between transverse acceleration and the vertical rotation rate in the teleseismic range benefiting from the recently developed ring laser instruments. The vertical rotation rate is found to be surprisingly similar to the horizontal translations in waveform which is explained with the plane wave propagation in the global range. That condition could not hold any more in the near-field range, but some information could be extracted from the comparison between the translations and the rotation rate. As a final application, we investigate the source-dependent variations on rotational ground motions and compare with the results for translations.

The thesis is structured as follows:

Chapter 1: An insight into the present standard procedures carried out in the Seismic Hazard Assessment (SHA) is shown and then the different methodologies for predicting ground motions are described and compared, which are working individually or cooperate with each other. In recent years, one of those methods – deterministic calculations have been used widely and its consumption both in terms of CPU time and memory motivated the development of one new tool. We name that tool Numerical Green’s Function (NGF) method.

Chapter 2: An introduction to the different solutions of the wave propagation is given and the state-of-the-art technologies are described. We will introduce in detail the techniques adopted. We show how to implement the source, how to solve the wave propagation problem, and how to efficiently absorb the energies outgoing from the working area, or reflect them at the free surface boundary. To correctly account for the rupture process, which has been found to be the most important contributor to the ground motion in the near-source region, different tools are developed which can be divided into two groups: kinematic description and dynamic description of the source. These two descriptions are briefly compared. Then we focus on the “quasi-dynamic” method developed by Guatteri et al. (2004) which combines, to some extent, the two different approaches. This method is used to provide us the rupture processes we will consider.

Chapter 3: Green’s function stands for the response on the surface due to an impulse dislocation at the source. A large earthquake rupture can be represented with a group of impulse dislocations, and thus the ground motion on the surface can be achieved by the superposition of its Green’s functions. In this chapter, we follow the representation theorem published in Aki and Richards (2002) to give the theoretical basis of that method and briefly describe the two groups of that method: composite method and integral method. Finally we introduce our new method – Numerical Green’s Function, present the basic equations and analyze its relationship with the representation theorem and empirical Green’s function method.

Chapter 4: Discretization of the fault plane into elements and assumption the source parameters identical inside each element will introduce errors in the calculated seismic motions

and these errors are expected to depend on some few parameters such as the fault geometry, the rupture velocity, the sub-fault size, the cut-off frequency for low-pass filtering the ground motions, the directivity effect, etc.. In this chapter we design a hypothetical velocity structure and investigate how the errors introduced by the fault discretization will change with those parameters. The results are considered to provide some clues for our next step – selecting a seismic active fault and discretizing it into pieces with optimal sizes for which the Green's functions will be calculated and stored.

Chapter 5: The working area of this study, the Newport Inglewood fault embedded in the Los Angeles basin is introduced. The Los Angeles basin is chosen as our working area because of the high seismicity and that the most reliable information about the subsurface structure could be achieved. One active fault, the Newport-Inglewood fault inside this region is considered as a possible place where an M7.4 earthquake could happen in the future decades. Also its near vertical straight fault plane facilitates the implementation of this fault into the finite difference method. After choosing the fault and velocity structure, we re-address the optimal size of sub-fault by simulating a few M7 earthquakes and investigate the peak ground velocity and the waveform difference introduced by the different discretizations.

The importance of the directivity effect on the ground motion in the near-source region has been recognized and is one of the main targets of the next generation of the attenuation relationship. A brief introduction to the physics of wave propagation is given in order to make the following discussions and illustrations of our results understandable for readers without previous knowledge. We analyze the different directivity effect supposed to happen between different component, or different kinds of motion (translation and rotation).

Chapter 6: This chapter addresses the problem of the variations of surface ground motion (e.g., peak ground velocity) due to hypocentre location for a given final slip distribution. A complex behavior about the dependence of absolute PGV and its variation on asperity location, directivity effect and local structure is presented. Hypocentral depth may affect PGV in a positive or negative way depending on the distance from the fault and the location with respect to the basin structure. The directivity effect is found to control the seismic motion generation for a specific final slip distribution.

Chapter 7: Inversions of the spatial and temporal evolution of earthquake slip on fault planes provide compelling evidence that fault displacement is spatially variable at all resolvable scales. Investigations of strong ground motion also indicate the spatial variability of the rupture velocity. This source physics complexity appeals for thorough description of the source process when calculating seismic motion. The method developed before hand allows efficient simulation of arbitrary slip histories. In this chapter, we investigate how the various slip histories affect peak ground velocities and the related variations in ground motion prediction for our study area. The fault perpendicular components of motion are confirmed to be dominated by directivity effects while the fault parallel component is influenced both by the slip distribution and the basin structure.

Chapter 8: The rotational motions excited by earthquakes are believed to be capable of providing more information for the aim of earthquake hazard analysis. But to the present

time, those information are hard to be acquired. The first reason is that the spacing of the accelerograph recording sites is too large to get the indirect rotational motion measurement from the accelerograph recordings. The second reason is that the small amplitude of the rotational motion is beyond the recording capability of the present instruments. At the present time, the answers lie in the numerical simulation. In this section, for an M7.0 earthquake which is considered to happen on the Newport-Inglewood fault embedded in the Los Angeles basin, different parameters responsible for the ground rotation variation, like the hypocentre location, directivity effect and slip history, are systematically investigated.

In the teleseismic range where plane wave assumption can be made, [Igel et al. \(2005\)](#) investigates the relationship between the translation and the rotation in terms of the amplitude ratio and waveform similarity. In this section, we find the waveform similarity between one horizontal acceleration and the vertical rotation rate even in the near-source region. We also calculate the amplitude ratio between the acceleration and the rotation rate and compare the results with the medium properties. That ratio is found to be somehow correlative to the basin depth.

Chapter 9: The most important results in this work are briefly summarized. Future promising prospectives are also described.

Appendix A: The individual peak ground velocity distributions corresponding to the varying hypocentres of the grid presented in chapter 6 are presented as a table for better illustration in case of interest. Three components of velocity and rotation rates are summarized here.

Appendix B: The peak ground velocity distributions are grouped into different tables corresponding to the varying slip histories (chapter 7). Three components of velocity and rotation rate are summarized here.

Acknowledgments

Deep thanks go to my advisor Prof. Heiner Igel. Heiner was an inspiring example of a student advisor: patiently answering a never ending stream of questions, encouraging when progress was slow, shaving off the worries of funding, being approachable anytime even during the holiday, providing financial supports for bench of international workshops. I received much good advice from, František Gallovič, Alain Cochard and Michael Ewald both in the field of seismology and Numerical tools and their great contributions to the work in this thesis. I want to thank my colleague members Markus Treml, Gilbert Brietzke, Bernhard Schubert, Toni Kraft, Wiwit Suryanto and Peter Daneck for their encouraging interest in my work, their numerous comments and critiques they expressed in our regular group meetings. Special thanks go to Erika Vye for thorough help about how to survive in Muenchen.

I am indebted to Gert Zöller (Institute of Physics and Institute of Mathematics, University of Potsdam, Potsdam, Germany) for his instructive knowledge in the dynamic rupture modeling. I greatly benefited from his insight and expertise in rupture physics.

Financial support during my first two years at Muenchen was provided by the International Quality Network Georisk Project (IQN), awarded by Deutscher Akademischer Austausch Dienst (DAAD). My research was also funded by the Elite Netzwerk Bayern through the THESIS Graduate College and the SPICE (Seismic wave Propagation and Imaging in Complex media), a joint program institutes throughout Europe.

Contents

1	Introduction	1
1.1	Standard Methods for Ground Motion Simulation	1
1.1.1	Attenuation Relationships	2
1.1.2	Stochastic Method	3
1.1.3	Deterministic Method	4
1.2	Motivation and Plot	4
2	Methodology	6
2.1	3D Staggered-Grid Finite-Difference Scheme	6
2.1.1	Temporal Extrapolation and Derivation	7
2.1.2	Double Couple Point Source Implementation	9
2.1.3	Free Surface Boundary	9
2.1.4	Perfectly Matched Layer Boundary	10
2.2	Rupture Process	11
2.3	Conclusions	14
3	Numerical Green’s Function Method	15
3.1	Representation Theorem	15
3.2	Empirical Green’s Functions	16
3.2.1	Composite Method	17
3.2.2	Rupture parameter	17
3.3	Numerical Green’s Function	18
3.4	Discussion	19
4	Synthetic Tests – Benchmarking	21
4.1	Parameter Studies – Homogeneous Case	21
4.1.1	Directivity Effect	27
4.1.2	Rupture Velocity	28
4.1.3	Cut-off Frequency	28
4.1.4	Sub-fault Size	29
4.2	Conclusions and Hints to the Future Work	29
5	NGF Data-Base	31
5.1	Los Angeles Basin	31
5.2	Newport-Inglewood Fault	33
5.3	Verification: Heterogeneous Medium	35
5.4	Near-Source Wave Propagation Physics	39

5.4.1	Velocity	39
5.4.2	Rotation	41
5.5	Conclusions	42
6	Application: Hypocentre Location Effect	44
6.1	Introduction	44
6.2	Seismogenic Zone	45
6.3	Set up	45
6.4	Velocity Snapshots	46
6.5	Two Hypocentre Examples	46
6.6	Inter-event Variations of Ground Motion	50
6.7	Comparison with the Empirical Results	53
6.8	Conclusions	57
7	Application: Slip History Effect	59
7.1	Introduction	59
7.2	Slip Histories	60
7.3	Average PGV Characteristics	61
7.4	Source Dependent PGV Variations	63
7.5	Discussions and Conclusions	66
8	Application: Rotation Rate	68
8.1	Introduction	68
8.2	Verification	70
8.3	Effect due to Hypocentre Location	70
8.3.1	Two Examples	72
8.3.2	Inter-event Variations of Rotation Rate	72
8.3.3	Rotation Rate Variations in the Near-Source Region	77
8.3.4	Relationship between PGRR and Source Depth	78
8.4	Slip History Effect	80
8.4.1	Average PGRR Characteristics	80
8.4.2	Source Dependent PGRR Variations	82
8.5	Comparison with Translations	85
8.5.1	Seismogram Profiles	85
8.5.2	Waveform Similarity	88
8.5.3	Amplitude Ratio and Medium Parameter	88
8.5.4	Peak Ground Acceleration Distribution	91
8.5.5	Decay with Fault Distance	94
8.6	Conclusions	94
9	Conclusions and Discussions	98
A	Peak Ground Motions: Varying Hypocentre	103
B	Peak Ground Motions: Varying Slip History	110
	List of Tables	117

List of Figures

119

References

130

Chapter 1

Introduction

1.1 Standard Methods for Ground Motion Simulation

Earthquakes are hazardous primarily because the induced strong ground shaking destroys things that people have constructed – buildings, transportation lifelines, and communication systems. Over the last century, earthquakes have caused economic losses up to hundreds of billions of dollars. And despite the continuing improvements in building codes and structural design, the annualized long-term loss due to earthquakes appears to be rising rapidly, near-exponentially. Resolving such issues illustrates the need for coordinated planning across all aspects of seismic safety. To facilitate planning, understandable earthquake information must be made available to a wide range of professionals.

Engineering considerations of earthquakes are the earthquake load and safety of engineering structures against it. Before the occurrence of an earthquake, engineers need to know the possibility of a certain strength and repetition rate of ground motion occurring at a site, the dynamic properties and strength of the engineering structures in order to design future structures safely and economically, and the possible behavior of existing structures if such an earthquake occurs and the necessary measures that should be taken. The process of evaluating the design parameters of earthquake ground motion at the engineering site is called seismic hazard assessment (SHA). The safety of an engineering structure is controlled by both the strength of earthquake motion and the seismic capacity of the engineering structure. Seismicity of a region is controlled by two factors: the stress and strain field from plate-tectonic movement and the strength and deformation capacity of the crust medium where the earthquake occurs.

The SHA usually consists of the following steps:

1. Determine the seismic province or belts where future earthquakes may occur according to the seismicity.
2. Determine the parameters of seismicity for each province and source.
3. Select the parameters for seismic hazard (peak acceleration, response spectrum and intensity) and determine their attenuation laws suitable for the region.
4. Determine the seismic hazard at the sites.

Several methods are employed during the SHA process which are described in the following, respectively.

1.1.1 Attenuation Relationships

It is generally agreed that, for the safety of structures, characteristics of the strong ground motion may be represented by three basic elements: amplitude, spectrum and duration. The widely used approach is to evaluate directly the ground motion values from an attenuation relationship between the ground motion and the source (usually magnitude) and propagating medium (usually distance) obtained empirically from ground motion data. This attenuation relationship is regressed from the real observations. The advantage of this approach is its simplicity in physical idea and reliability, and the disadvantage is the lack of data (needed to retrieve the relations) for many regions in the world and the amplification inside a sedimentary basin is difficult to consider.

The first individual relationship between the epicentral acceleration a_0 at a period T_0 , the magnitude M and the distance R is obtained by [Gutenberg and Richter \(1956\)](#) for the southern California region as:

$$\begin{aligned}\log a_0 &= -2.1 + 0.81M - 0.027M^2, \\ a_R &= a_0 F_a, \\ F_a &= (1 + R/y_0)^n, \quad y_0 \text{ is taken as 48 km,} \\ n &= 1 + 1/(2.5T_p),\end{aligned}$$

where how the acceleration decays with the distance is fulfilled by the attenuation parameter F_a . [Kanai \(1961\)](#), for the first time, presented the simple attenuation relationship (peak acceleration a) represented by M and R as:

$$\log a = c_1 + c_2 M + c_3 \log R,$$

where c_n are the coefficients regressed from observations (which have the same meaning in the following equations in this section). In order to account for the saturation of ground motion in the epicentral region, [Milne and Davenport \(1969\)](#) included a magnitude term in the distance term, Δ , and presented their attenuation relationship as:

$$\log a = c_1 + c_2 M + (\log \Delta^2 + c_3 e^{c_4 M}),$$

where a is the peak acceleration. [Esteva \(1970\)](#) also found that the former attenuation relationships produced high acceleration, a , in the very small R region which didn't accord with the common knowledge that the ground motion should have an upper limit. Hence he suggested to add one constant R_0 into the distance term, R , to restrict the ground motion to be finite in the near-field region. Finally he presented the following equation:

$$\log a = c_1 + c_2 M + c_3 \log(R + R_0)$$

[Duke et al. \(1970\)](#) introduced the linear distance term into the attenuation relationship to account for the ground motion decay caused by the energy absorption during propagation through the earth. [Schnabel and Seed \(1973\)](#) confirms the results of Duke from the theoretical point of view. Duke's equation include the magnitude term, the energy decay by the geometrical expansion and the ground motion decay caused by the energy absorption in the earth and thus become the most popular model used in the field of seismic motion attenuation research.

In the last 80ies, the high frequency part of ground motion is found to be saturated in the near-field area by real observations. In this region, the part of the fault which is excited

during a large earthquake can not be considered as a point any more. From the point of view of the energy superposition, in this region, the main contributor to the ground motion is the closest part of the rupture. The other parts, which are relatively far from the station, will act only to elongate the duration time, but not to increase the peak amplitude. Thus the ground motion decays very slowly in this region. An upper limitation of the ground motion appears which can be estimated with the rock strength, the stress drop of the local rupture (e.g. Brune, 1970; Newmark and Rosenblueth, 1971; Housner, 1975). This near-field ground motion saturation should be included into the attenuation relationship. Thus different models are developed to account for this phenomenon (e.g. Campbell and Duke, 1974; Boore and Joyner, 1984; Campbell, 1981; Bolt and Abrahamson, 1982; Espinosa, 1980). The existing and widely used attenuation relationships can be found in the following articles: Abrahamson and Silva (1997), Boore et al. (1997), Campbell (1997), Campbell and Bozorgnia (2003), Idriss (1991), Sadigh et al. (1997).

The following are the main technical issues being addressed in the next generation attenuation relationship development and in the supporting research (Chiou et al., 2004).

- Consideration of the following effects on ground motions:
 - Rupture directivity;
 - Polarization of near-field motion (fault-strike-normal component vs. fault-strike-parallel component);
 - Footwall vs. hanging wall for dipping faults;
 - Style of faulting (strike-slip, reverse, normal);
 - Depth to faulting (e.g., buried vs. surface rupture);
 - Static stress drop (or rupture area);
 - Site amplification effects relative to a reference “rock” condition;
 - 3-D sedimentary basin amplification (depth to basement rock);
- Consideration of the following features in the statistical analysis of data:
 - Uncertainties in predictor variables (e.g. uncertainty in the magnitude of an earthquake);
 - Missing values of predictor variables (e.g. the NEHRP category of a recording site);
 - Dependencies of standard errors on magnitude, distance, and soil type.

1.1.2 Stochastic Method

This simple and powerful method has been widely used in the prediction of strong ground motions (Hanks and McGuire, 1981; Boore, 1983, 1986, 1996; Boore and Atkinson, 1987; Atkinson and Boore, 1997; Atkinson and Beresnev, 1998). It combines parametric or functional descriptions of the ground motion’s amplitude spectrum with random phase spectrum modified in such a way that the motion is distributed over a duration related to the earthquake magnitude and to the distance from the source. It distills what is known about the various factors affecting ground motions (source, path, and site) into simple function forms and distinguishes the *S*-wave and the *P*-wave.

Based on these attenuation relationships the ground motion – from an earthquake of magnitude M_0 , at a site (R distant from the source) and at frequency of ω – may be expressed in the frequency domain as follows:

$$Y(M_0, R, \omega) = E(M_0, \omega)P(R, \omega)G(\omega)I(\omega) \quad (1.1)$$

where $Y(M_0, R, \omega)$, $E(R, \omega)$, $G(\omega)$, and $I(\omega)$ are respectively the spectra of ground motion, source, path, local site effect and instrument.

This method often goes by the name of “Stochastic Method” which is essential for earthquake engineers. Provided all terms in the right side of equation 1.1, this method is fast to simulate ground motions. It is particularly useful for simulating the higher-frequency ground motions of most interest to engineers (generally, $f > 0.1$ Hz). Since the key role $P(R, \omega)$ is derived from the real observations, this method is not applicable to the regions without enough data. More information about this method can be found in [Boore \(2003\)](#).

With the growing recognition that finite-fault effects, including rupture geometry and directivity, can profoundly influence the character of strong-ground motions, in both the near- and far-field regions ([Hartzell, 1978](#); [Irikura, 1983](#); [Joyner and Boore, 1986](#); [Somerville et al., 1991](#); [Hutchings, 1994](#); [Zeng et al., 1994](#)). [Silva \(1990\)](#), [Schneider et al. \(1993\)](#), [Beresnev and Atkinson \(1997\)](#) and [Beresnev et al. \(1998\)](#) extended the stochastic modelling technique to consider rupture effect due to a finite-fault plane.

1.1.3 Deterministic Method

This is the method which will be adopted for this thesis for calculating the ground motions during an earthquake. To solve the wave equation by a deterministic method, the geological model is approximated by a numerical mesh, that is, the model is discretized into a finite number of points. These techniques are also called grid methods and full-wave equation methods, the latter since the solution implicitly gives the full wave-field. Deterministic methods do not have restrictions on the material variability and can be very accurate when a sufficiently fine grid is used. Furthermore, the technique can handle the implementation of different rheologies and is well suited for the generation of **snapshots** which can be an important aid in the interpretation of the results. A disadvantage of these general methods, however, is that they are more expensive than the two before-mentioned methods in terms of computer time and memory occupation.

Normally the higher the interesting frequency, the bigger the memory and the more CPU time is needed. The modelling can be made more efficiently by using hybrid techniques, for instance, combining finite differences with faster algorithms – the stochastic method. In this way, modelling of the full wave-field can be restricted to the target region and the propagation in the rest of the model can be simulated with faster methods.

One of those popular and matured numerical methods – the **Finite Difference** method – is adopted in this pilot study to take the advantage of small CPU time occupation, easy implementation of the absorbing boundary condition and double-couple point source and kinematic source scenario.

1.2 Motivation and Plot

Since the earthquake destroys the buildings by acting a “load” caused by the vibrational motion of the ground which is caused by earthquake waves propagating away from the earthquake

source. And earthquake ground motion is a complicated phenomenon and the complication comes from several factors, critical but not accurately known, such as the dynamics of source rupture and the details of the transmitting media; these vary either from source to source, from path to path or from site to site and therefore introduce large scattering in values of ground motion. Thus the calculation of the complete wave-field for potential large earthquakes in a given seismically active region of known structure will play a central role in reliably estimating shaking hazard (e.g., [Olsen and Archuleta, 1996](#); [Olsen, 2000](#); [Ewald et al., 2006](#)). Such calculations will complement hazard estimation based on probabilistic estimates of seismicity (e.g., [Gerstenberger et al., 2005](#)) and/or stochastic means to calculate ground motion scenarios based on highly simplified physical models (e.g., [Beresnev et al., 1998](#); [Boore, 2003](#)). Earthquake-induced ground motions strongly depend on: (1) the velocity structure and (2) the finite-fault slip histories. The local and regional velocity structure can be estimated and continuously improved using tomographic tools and/or direct measurements (e.g., borehole information). However, the variation concerning rupture processes remains and it is unquestionable that hazard relevant ground motion characteristics for earthquakes of a given size will strongly depend on some rupture properties such as stress drop, source mechanisms, rupture velocity, slip speed, etc..

This poses a formidable problem when faced with the task of estimating ground motion due to one or more “characteristic earthquakes” of a specific seismically active region. In addition to the variations caused by the shallow velocity structure at frequencies relevant to structures, one would have to calculate many different slip scenarios for one presumed earthquake in order to account for rupture related variations. In order to quantify these variations we propose to generate data bases with Green’s functions calculated for discrete models of faults or fault systems for areas with sufficiently well known 3D velocity structure and fault location. The surface ground motions for each sub-fault excitation are stored which allow arbitrary finite fault scenarios to be synthesized at very little computational costs compared to a normal complete 3D calculation, once the database is available. The opportunity to investigate ground motion variations as a function of many different rupture related parameters for a specific area comes at the price of a sufficiently large number of initial 3D simulations for the pre-designed discretized fault and is economical if the number of synthesizations exceeds the number of NGF calculations.

In this thesis we introduce the concept of the NGF method, discuss the accuracy of the method as a function of sub-fault size and other earthquake related parameters, and present applications to a model of the Newport-Inglewood fault in the Los Angeles Basin. The approach enables us to investigate the interesting topic, namely how the ground motion varies with the source and the basin structure. Benefiting from the method for calculating quasi-dynamic rupture process published in [Guatteri et al. \(2004\)](#) we can fix the final slip distribution and vary the hypocentre location and calculate the corresponding ground motions and investigate the complex variation of ground motion (translation and rotation). At the same time, we can also focus on the source scenarios with fixed hypocentre but varying final slip distribution. After checking our results with another research, the ground motions variations in the near-source field are presented, discussed and cross-compared.

Chapter 2

Methodology

With the development of the computational technology, more and more wave propagation problems can be solved and simulated with numerical tools. From the physical point of view, these tools should be capable to properly insert the source, consider the energy spreading in the propagation process, absorb the outgoing energy at the boundary and reflect the energy at the free surface. Considering the complexity of the medium properties and the real topography, different numerical tools are developed. We will shortly describe those tools and focus on the technologies we adopt in this thesis. At the same time, different tools are also developed to generate complex source scenarios. One of them is presented in this chapter, too.

2.1 3D Staggered-Grid Finite-Difference Scheme

In order to calculate wave-field simulations for real **3D velocity structure** at frequencies of interest to both seismologists and engineers, we turn to those deterministic computational methods whose efficiency has advanced to such a state which can fulfill our requirements. The most general of these numerical methods are grid-based techniques that track the wave field on a dense 3D grid of points, e.g., the finite-difference (FD), finite-element (FE), and pseudo-spectral (PS) methods. Various algorithms have been developed to implement these techniques, and while there will always be debate as to which one is the “best” technique, each method has its merits and pitfalls.

The 3D staggered-grid finite-difference velocity-stress scheme, with 2-4 implementation (second-order accurate in time and fourth-order accurate in space) has become increasingly popular for simulating elastodynamic equation of ground motion. In seismic applications, the velocity-stress formulation was first used by [Madariaga \(1976\)](#) to model fault-rupture dynamics. [Virieux \(1984, 1986\)](#) and [Levander \(1988\)](#) have extended the technique to model seismic wave propagation in 2D media, and the formulation for 3D media is outlined by [Randall \(1989\)](#) and [Yomogida and Etgen \(1993\)](#). It was developed by [Virieux \(1984\)](#) to model the P-SV wave propagation in heterogeneous media. [Graves \(1996\)](#) incorporated the moment tensor source, implemented a stable and accurate representation of a planar free-surface boundary and also spatially variable anelastic attenuation. It was also widely used to simulate earthquake scenarios, such as the effect due to the local site condition ([Olsen, 2000](#)), kinematic rupture process and even dynamic rupture process. The advantages of the staggered-grid formulation are:

- Source insertion is straightforward and can be expressed in terms of velocity (via body

forces) or stress;

- Stable and accurate representation for a planar free-surface boundary is easily implemented;
- Since the finite-difference operators are local, the entire model does not have to reside in core memory all at once;
- It is easily extended to high-order spatial difference operators;
- The method can be interfaced with other modelling techniques by expressing the input wave field along a boundary of the finite-difference grid;
- The algorithm is easily implemented on scalar, vector, or parallel computers.

In the following chapter we outline the numerical approach beginning with the equations of motion and then describe their discrete formulation using the staggered-grid approach with a Perfectly Matched Layer (PML) boundary condition. We discuss in detail some ideas related to incorporating earthquake (double couple) sources and free-surface boundary implementation.

2.1.1 Temporal Extrapolation and Derivation

The following series of equations track the wave propagation within three-dimensional (3D), linear, isotropic elastic media.

Equations which conserve the momentum:

$$\rho \delta_{tt} u_x = \delta_x \tau_{xx} + \delta_y \tau_{xy} + \delta_z \tau_{xz} + f_x \quad (2.1)$$

$$\rho \delta_{tt} u_y = \delta_x \tau_{xy} + \delta_y \tau_{yy} + \delta_z \tau_{yz} + f_y \quad (2.2)$$

$$\rho \delta_{tt} u_z = \delta_x \tau_{xz} + \delta_y \tau_{yz} + \delta_z \tau_{zz} + f_z \quad (2.3)$$

and the stress-strain relations:

$$\tau_{xx} = (\lambda + 2\mu) \delta_x u_x + \lambda (\delta_y u_y + \delta_z u_z) \quad (2.4)$$

$$\tau_{yy} = (\lambda + 2\mu) \delta_y u_y + \lambda (\delta_x u_x + \delta_z u_z) \quad (2.5)$$

$$\tau_{zz} = (\lambda + 2\mu) \delta_z u_z + \lambda (\delta_x u_x + \delta_y u_y) \quad (2.6)$$

$$\tau_{xy} = \mu (\delta_y u_x + \delta_x u_y) \quad (2.7)$$

$$\tau_{xz} = \mu (\delta_z u_x + \delta_x u_z) \quad (2.8)$$

$$\tau_{yz} = \mu (\delta_z u_y + \delta_y u_z) \quad (2.9)$$

Herein the (u_x, u_y, u_z) stand for the displacement components; $(\tau_{xx}, \tau_{yy}, \tau_{zz}, \tau_{xy}, \tau_{xz}, \tau_{yz})$ stand for the stress components; (f_x, f_y, f_z) stand for the body-force components.

By first differentiating the stress-strain sets of equations with respect to time and substituting the time-differentiated displacements $\delta_t(u_x, u_y, u_z)$ with the velocity components (v_x, v_y, v_z) , we can solve the wave propagation in terms of velocity and stress rate. The resulting sets of equations are:

$$\delta_t v_x = \frac{1}{\rho} (\delta_x \tau_{xx} + \delta_y \tau_{xy} + \delta_z \tau_{xz} + f_x) \quad (2.10)$$

$$\delta_t v_y = \frac{1}{\rho} (\delta_x \tau_{xy} + \delta_y \tau_{yy} + \delta_z \tau_{yz} + f_y) \quad (2.11)$$

$$\delta_t v_z = \frac{1}{\rho} (\delta_x \tau_{xz} + \delta_y \tau_{yz} + \delta_z \tau_{zz} + f_z) \quad (2.12)$$

and

$$\delta_t \tau_{xx} = (\lambda + 2\mu) \delta_x v_x + \lambda (\delta_y v_y + \delta_z v_z) \quad (2.13)$$

$$\delta_t \tau_{yy} = (\lambda + 2\mu) \delta_y v_y + \lambda (\delta_x v_x + \delta_z v_z) \quad (2.14)$$

$$\delta_t \tau_{zz} = (\lambda + 2\mu) \delta_z v_z + \lambda (\delta_x v_x + \delta_y v_y) \quad (2.15)$$

$$\delta_t \tau_{xy} = \mu (\delta_y v_x + \delta_x v_y) \quad (2.16)$$

$$\delta_t \tau_{xz} = \mu (\delta_z v_x + \delta_x v_z) \quad (2.17)$$

$$\delta_t \tau_{yz} = \mu (\delta_z v_y + \delta_y v_z) \quad (2.18)$$

The computation procedure to calculate the wave propagation within the media is achieved by the following two steps (in 1D case, for example):

1. Calculation of time derivatives

From the approximation of the Taylor expression for a function $f(x)$

$$f(x + \Delta x) = f(x) + f'(x) \Delta x + \frac{\Delta x^2}{2!} f''(x) + \frac{\Delta x^3}{3!} f'''(x) + \dots \quad (2.19)$$

we can deduce the differential quotients with respect to space in forward or backward direction as

$$\frac{\delta f}{\delta x} \approx \frac{f(x) - f(x - \Delta x)}{\Delta x} \quad (2.20)$$

$$\frac{\delta f}{\delta x} \approx \frac{f(x + \Delta x) - f(x)}{\Delta x} \quad (2.21)$$

2. Extrapolation in time

Also based on the Taylor expansion of a function, the value of a function at the next time step could be approximately written as:

$$f(t + \Delta t) \approx f(t) + \frac{\delta f(t)}{\delta t} \Delta t. \quad (2.22)$$

This method is called an explicit method. Since the time step is determined by accuracy criteria rather than by stability criteria, the general way to solve the differential formulation of the wave equation is with this explicit method (Emerman et al., 1982).

Using staggered-grids, we can simulate the heterogeneous medium with a stable scheme for large variation of Poisson's ratio (Virieux, 1986). In staggered-grid methods, groups of field variables and material properties are defined on different meshes separated by half the grid spacing. The newly computed variables are centered between the old variables. Staggering effectively halves the grid spacing, increasing the accuracy of the approximation and improving accuracy and stability, and eliminate no-causal artifacts (Virieux, 1986; Levander, 1988; Carcione and Helle, 1999). The velocity-stress formulation in staggered grids constitutes a flexible modelling technique because it allows one to freely impose boundary conditions and is able to directly yield all the field variables (Karrenbach, 1999). For detailed solution of this staggered-grid finite-difference technique and the numerical accuracy and stability analysis the reader is referred to these articles: Virieux (1986); Levander (1988); Randall (1989).

2.1.2 Double Couple Point Source Implementation

As has been depicted before, staggered-grid method has an advantage – straightforward source insertion expressed in terms of velocity or stress. Assume we have the focal mechanism of a hypothetical small earthquake represented with a point source (pure shear). The individual 6 moment tensor components are related to the focal mechanism parameters as follows:

$$m_{xx} = -\sin\delta \cos\lambda \sin 2\theta_s + \sin 2\delta \sin\lambda \sin^2\theta_s, \quad (2.23)$$

$$m_{yy} = \sin\delta \cos\lambda \sin 2\theta_s - \sin 2\delta \sin\lambda \cos^2\theta_s, \quad (2.24)$$

$$m_{zz} = \sin 2\delta \sin\lambda, \quad (2.25)$$

$$m_{xy} = \sin\delta \cos\lambda \cos 2\theta_s + \frac{1}{2} \sin 2\delta \sin\lambda \sin\theta_s, \quad (2.26)$$

$$m_{xz} = -\cos\delta \cos\lambda \cos\theta_s + \cos 2\delta \sin\lambda \sin\theta_s, \quad (2.27)$$

$$m_{zy} = -\cos\delta \cos\lambda \sin\theta_s - \cos 2\delta \sin\lambda \cos\theta_s, \quad (2.28)$$

where m_{ij} is the ij th component of the Moment tensor. Parameters δ , λ and θ_s are the dip, rake and strike angles of the point source (Aki and Richards, 2002).

In order to simulate the temporal behavior of the equivalent body forces which are created by the earthquake, some functions are introduced by different scientists which are named as the source time function. Normally they are based on the displacement of the relative motion between two sides of the fault plane. With a time differentiating, the exact form we use could be acquired. What should be kept is that this time source function should be normalized with respect to the integration over the total duration time to 1.

Thus, with the scalar earthquake moment M_0 , the shear constant, μ , the moment tensor m_{ij} and the source slip rate function $s_r(t)$, it is straightforward to exert the force at the location of the point source. Here is the final equation of the temporal moment tensor M_{ij} :

$$M_{ij} = M_0 \cdot \mu \cdot m_{ij} \cdot s_r(t) \quad (2.29)$$

2.1.3 Free Surface Boundary

Because of concerns related to numerical stability and accuracy of the computed response, finite-difference schemes require careful consideration of the free-surface boundary condition. For our case of planar surface, an explicit boundary condition is adopted for the reason that it requires less points per wavelengths and superior in accuracy compared to the vacuum formulation (e.g., Graves, 1996).

Generally speaking, two implementations of the explicit free-surface boundary condition are developed and 1/2 grid-length apart vertically. Since it is hard to tell which one is better in terms of the epicenter distance (Gottschämmer and Olsen, 2001), we use the comparatively simpler one which is written in the article of Graves (1996). The free-surface is co-located with the normal stress position. This method satisfies the stress-condition at the free-surface which means the following:

$$\tau_{zz} = \tau_{xz} = \tau_{yz} = 0|_{free-surface}. \quad (2.30)$$

τ_{zz}, τ_{xz} and τ_{yz} between the free-surface are explicitly settled to be antisymmetric with the

free-surface itself:

$$\tau_{zz}^{k-1} = -\tau_{zz}^{k+1}, \quad (2.31)$$

$$\tau_{xz}^{k-1/2} = -\tau_{xz}^{k+1/2}, \quad \tau_{xz}^{k-3/2} = -\tau_{xz}^{k+3/2}, \quad (2.32)$$

$$\tau_{yz}^{k-1/2} = -\tau_{yz}^{k+1/2}, \quad \tau_{yz}^{k-3/2} = -\tau_{yz}^{k+3/2}, \quad (2.33)$$

where k is the location of the surface in grid. For the computation of the normal stress (τ_{xx}, τ_{yy}) at the surface, special attention should be paid because they are derived also from the velocity values at 3/2 grid point above the free surface. We use the second-order accuracy in the computation of the vertical spatial derivatives of the horizontal normal stress at the free surface.

2.1.4 Perfectly Matched Layer Boundary

The simulation of waves by deterministic methods in unbounded domains requires a special treatment for the boundaries of the necessarily truncated computational domain. Now the mostly used and advantageous method is the recently developed one, the Perfectly Matched Layer (PML) scheme. The principal idea of this method is to introduce an absorbing layer in which each component (velocity or displacement) is composed into two auxiliary components: a component orthogonal to the boundary and a component parallel to it. A system of equations governing these new unknowns is constructed. A damping term is finally introduced for the component orthogonal to the boundary. Thus this layer model has the property of generating no reflection at the interface between the free medium and the artificial absorbing medium both during and after the arrival of the primary seismic phases. In particular, PML tends to absorb relatively uniformly across the simulation bandwidth, including the long periods where the [Cerjan et al. \(1985\)](#) boundary seems to be less efficient.

As for the absorbing boundary for the special case of 3D staggered-grid finite difference scheme with free surface and heterogeneity of the medium and with a 2-4 implementation (second-order accurate in time and fourth-order accurate in space), we use the one developed by [Marcinkovich and Olsen \(2003\)](#).

The two sets of equations for simulating the wave propagation are split into component parallel and orthogonal to the interface, based on the spatial derivative separation. The orthogonal one consists of the spatial derivative which acts normal to the three coordinate planes, X, Y, Z . This term is damped with the pattern illustrated in the following part, or different layer inside the absorbing boundary are multiplied by its respective pre-settled value. The parallel one contains the other spatial derivative terms. The summation of the damped orthogonal part and the untouched parallel part is used to calculate the respective values for the next time step. In the horizontal edges, vertical edges and corners of the total working bulk needs multiple damping terms.

Here we show the exact way to calculate the damping term inside the PML, which is easily used in a arbitrary PML thickness. First the maximum damping value for a PML with width between 1 and 20 is:

$$d_0 = \frac{\tau V_s}{\Delta h} (c_1 + c_2 n_b + c_3 n_b^2) \quad (2.34)$$

where n_b is the thickness of the PML (in nodes), τ is the tuning parameter which in practice ranges from 3 to 4. V_s is the prominent velocity in earthquake simulation, Δh is the grid-length, and the polynomial coefficients are the following: $c_1 = \frac{8}{15}$, $c_2 = \frac{-3}{100}$ and $c_3 = \frac{1}{1500}$.

From the maximum damping value there are several ways to select the exact individual damping value for each layer of PML (e.g., [Hastings et al., 1996](#); [Chew and Liu, 1996](#); [Liu and Tao, 1997](#); [Zeng and Liu, 2001](#); [Collino and Tsogka, 2001](#)). But the typical one is:

$$d_i = d_0 \left(\frac{i}{n_b} \right)^P \quad (2.35)$$

where d_i is the damping value of the i th node as counted from the PML interface with the free medium. With P values in the range of 1 to 4 this equation provides meaningful results. In this study it is fixed to 2.

2.2 Rupture Process

Images of the spatial and temporal evolution of earthquake slip on fault planes provide compelling evidence that fault displacement is spatially variable at all resolvable scales. These finite-source rupture models are typically derived by inversion of low-pass-filtered strong ground motion recordings (e.g., [Beroza and Spudich, 1988](#)), sometimes augmented with teleseismic data ([Hartzell and Heaton, 1983](#); [Wald et al., 1991](#)) and/or geodetic measurements ([Heaton, 1982](#); [Wald and Somerville, 1995](#); [Yoshida et al., 1996](#)). Inversions of geodetic data only are also used to constrain larger-scale slip ([Larsen et al., 1992](#); [Bennett et al., 1995](#)), and provide independent evidence for spatial variability of slip. Some studies of strong motion data indicate that the rupture velocity is spatially variable as well ([Archuleta, 1984](#); [Beroza and Spudich, 1988](#); [Bouchon et al., 2000](#)), adding another degree of complexity into the rupture process. This rupture variability is of great interest because it strongly influences the level and variability of damaging high-frequency seismic energy radiated by an earthquake ([Madariaga, 1976, 1983](#); [Spudich and Frazer, 1984](#)).

Numerous theoretical studies of extended-source earthquake models describe the complex rupture process. First, **dynamic** descriptions of the earthquake source are based on models that satisfy elasto-dynamic equations with a prescribed fracture criterion on a pre-determined fault plane ([Andrews, 1976](#); [Day, 1982](#); [Das and Kostrov, 1987](#); [Quin and Das, 1989](#)). An earthquake is modelled as a dynamically propagating shear crack that radiates seismic waves. The slipping fault is associated with a drop in shear stress, and the evolution of rupture depends on the initial conditions and the failure criterion. Second, **kinematic** descriptions of the earthquake source, on the other hand, specify the slip as a function of space and time without explicit consideration of a physical model for the rupture process, which therefore may not be physically realizable.

In this project, we take the advantage of the new developed “pseudo dynamic” method ([Guatteri et al., 2004](#)) which, actually is a kinematic model, but capable to emulate important characteristics of dynamic rupture and to identify important interactions between source properties (rupture velocity, slip velocity, rise time, etc.) that are relevant for strong ground motion prediction. In this way the stochastic characterization of the spatial complexity of earthquake slip as found in finite-source slip inversions is also considered. This method is summarized in the following (with all illustrations in [Fig. 2.1](#)):

1. Define the target earthquake’s magnitude and event type;
2. Assign or determine the fault dimensions ([Wells and Coppersmith, 1994](#); [Somerville et al., 1997](#); [Mai and Beroza, 2000](#));

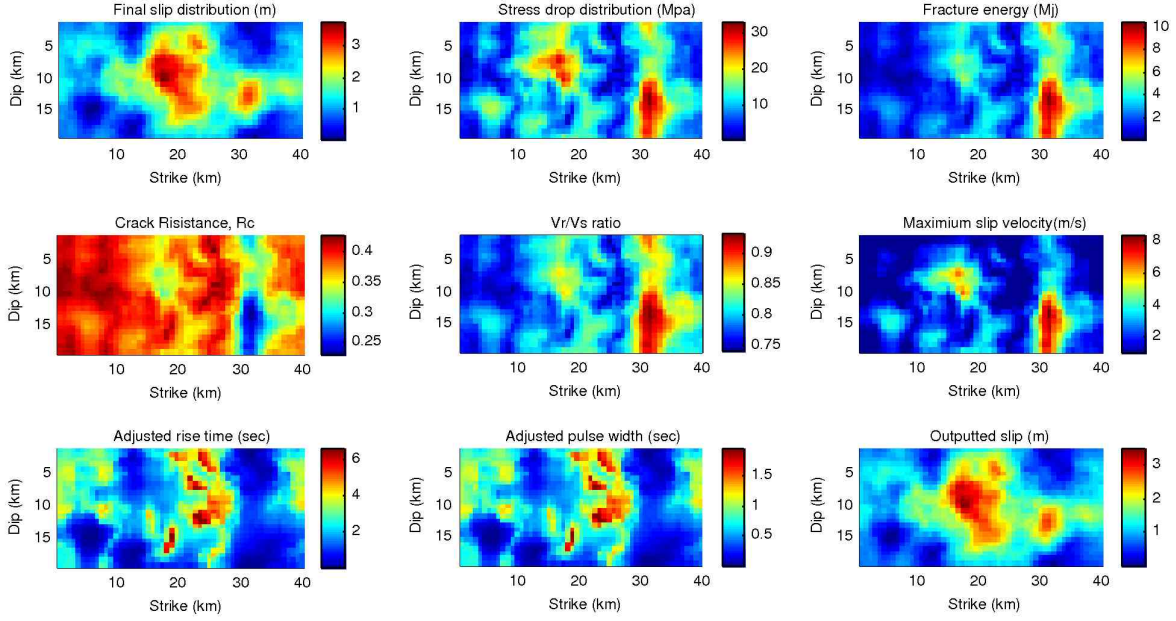


Figure 2.1: Procedure for generating the different source parameters for a quasi-dynamic rupture process. (After [Guatteri et al., 2004](#)). The procedure starts at a slip realization generated as a 2D random field (see [Mai and Beroza, 2002](#)).

3. Set the hypocentre location;
4. Generate a stochastic slip distribution, $D(x, z)$, following one of the equations presented in [Andrews \(1980\)](#); [Somerville et al. \(1997\)](#); [Mai and Beroza \(2002\)](#) with a pre-chosen auto-correlation length which is found to be empirically related to the magnitude ([Mai and Beroza, 2000](#));
5. Compute the corresponding static stress-drop distribution, $\Delta\tau(x, z)$, with the relation presented in [Andrews \(1980\)](#):

$$\Delta\tau(k) = -K(k) \cdot D(k) \quad (2.36)$$

where $\Delta\tau(k)$ and $D(k)$ denote the 2D stress drop $\Delta\tau(x, z)$ and slip function $D(x, z)$, in the wavenumber domain, respectively. $K(k)$ represents the static stiffness function which, for crustal rocks, can be approximated as $K(k) = -\frac{1}{2}\mu k$ and $k = \sqrt{k_x^2 + k_y^2}$ being the wavenumber;

6. Generate a distribution of fracture energy (G_c) from slip distribution. The **empirical** linear relationship is developed by ([Guatteri et al., 2004](#), equation 6), where the conditional expectation of G_c is :

$$E(G_c|\beta, \Delta\tau, L_h) = \beta_0 + \beta_1 \Delta\tau L_h^{1/2} \quad (2.37)$$

where $\beta_0 = 0.18$ and $\beta_1 = 0.0015$ for $M \leq 6.5$ and $\beta_0 = 2.7$ and $\beta_1 = 0.0021$ for $M \geq 6.5$. $\Delta\tau$ stands for the stress drop and L_c is the characteristic crack length;

7. Calculate rupture velocity and rupture arrival time distributions. Rupture velocity is related to the resistance parameter R_c by

$$1 - v^2/\beta^2 = \pi^2 \cdot (R_c/2)^2 \quad (2.38)$$

where R_c is a dimensionless parameter given by:

$$R_c = \mu \cdot G_c / (\Delta\tau^2 \cdot L_h) \quad (2.39)$$

Combine these two forward equations, equation (2.37) and equation (2.39), we get the relationship between the crack resistance parameter R_c and the stress drop $\Delta\tau$, crack length L_h and the elastic modulus μ as follows:

$$R_c = \mu \cdot \frac{\beta_0 + \beta_1 \Delta\tau L_h^{1/2}}{\Delta\tau^2 L_h} \quad (2.40)$$

8. The slip rate function is approximated by two overlapping triangles, T1 and T2, with a total base equal to the rise time T_r . T1 is an isosceles triangle and is the portion that contributes the most to the high frequency seismic radiation. See Fig. 2.2.

V_{max} is calculated as:

$$V_{max} = 0.5 \cdot V_{maxref} \cdot W \cdot \tau_p \cdot v / (\beta \cdot \mu) \quad (2.41)$$

where W is the width of the fault, $\tau_p = \max(\Delta\tau, w(\tau_x - \tau_d))$ and $V_{maxref} = 0.9 D_c f_c$, where D_c is a chosen value of slip-weakening distance, $\tau_s - \tau_d = 2G_c/D_c$, and f_c is a frequency parameter defined in Ohnaka and Yamashita (1989). For $\Delta\tau > 0$, $w = 0.6$.

9. Apply two-step procedure to derive the distribution of T_p and T_r .

Then the pulse width T_p is calculated by:

$$T_p = \beta_1 \cdot \Delta u / V_{max} \quad (2.42)$$

where $\beta_1 = 0.84$, Δu is the total slip.

And the rise time T_r is given by:

$$T_r = T_p + \frac{\Delta u}{cV_{max}} \quad (2.43)$$

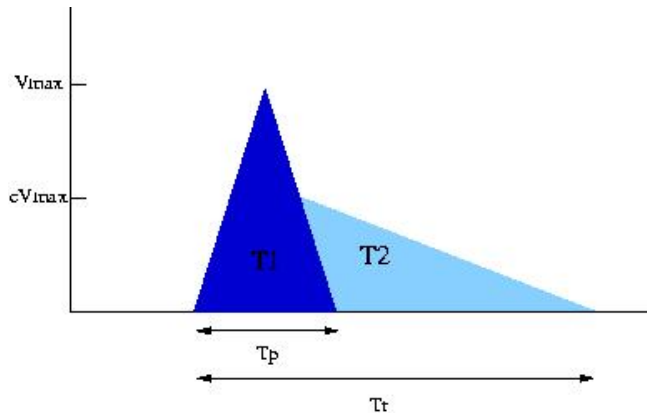


Figure 2.2: Slip rate function adopted in the quasi-dynamic process, characterized as isosceles triangle T1 and a rectangular triangle T2 which are overlapped with each other. c is chosen to be $1/2$.

2.3 Conclusions

In this chapter we describe the basic numerical tools adopted in this thesis for the realization of the wave propagation in 3D media which are used for the NGF generation (afterwards used to synthesize the ground motion). With these tools available, the NGF data base can be built up for the future use. At the same time, for the aim of arbitrary amount of source scenario creation, we refer to the quasi-dynamic rupture process generating tool in this chapter which will provide as many source scenarios as needed. However, for the first step – a trial, we will restrict us to the isotropic, elastic part of wave propagation and no topography will be considered. The fault plane is also assumed to be a straight plane.

Chapter 3

Numerical Green's Function Method

Deterministic earthquake scenario simulation methods are playing an increasingly important role in seismic hazard and risk estimation. However, the numerical calculation of the complete wave-field in the observed frequency band for a seismically active basin remains a computationally expensive task. For example, with a working area of $160 \times 130 \times 60$ km and with the lowest shear-wave velocity of 1200 m/s, in order to simulate the strong ground velocity with frequency larger than 2 Hz, we have to set the grid-length less than 100 m to avoid the effect of numerical dispersion.

Our aim is to provide a tool with which we can calculate a large number of different finite source scenarios for a particular fault or fault system in one seismic active area. In order to avoid having to run the 3D code for each kinematic source scenario, we propose the concept of “Numerical Greens functions” (NGFs). The basic idea is that: a large seismic fault or fault system is uniformly divided into sub-faults of appropriate sizes. For those sub-faults synthetic seismograms for the whole surface of the seismically active area are calculated and stored with the correct velocity model taken into account. Within some limitations, arbitrary kinematic sources can be simulated, inexpensively, by superposition of this set of separate seismograms. In the following we present the basic theory of this method.

3.1 Representation Theorem

The elastodynamic Green's function is introduced to describe the displacement field from a unidirectional unit impulse in the j -direction which is localized precisely in space ξ and time τ . The i th component of that displacement at receiver \mathbf{x} and time t is denoted as $G_{ij}(\mathbf{x}, t - \tau, \xi)$ (Aki and Richards, 2002). The Green's function provides all the information about how the wave propagates in the 3D medium from the small dislocation (impulse in time) to a receiver on the surface. Using that concept, the ground displacement during a large earthquake can be stated with the representation theorem as following (Aki and Richards, 2002, equation 3.18):

$$\begin{aligned} u_i(\mathbf{x}, t) &= \int_{-\infty}^{\infty} d\tau \iint_{\Sigma} [s_j(\xi, \tau)] v_k(\xi) c_{j k p q}(\xi) \frac{\partial}{\partial \xi_q} G_{ip}(\mathbf{x}, t - \tau(\xi), \xi) d\Sigma \\ &= \iint_{\Sigma} [s_j(\xi, t - \tau(\xi))] v_k(\xi) c_{j k p q}(\xi) * \frac{\partial}{\partial \xi_q} G_{ip}(\mathbf{x}, t, \xi) d\Sigma, \end{aligned} \tag{3.1}$$

where $u_i(\mathbf{x}, t)$ is the i th component of the ground displacement at general (\mathbf{x}, t) , excited by the displacement discontinuity, $[\mathbf{s}(\xi, t - \tau(\xi))]$, across the internal surface Σ whose normal direction is indicated by a unit vector $v(\xi)$. $c_{j k p q}(\xi)$ is the elastic parameter tensor. $\tau(\xi)$ stands for the delay time of the rupture front propagation.

The moment tensor density is introduced in (Aki and Richards, 2002, equation 3.19) as:

$$\tilde{m}_{pq}(\xi, t) = [s_j(\xi, t - \tau(\xi))]v_k(\xi)c_{j k p q}(\xi). \quad (3.2)$$

For a shear fault located inside an isotropic medium, $\tilde{m}_{pq}(\xi, t)$ can be simplified to:

$$\tilde{m}_{pq}(\xi, t) = \mu(\xi)s(\xi, t - \tau(\xi))\tilde{M}_{pq}(\xi), \quad (3.3)$$

where $\mu(\xi)$ is the shear modulus and scalar function $s(\xi, t - \tau(\xi))$ is the slip function. $\tilde{M}_{pq}(\xi)$ depends on the internal surface geometry and the slip direction.

The internal surface Σ can be sub-dividing into a number of elements σ_n ($n = 1, \dots, N$), and equation 3.1 can be reformulated as:

$$u_i(\mathbf{x}, t) = \sum_{n=1}^N \iint_{\sigma_n} \mu(\xi)s(\xi, t - \tau(\xi))\tilde{M}_{pq}(\xi) * \frac{\partial}{\partial \xi_q} G_{ip}(\mathbf{x}, t, \xi) d\sigma, \quad (3.4)$$

where the part after the summation in equation 3.4 represents the ground displacement excited by this small internal surface, σ_n , or a small earthquake.

3.2 Empirical Green's Functions

Assume the small earthquake, σ_n , in equation 3.4 begins to break after a certain time, τ_n , accounting for the time delay of the rupture front propagation. Name that part as $u_i^n(\mathbf{x}, t)$ ($n = 1, \dots, N$) we get:

$$u_i(\mathbf{x}, t) = \sum_{n=1}^N u_i^n(\mathbf{x}, t - \tau_n). \quad (3.5)$$

In equation 3.5, the general idea behind the empirical Green's function (EGFs) method is expressed: to obtain the seismic motion excited by a large event, $u_i(\mathbf{x}, t)$ in equation 3.1, by linear summing the seismic motions excited by small events, $u_i^n(\mathbf{x}, t)$ (which are called empirical Green's functions (EGFs)). The following conditions between the small events and the larger event have to be fulfilled to approximate the correct u_i :

1. Focal mechanism similarity (the direction of the slip vector, $\mathbf{s}(\xi)$, and the normal direction of the internal surface, $v(\xi)$). The focal mechanisms of the EGFs should be similar to that of the large event (Hartzell, 1978).
2. Rupture process similarity. The rupture process of each small earthquake must be exactly the same as what happens in the same part of the fault plane of the large target earthquake.

3. Travel paths similarity ($\frac{\partial}{\partial \xi_q} G_{ip}(\mathbf{x}, t, \xi)$). The travel paths between the station and the small-event foci must be similar to the path between the station and the correspondent part of the large-event fault. For one specific seismic active area with 3D velocity structure, this assumption restricts the selection of the EGF to those located on that specific fault system.
4. Linearity. This assumption should be paid more attention in the area where nonlinear seismic motion can be produced. For example, inside the sedimentary basin, soil saturated with water can introduce liquefaction effect on the passing seismic motion. That liquefaction effect is different between the small earthquake and the large earthquake.

One possible way of acquiring these Green's functions is through recording the ground motions during a real earthquake. These Green's functions are named as Empirical Green's function. Several approaches were developed based on these principles (Frankel, 1995; Hutchings and Wu, 1990; Irikura, 1983; Wenerberg, 1990) which are different primarily in whether they use scaling relations when they summed up the single EGFs or implemented the source process for the larger aim earthquake. Roughly, based on this idea, EGF approaches can be distinguished into two main classes: the composite and the rupture parameter approach (Wössner et al., 2002; Gallovič and Brokešová, 2007a).

3.2.1 Composite Method

This method uses the same form of the equation 3.5. However it is not based on the representation theorem. It (Irikura, 1983; Wenerberg, 1990; Frankel, 1995) assumes that the large events are composites of small to moderate-sized events ($M \geq 3.5$ or $M_0 \geq 2.3 \times 10^{15} N \cdot m$). To be more exact, they assume one bigger fault plane could be described by a simple geometrical summation of its different pieces. The summation of the small events (EGFs) is thus based on scaling relations between small and large events (the stress drop is assumed to be constant throughout the fault plane). The number of subevents or EGFs is usually small, the discretization of the rupture process is quite coarse, which produces spatial and temporal high-frequency aliasing effects (Bour and Cara, 1997). This method has the advantage of simplicity, but its potential is limited by the fact that suitable empirical records are not always available.

3.2.2 Rupture parameter

The rupture parameter (Hutchings, 1991) uses very small events ($M_0 < 1.5 \times 10^{14} N \cdot m$, Hutchings and Wu (1990)). The small earthquakes are considered to be excited by a effective step-impulsive source time function. By de-convolving the specifically assumed source time function from the real recordings and normalizing the time-series of the small earthquake with its moment, recordings of these small events can be used directly in the representation relation (Aki and Richards, 2002) as (Empirical) Green's functions. The actual seismograms from a hypothetical rupture process are simulated by adding up EGFs using an appropriate kinematic rupture process. Therefore, the fault plane of the targeted event is discretized into elemental areas that are small enough to model continuous rupture up to the highest frequency of interest. The summation of the separate moments of all elements should match the given targeted moment to keep the radiated energy the same. Since empirical Green's functions

scale linearly only in amplitude with differences in seismic moment, they can provide the contribution from any appropriate discretized elementary source area.

3.3 Numerical Green's Function

Another way to acquire the Green's functions is the numerical tool in which a point source (a grid of the method) is used to represent a small source and thus some approximations have to be made. In this section, following the essential idea behind the two forward mentioned methods, we develop the approach adopted for ground motion simulation in this thesis. We will work with the *velocity*, instead of the *displacement wave field*. So the $G_{ip}(\mathbf{x}, t, \xi)$ in equation 3.1 will stand for the i th component of the ground velocity response of a slip rate impulse precisely located at ξ and time τ (unit amplitude and in p -direction). Following the same idea of deducing from equation 3.1 to equation 3.5, we get the i th component of ground velocity at \mathbf{x} and time t , $v_i(\mathbf{x}, t)$, during a large earthquake as:

$$v_i(\mathbf{x}, t) = \sum_{n=1}^N \iint_{\sigma_n} \mu(\xi) s_r(\xi, t - \tau(\xi)) \tilde{M}_{pq}(\xi) * \frac{\partial}{\partial \xi_q} G_{ip}(\mathbf{x}, t, \xi) d\sigma, \quad (3.6)$$

where σ_n ($n = 1, \dots, N$) are the sub-faults of the large fault. $\mu(\xi)$ is the shear modulus. $s_r(\xi, t - \tau(\xi))$ is the scalar slip rate function. $\tilde{M}_{pq}(\xi)$ is the unit moment tensor density of the according source mechanism (fault plane geometry and slip direction).

Assume each point inside σ_n ruptures in the same direction and starts at the same time, σ_n is a plane inside which the elastic parameters are the same, we get the following equation after moving the constant part outside the integration:

$$v_i(\mathbf{x}, t) = \sum_{n=1}^N \mu^n s_r^n(t - \tau_n^0) \tilde{M}_{pq}^n * \iint_{\sigma_n} \frac{\partial}{\partial \xi_q} G_{ip}(\mathbf{x}, t, \xi) d\sigma, \quad (3.7)$$

where $s_r^n(t - \tau_n^0)$ is the slip rate function of the small source σ_n . Parameter μ^n is the shear modulus and \tilde{M}_{pq}^n represents the unit moment tensor density.

Let us neglect the difference between the different Green's tensor inside each σ_n . Then it can be taken out of the integral in equation 3.7,

$$\begin{aligned} v_i(\mathbf{x}, t) &= \sum_{n=1}^N \mu^n s_r^n(t - \tau_n^0) \tilde{M}_{pq}^n * \frac{\partial G_{ip}^n(\mathbf{x}, t)}{\partial \xi_q} A^n \\ &= \sum_{n=1}^N \left(\tilde{M}_{pq}^n \frac{\partial G_{ip}^n(\mathbf{x}, t)}{\partial \xi_q} \right) * s_r^n(t - \tau_n^0) \mu^n A^n, \end{aligned} \quad (3.8)$$

where A^n is the area of the sub-fault σ_n .

We call the part inside the brackets as the Numerical Green's Function (NGFs) which is the velocity response of the medium at location \mathbf{x} and time t due to a unit pure shear impulse slip rate. Name that as $g_i^n(\mathbf{x}, t)$, finally we get the basic equation to synthesize the individual NGFs to calculate the ground velocity as:

$$v_i(\mathbf{x}, t) = \sum_{n=1}^N g_i^n(\mathbf{x}, t) * s_r^n(t - \tau_n^0) \mu^n A^n. \quad (3.9)$$

This method is summarized and compared with graphical description in Fig. 3.1. A targeted fault plane (represented with solid red rectangle, Fig. 3.1 bottom left) is divided into uniform, rectangular sub-faults (colorful rectangles in Fig. 3.1 bottom right) and for each of these sub-faults the corresponding Numerical Green's function (Fig. 3.1 top right corner, double-couple source mechanism) is calculated (here we restrict ourselves to pure strike-slip excitation). The corresponding ground velocity of the large earthquake (Fig. 3.1 top left corner) can be synthesized with those individual NGFs. Even though in a strict mathematical sense the term *Green's function* is not correct we use it in connection with our source time function (a Delta function in slip rate). The calculations can be carried out using any numerical solution to the 3D wave propagation problem. Here we employ a high-order staggered-grid finite-difference approach (e.g., Igel et al., 1995; Gottschämmer and Olsen, 2001) with efficient absorbing boundaries based on the concept of perfectly matched layers (e.g., Collino and Tsogka, 2001; Marcinkovich and Olsen, 2003).

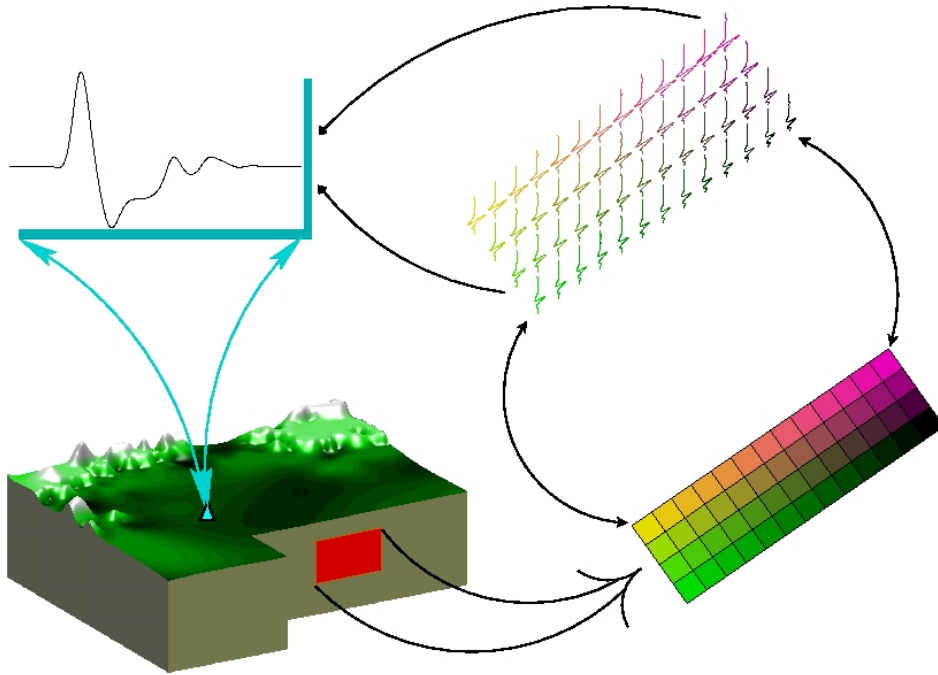


Figure 3.1: Schematic illustration of the Numerical Green's Function method. The fault plane (red solid rectangle) for a large earthquake is buried in the earth and zoomed into a larger one (bottom right). This fault plane is discretized into elements (colorful equilateral rectangles in the bottom right corner), whose corresponding Green's functions (at a specific station (cyan triangle)) are calculated (top right). The seismic motion of the large earthquake (top left) at the station (cyan triangle) can be synthesized with those individual Green's functions.

3.4 Discussion

The theoretical basis of the Green's function method is presented in the works of Aki and Richards (2002) and defined as including all the information of how the wave propagates after it leaves the source in heterogeneous medium. Thus how to use this concept into a practical

case is divided into two parts: acquisition of these Green's functions and implementing of an appropriate source. Before the numerical method and the computer technology were developed to an extent powerful enough to provide the 3D Green's function universally, the adoption of real recordings was the only way to go. Because of the scarcity of this data, especially in some seismic active area but without enough stations installed or lack of historical earthquakes, this method is not optimal.

Using the rupture parameter approach developed by [Hutchings and Wu \(1990\)](#), one can easily simulate the rupture process by varying the hypocentre location, rupture velocity, fault plane geometry, distribution of slip and rise time. But for an element that is not matched by any small earthquake the record from the adjacent elements have to be extrapolated with an assumed correction for differences in radiation pattern, attenuation and P and S travel times. At the same time, a relatively simple spectral division is used to obtain the source pulses from real recordings and thus will introduce errors in the frequency range where the amplitude value is small. The forward two shortages can be overcome when more and more data is available.

Another way to solve the data insufficiency problem could be to use numerical tools. That is the reason for the new method – the numerical Green's function. For a well enough investigated region, e.g. the Los Angeles basin, the Green's function, necessary for a specific fault system, could be calculated with numerical tools within a certain frequency range.

Normally, after the fault is activated at the hypocentre and begins to rupture, this rupture arrives at the different point inside one sub-fault at different time. Each point will slip with different slip time function and in different direction, too. Meanwhile, the Green's function between one station and each point inside this sub-fault is different from each other, e.g., in terms of the relative spatial location. However, discretizing equation (3.6) to equation (3.8) means all the area occupied by the small-event surface, A_n (equation 3.9), are forced, artificially, to start at the same time, follow the same sliprate time function to slip in the same direction. The difference in the rupture front arrival time to different part of A_n is artificially neglected. The travel path difference between different point of the sub-fault and the station is neglected, too. The difference in terms of sliprate between different points is neglected. These neglects will lead to errors of the seismic motion, compared with the continuous solution. The first step will be the pattern of discretizing the fault and understanding the resulting misfit introduced. We will focus on this topic in the following chapters.

[Graves and Wald \(2001\)](#) also calculated a database of Reciprocal Green's Functions by putting the source (double couple point source) at a station and recording the response at the whole 3D grids. Those responses can, reciprocally, be used as Green's Functions to resolve the trade-offs between the source complexity and the 3D elastic media's path effect when doing the finite fault source inversion. Their work focuses on a few stations on the surface where observations about an earthquake are available, while the fault discretization can be very small and reach the same scale of the grid-length adopted by the numerical method. Therefore, such a method is suitable when dealing with small number of receivers (with respect to number of subfaults). In the other way around, we discretize the fault plane into elements with certain size and calculate the responses for all the stations on the surface. The discretization of the fault plane with elements of certain size is a crucial point about the total amount of the calculation work. And afterwards, the spatial variation of the ground motions can be presented over the entire study area. The number of actual receivers is much larger than the number of subsources.

Chapter 4

Synthetic Tests – Benchmarking

Consider that the goal of the NGF method is to be able to synthesize – within some limits (e.g., reliable frequency range) – complete ground motions from arbitrary finite source scenarios on a discretized fault, and that the generation of an NGF data base is computationally expensive. For a specific magnitude, when the fault geometry is determined, the overall amount of calculation is inversely proportional to the sub-fault size. One key step of this thesis is to find a minimum number of sub-faults necessary to determine the ground motion with sufficient accuracy. We first qualitatively investigate the sub-fault size effect on the simulated ground motion in a homogeneous media. The optimal (largest) size of such sub-faults, for a specific magnitude of earthquake, is expected to depend on (1) the desired frequency band for the synthesized ground motions (i.e., the shortest wavelengths to be described in the 3D velocity model), (2) the properties of the ruptures themselves (rupture speed, slip velocity, rise time etc..) and (3) the angle of the receiver position relative to the rupture propagation (directivity). This dependency is thoroughly investigated both for a homogeneous medium and a heterogeneous medium in this chapter.

4.1 Parameter Studies – Homogeneous Case

In this section, this dependency is investigated for a homogeneous medium (with parameters shown in Table 4.1). The working area is shown in Fig. 4.1. At first, seismic motions on the surface grids of the working area (Table. 4.1) from a set of double-couple point sources (strike angle 90° , rake angle 0° , ramp source time function and rupture area of $1 \times 1 \text{ km}^2$) at different depths, 1 km from each other, are calculated and stored (Fig. 4.2 solid circles). The seismograms recorded at the surface grids, 1 km from each other, are the numerical Green's functions defined in chapter 3. With appropriate horizontal space shifting, numerical Green's functions corresponding to a planar vertical fault (Fig. 4.2, hollow circles) can be acquired. With the method developed in chapter 3 (equation 3.9), these numerical Green's function can be used to calculate the ground motions for a large earthquake with pre-chosen appropriate kinematic rupture processes.

Implementation of Different Sub-fault Sizes

How the fault plane is discretized into sub-faults of different size is described in the following. The fault plane is always assumed to be sub-divided into equilateral squares, different in side-length, see Fig. 4.3. The four neighboring sub-faults, side-length of 1 km, shaded with the

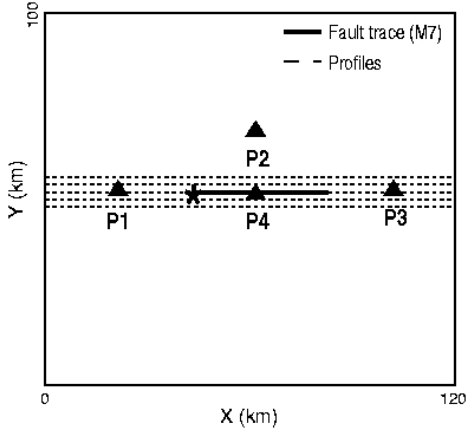


Figure 4.1: Study area for the verification of the hypothetical homogeneous medium. The fault trace of the hypothetical M7 earthquake is represented with the thick black line on which the black asterisk represents the epicentre. The five dashed black lines show the profile locations for future use. Four stations, P1, P2, P3 and P4 (black solid triangles) are used for future illustration.

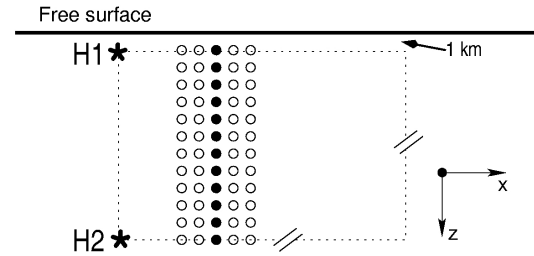


Figure 4.2: Schematic set-up for the homogeneous case. The thick black line is the free surface. Black solid circles are the hypocentres of a set of double-couple point sources. The fault plane is represented by the thin dashed rectangle (which is uniformly discretized and represented with cycles, solid and open). Big asterisks, H1 and H2, show the two example hypocentre location.

Table 4.1: Verification setup

Grid length (m)	1000
Time step (s)	0.082
S-wave velocity (m/s)	3900.0
P-wave velocity (m/s)	6754.8
Density (kg/m^3)	2811.0
Slip velocity (m/s)	2.9
PML Nodes padded	15
Simulation time (s)	50
Study area (km)	$120 \times 100 \times 45$
PML Nodes padded	15

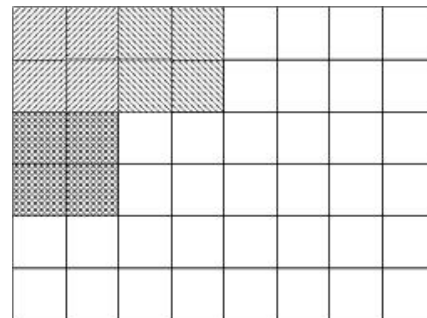


Figure 4.3: Fault plane discretization with sub-fault of different sizes. A larger sub-fault with $2 \times 2 \text{ km}^2$ is taken as an example.

same pattern are combined to produce a larger sub-fault, side-length of 2 km. The kinematic source parameters for those small sources located in the larger sub-fault, i.e., the static slip, the slip velocity and the rupture velocity, are the arithmetic mean value of those of the four individual sub-faults. Following the same way, solutions of larger sub-faults can be achieved. The numerical Green’s functions (NGFs) are kept the same which defines the travel path effect and source mechanism between one point of the fault plane and one station on the surface.

Kinematic Rupture Process

The parameters for those kinematic rupture processes are defined in the following way. The fault dimensions of this Mw 7 earthquake is chosen as 36×24 km which, finally, can be evenly sub-divided into sub-fault of sizes, 2×2 , 3×3 , 4×4 km, to investigate the sub-fault size effect on the calculation accuracy, and posed such that the strike direction is parallel to the x -axis of the study area. The top of the fault plane is set to be 1 km from the free surface (Fig. 4.2) and the hypocentre is fixed at left fault side (Fig. 4.2) based on the fact that most large earthquakes are found out to be uni-lateral in terms of the rupture propagation. The rupture propagates radially from the hypocentre to the other parts of the fault plane with a constant velocity. The scalar moment M_0 is related to the moment magnitude Mw as $\log M_0 = 1.5M_w + 16.05$ (Kanamori, 1977). The final average slip D is calculated as $D = M_0/(\mu A)$ where μ is the elastic modulus and A is the ruptured area. The slip function for each sub-fault in the time domain is assumed to be a ramp function (Fig. 4.4 left) whose rise time (τ_i , Fig. 4.4 right) is calculated as the ratio between the local static slip and the presumed constant slip velocity (Table 4.1). The final slip distribution is generated following the 2D Gaussian function, see Mai and Beroza (2000, equation (1)) and scaled to the forward mentioned average slip. The auto-correlation lengths in the strike direction and the dip direction are chosen to be 17.2 km and 5.8 km, respectively, which followed the results of a strike slip Mw 6.9 earthquake in Table 2 of Mai and Beroza (2000). The final slip distribution is show in Fig. 4.5.

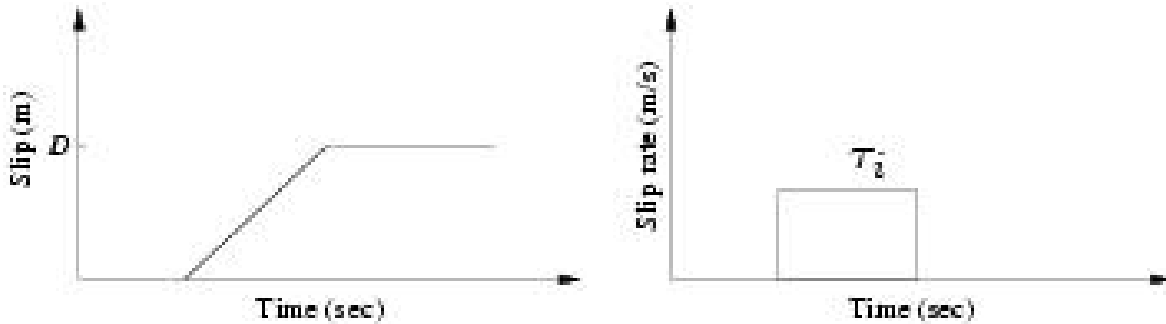


Figure 4.4: Slip time function (left) and slip rate time function (right) adopted. τ_i is the rise time of the i th sub-source. The constant slip rate value equals to s_i/v_{rup} , and v_{rup} is assumed to be constant at 3.1 m/s.

Accuracy Measurement

The solution of the 1×1 km (equal to the grid-length) is considered as the “continuous” solution and used to measure the accuracy of differently discretized solutions. The misfit energy (ME) between the seismograms of the discretized solutions with sub-faults (like 2.0×2.0 km²,

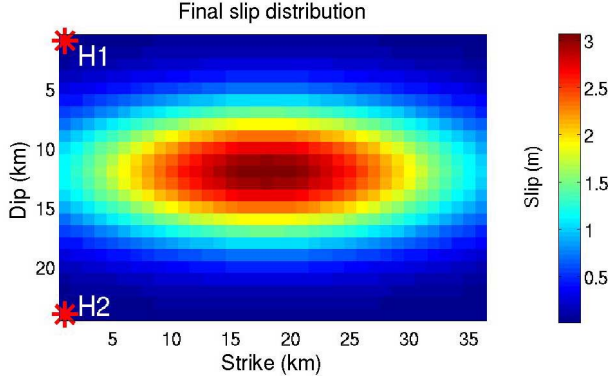


Figure 4.5: Final slip distribution. Gaussian function (following [Mai and Beroza, 2000](#)) in the space domain is adopted. H1 and H2 mark two hypocentres at different depth.

$3.0 \times 3.0 \text{ km}^2$ and $4.0 \times 4.0 \text{ km}^2$, respectively), and the “continuous” solution is adopted for the comparison:

$$ME = \frac{\sum_{i=1}^{nt} [v_c(i\Delta t) - v_d(i\Delta t)]^2}{\sum_{i=1}^{nt} (v_c(i\Delta t))^2} \quad (4.1)$$

where $v_c(i\Delta t)$ is the velocity amplitude of the “continuous” solution and $v_d(i\Delta t)$ is that of the discretized solution at time $i\Delta t$, respectively. ME equals 0 means the two seismograms are identical and thus no misfit is introduced by the increasing of the sub-fault size. The larger the ME, the more misfit is introduced by the increasing of the sub-fault size .

First Comparison

We show the velocity seismograms simulated with hypocentre H1 (Fig. 4.5) on a few profiles (dashed lines in Fig. 4.1) which are parallel to the fault trace in Fig. 4.6. The fault trace is located in the position of $y = 52 \text{ km}$ (Fig. 4.1). The rupture velocity is assumed to be constant at 2.34 km/s and the resulting velocity seismograms are low-pass filtered at frequency of $1/3 \text{ Hz}$ with Gaussian function. The maximum ME for one horizontal component, x -component, on the profile of $y = 52 \text{ km}$ where the fault trace is located, is about 109% which is much larger than that for the other two components. With increasing distance from the fault trace to 2 km , that value for x -component decreases to 4.7 %, much faster than the other two components. At the profile of $y = 54 \text{ km}$, the ME for the x -component already decreases to 4.5% and 1.7% at the profile location $y = 56 \text{ km}$ which is smaller than that for the y -component, 5.9%. Thus we conclude that in most of the study area, except the narrow band region surrounding the fault trace, the y -component of velocity will receive more effect due to the sub-fault size increasing. In this chapter we will always take the y -component to illustrate the simulation accuracy to be on the safe side.

Four stations, P1, P2, P3 and P4 (black solid triangles in Fig. 4.1), are chosen and the Fourier amplitude spectra of the velocity seismograms corresponding to the different solutions are shown in Fig. 4.7. Considering where the rupture starts (H1 in Fig. 4.1), the station P1 is in backward direction of the rupture propagation, the station P2 is located in the middle of the fault trace but 16 km above, the station P3 is in the direction of the rupture propagation and the station P4 is right in the middle of the fault trace. At the station P3, there is almost no difference between the velocity Fourier amplitude spectra from different solutions. The

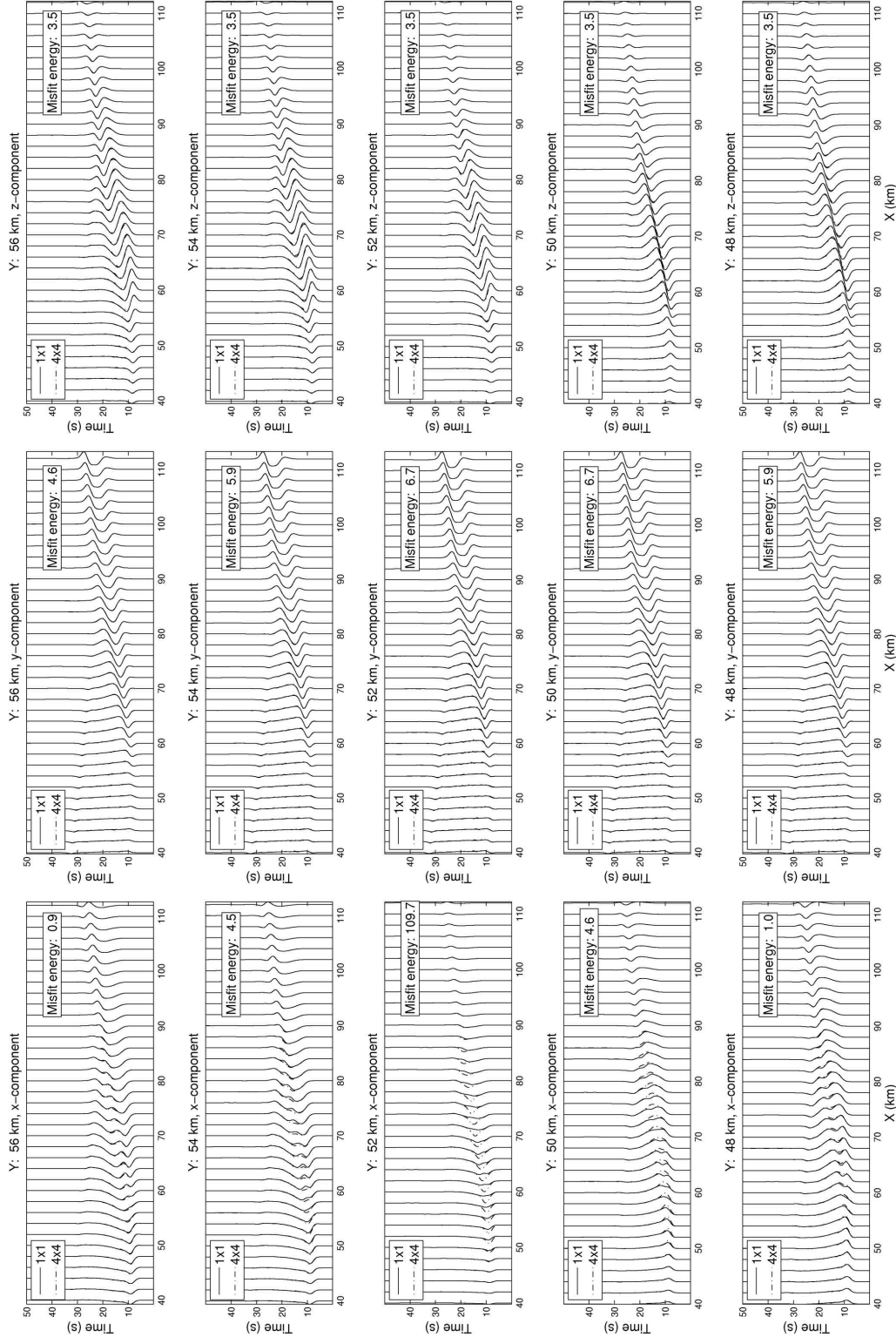


Figure 4.6: Velocity profiles from two discretized solutions, side-lengths of 1×1 and 4×4 km. From left to right are the x -, y - and z -components. The profiles are parallel to the fault trace, and the location are shown in the title of each sub-figure (dashed lines in Fig. 4.1). The maximum misfit energy (ME), see definition in the text) across each profile is shown in the inlet in percentage. The fault trace is located at $y = 52$ km (thick black line in Fig. 4.1).

frequency where those spectra become different is smaller for the station P1 than that for the station P2. For the station P4, when the sub-fault size is increased to 4×4 km, for the x -component, the Fourier amplitude is totally different from the other three solutions, even in the low frequency range while this is not observed in the other two components. This illustrates the extremely high ME value (109%) right on the fault trace in Fig. 4.6. We will not put too much attention on this narrow band but focus on the rest of the working area. The y -component has comparable ME value in most working area as in the fault trace and thus will be adopted to illustrate the parameter variation on the simulation accuracy when the source is differently discretized.

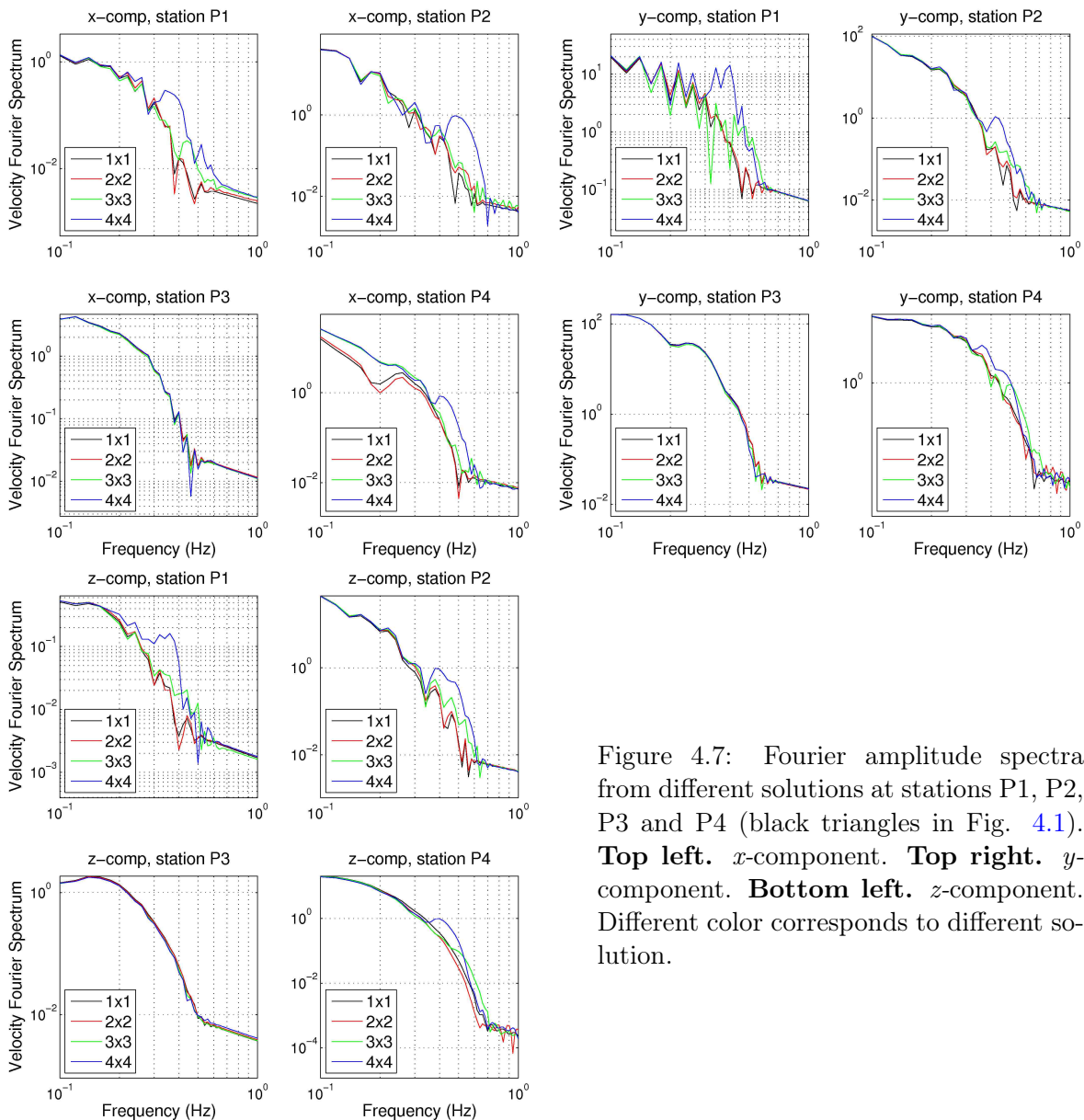


Figure 4.7: Fourier amplitude spectra from different solutions at stations P1, P2, P3 and P4 (black triangles in Fig. 4.1). **Top left.** x -component. **Top right.** y -component. **Bottom left.** z -component. Different color corresponds to different solution.

4.1.1 Directivity Effect

The directivity effect depends on the relative angle between a station and the rupture propagation which starts from the hypocentre. Since most large earthquakes are found to be unilaterally breaking, we fix the hypocentre at the left side of the fault plane (Fig. 4.5). We take two hypocentres with different depth, H1 and H2 (Fig. 4.5, red asterisk), to investigate the hypocentre depth effect on the simulation accuracy when the fault plane is differently discretized.

First, in Fig. 4.8 left, the ME distribution on the surface between the different solutions and the “continuous” solution is shown to exhibit the directivity effect on the simulation accuracy. The rupture starts from the hypocentre H1 and propagates to the other part of the fault plane with a constant velocity of 3.9 km/s. The resulting seismograms are low-pass filtered at frequency of 1/3 Hz (3.0 sec). For the solution of 4×4 km, in the triangle area right behind the rupture propagation, the ME values are larger than those in the other area (except the fault trace).

We then change the hypocentre to a deeper one – H2, keep the other parameters unchanged and synthesize the ground motion. The misfit energy distribution between the larger discretization of the fault plane and the “continuous” solution is shown in Fig. 4.8 right. The largest ME for the solution of 4×4 km is around 1.76 % , smaller than that for H1. We thus conclude that when the station is in the position with a larger angle with the rupture propagation, the simulation accuracy gets worse when the fault plane is represented with larger sub-faults. The shallower the hypocentre, the larger is the misfit introduced by the discretization of the fault plane. In the following, we will keep focus on the worst case and just show the results for hypocentre H1.

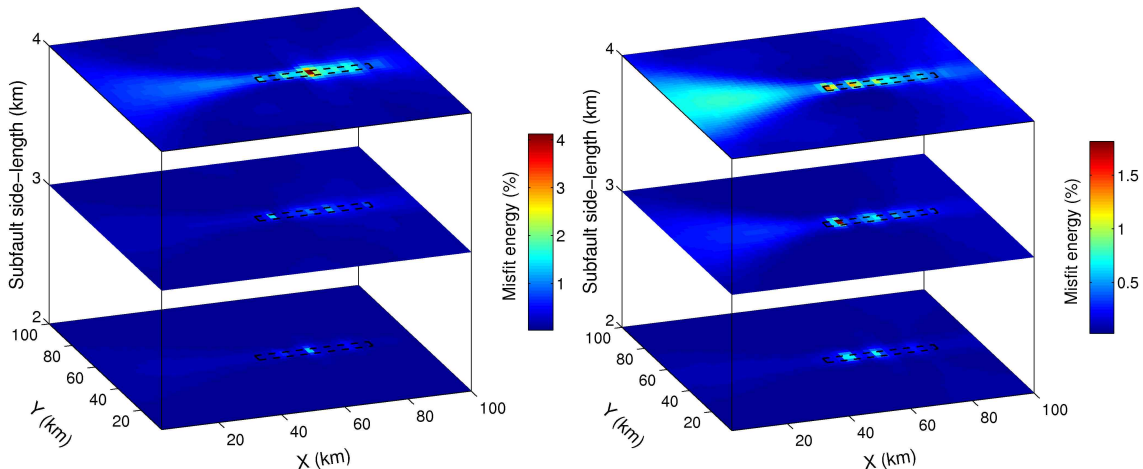


Figure 4.8: Hypocentre depth effect on the ground motion accuracy from discretized sources. Misfit energy between the seismogram (y -component) of one discretized solution (i.e., 2×2 km, 3×3 km and 4×4 km, vertical axis) and the “continuous” solution is shown over the study area. **Left.** Hypocentre H1 (Fig. 4.5). **Right.** Hypocentre H2 (Fig. 4.5). Fault trace is marked with the black dashed rectangle to avoid masking the fault projection.

4.1.2 Rupture Velocity

In our source description, the time when one sub-fault begins to rupture is the smallest integration of the variable – hypocentre distance divided by rupture velocity. The arrival time of the rupture front is inversely affected by the rupture velocity. We take two rupture velocity 2.34 km/s (60% of the shear wave velocity) and 3.9 km/s (100% of the shear wave velocity), and synthesize the individual Green’s function with different sub-faults (i.e., 2×2 km, 3×3 km, 4×4 km), and compare the velocity seismograms with those of the “continuous” solution in Fig. 4.9 in terms of ME distribution. Fig. 4.9 left corresponds to those results synthesized with rupture velocity of 2.34 km/s and Fig. 4.9 right corresponds to rupture velocity of 3.9 km/s. The rupture starts from H1 and the resulting ground motion is low-pass filtered at a frequency of 1/3 Hz with a Gaussian function. The ME in the triangular region right behind the rupture propagation, Fig. 4.9 left, is smaller than that in Fig. 4.9 right which means the larger the rupture velocity adopted, the less misfit introduced by the discretization of the fault plane. The possible lowest rupture velocity related to the source scenario generation will decide the largest sub-fault size.

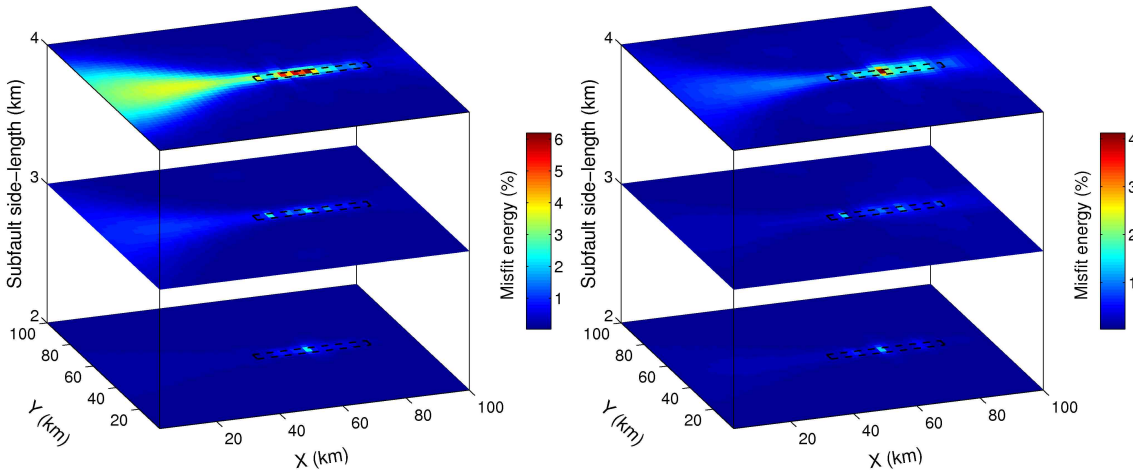


Figure 4.9: Rupture velocity effect on the ground motion accuracy from discretized sources. Misfit energy between the seismogram (y -component) of one discretized solution (i.e., 2×2 km, 3×3 km and 4×4 km, vertical axis) and the “continuous” solution, for which different rupture velocity is used, over the study area is shown. **Left.** Rupture velocity of 2.34 km/s. **Right.** Rupture velocity of 3.90 km/s. Fault trace is marked with the black dashed rectangle to avoid masking the fault projection region.

4.1.3 Cut-off Frequency

The resulting ground motions have to be filtered (low-pass) at some cut-off frequency to eliminate numerical dispersion. Two frequencies (smaller than the one required by the finite difference method, i.e., 0.5 Hz), 0.33 and 0.25 Hz, are chosen and used to low-pass filter the resulting seismograms synthesized with different discretized solutions of the source (i.e., 2×2 km, 3×3 km, 4×4 km). The filtered motions from the discretized solution and the “continuous” solution are related by the misfit energy (ME) for the entire surface. These ME

distribution on the working area are shown in Fig. 4.10 in two parts corresponding to two cut-off frequencies (Fig. 4.10 left and Fig. 4.10 right). For the discretized solution of sub-fault 4×4 km (Fig. 4.10), the ME in the triangle area behind rupture propagation for the case of a cut-off frequency of 0.33 Hz (Fig. 4.10 left) area, is larger than that in the same region for the case of a cut-off frequency of 0.25 Hz (Fig. 4.10 right) which means the larger the cut-off frequency, the larger is the misfit introduced by the discretizing of the fault plane.

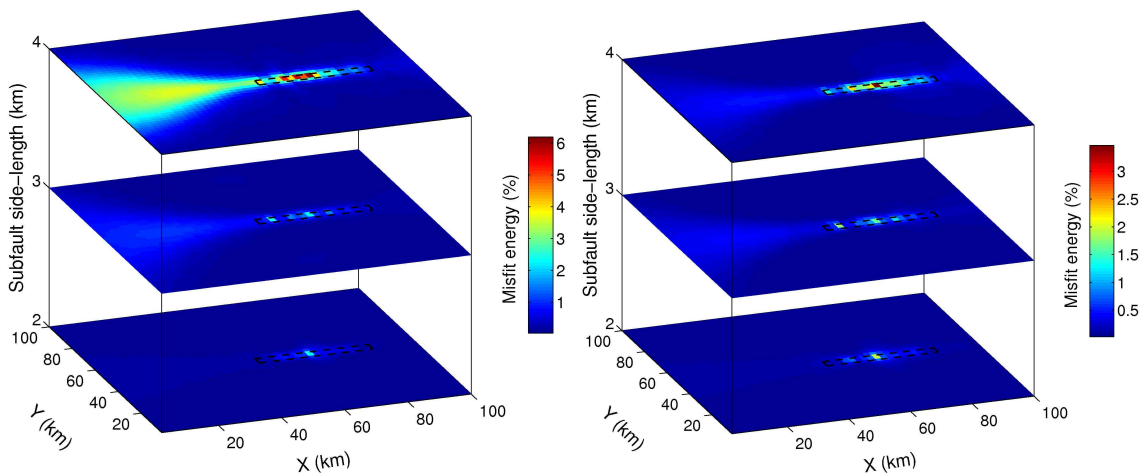


Figure 4.10: Cut-off frequency effect on the ground motion accuracy from discretized sources. Misfit energy (ME) between the seismogram (low-pass filtered with different cut-off frequencies) of one discretized solution (i.e., 2×2 km, 3×3 km, 4×4 km, vertical axis) and the “continuous” solution is shown over the study area. **Left.** Cut-off frequency of 0.33 Hz. **Right.** Cut-off frequency of 0.25 Hz. The y -component of velocity is adopted.

4.1.4 Sub-fault Size

The key point about the discretization of the fault plane is how big the sub-fault could possibly be. To get that value, how the misfit introduced by the discretization of the fault plane (into elemental sub-faults) changes with the sub-fault size should be investigated. We can observe that trend from Fig. 4.8, Fig. 4.9 and Fig. 4.10. With the increase of the sub-fault size, the ME of the entire working area is getting larger. Therefore we conclude that the growth of the sub-fault size will lead to more misfits to the synthesized seismic motions.

4.2 Conclusions and Hints to the Future Work

In order to simulate an earthquake or fault system with a larger number of rupture processes, we developed a new method named Numerical Green’s function method. First we test the accuracy of this method with a few of hypothetical earthquake simulations.

A pilot study is carried out for a homogeneous medium to investigate how different parameters will affect the accuracy of our method comparing to the true solution, in our work we take the quasi-continuous solution. Several parameters could affect the simulation of the finite fault earthquakes. First we investigate how the wave form is affected by these parameters. The misfit energy between two seismograms (discretized vs. “continuous” solutions) are

adopted to calibrate the accuracy. Our conclusions are: (1) the bigger the rupture velocity, the more accurate is the synthesis; (2) the accuracy of the synthesis at different receivers is affected by the directivity effect; (3) the accuracy of the synthesis decreases with the growth of the sub-fault size; (4) the accuracy of the synthesis decreases with the cut-off frequency used to filter the ground motions.

This quantitative research shows us the basic trends of how the misfit introduced by the discretization of fault plane varies with different parameters in a homogeneous media. With these results we can move to a real 3D media and choose a seismically active fault or fault system. We choose the Los Angeles basin as our major working area and investigate the optimal sub-fault size for this area in the following chapter.

Chapter 5

NGF Data-Base

There are lots of seismically active regions in the world which could be used as our working area. The Los Angeles basin has high population and industrial density and is known as an area of high seismic risk. Plenty of studies have been carried out for the basin structure investigation for a better earthquake risk assessment. Also many studies have been done to reveal the fault and fault system buried in this region. Thus we choose this region as our target for the trial of our method. In this chapter we present the necessary information about the seismicity, the velocity structure and the target fault geometry in 3D. The necessary verification in terms of sub-fault size is redone for our 3D target area. Some theories about the wave propagation in the near-source region are shown here to provide some basic knowledge for people unfamiliar with this topic.

The physics about the wave propagation in the near-source is briefly described to provide some fundamental knowledge for a better presentation and discussion of the results.

5.1 Los Angeles Basin

The greater Los Angeles region is tectonically complex and seismically active. From the geological point of view, the Los Angeles basin is a deep sedimentary basin. This basin is located at the junction of the northern Peninsular Ranges and the central Transverse Ranges. During Miocene time, the basin started to build up through a pull-apart process (Wright, 1987). Five million years ago, the opening Gulf of California migrated the boundary between the Pacific and the North America plates to the San Andreas fault (SAF) east of the basin. This geological process created a left step (known as the Big Bend) along a right-lateral strike slip SAF north and east of the basin (Atwater, 1989). As moving in the NW direction toward the Big Bend, the region started to undergo compression. Following basin evolutions are involved volcanism, uplift, extension, block rotation, pulling apart, shear faulting, compression, and folding (e.g., Campbell and Yerkes, 1976; Wright, 1987). At the present time the sediments in the central basin are more than 10 km thick which form a northwest-southeast elongated synclinorium whose flanks are folded and cut by a group of Quaternary active faults (Ziony and Yerkes, 1985).

Present day crustal deformation, south of the basin, is dominated by NW-trending strike slip faults (e.g., the SAF, the San Jacinto fault (SJF), the Elsinore fault, and the Newport-Inglewood fault). East of the basin, the SJF merges with the SAF. The Whittier-Elsinore fault system, the Newport-Inglewood fault, and the Palos Verdes fault cut through the east and

west flanks of the basin (Ziony and Yerkes, 1985). In the north of the basin, a frontal thrust fault system has pushed up the San Gabriel Mountains. This fault system is defined by the Sierra Madre-Cucamonga fault system along the SE and the Santa Susana fault along the SW. The Santa Monica Mountains have been uplifted by the E-W trending Malibu-Santa Monica-Raymond Hill fault system (Davis et al., 1989). Beneath most of the central and western Transverse Ranges, horizontal detachment in the lower crust or at the Moho boundary has been suggested (e.g., Bird and Rosenstock, 1984; Weldon and Humphreys, 1986; Namson and Davis, 1988; Huftile and Yeats, 1995). Furthermore, six major thrust or oblique fault systems have been identified in and around the Los Angeles basin area by recent geomorphological and trenching studies (Dolan et al., 1995): the Sierra Madre-Cucamonga system, the Los Angeles basin fault system, the Santa Monica Mountains fault system, the Oak Ridge fault system, the San Cayetano fault, and the Palos Verdes fault. Dolan et al. (1995) have presented the detail description of the locations and scale of thrust and horizontal detachments occurring in the region.

Earthquakes also help illuminate the tectonics of the Los Angeles basin. Earthquake focal mechanisms show a mixture of NW dextral strike slip and N-S convergence (Hauksson, 1990). Earthquakes of right lateral strike slip faulting represented by the 1933 M 6.4 Long Beach earthquake dominate the seismicity south of the basin. North of the basin, many of the earthquakes have thrust mechanisms, often coupled with left-lateral displacements. Examples include the 1971 San Fernando M 6.6, the 1987 Whittier Narrows M 5.9, the 1991 Sierra Madre M 5.8, and the 1994 Northridge M 6.7 earthquakes (Working Group on California Earthquake Probabilities [WGCEP], 1995).

Across the basin from San Pedro to Mt. Wilson, about 10 mm/yr convergence is revealed by early geodetic studies in the Los Angeles basin (Cline et al., 1984). However, the data available at that time were not good enough to make the estimate very accurate. North of the basin, Cheng et al. (1987) investigated more than ten years of trilateration measurements. They estimated 6 mm/yr convergence normal to the SAF along a NW profile from the Malibu fault to the White Wolf fault. Little convergence within the San Gabriel Mountains normal to the SAF was found by Lisowski et al. (1991) when adopting the updated trilateration data. Shen (1991) revealed about 3 mm/yr convergence along the southern frontal fault system. Taking the advantage of combining the Very Long Baseline Interferometry (VLBI) and GPS measurements, Feigl et al. (1993) reported 5.0 ± 1.2 mm/yr shortening from Palos Verdes to JPL which is located in the SW foothills of the San Gabriel Mountains. West of the basin, 7-10 mm/yr N-S convergence across the Ventura Basin was determined by Donnellan et al. (1993) using GPS methods. Recently, Sany et al. (1995) found that the SAF is located near the center of a deformation band.

One of the most recent significant earthquake event affecting southern California was the January 17th 1994 Northridge Earthquake. At 4:31 A.M. on Monday, January 17, a moderate but very damaging earthquake with a magnitude of 6.7 struck the San Fernando Valley. In the following days and weeks, thousands of aftershocks occurred, causing additional damage to affected structures. Fifty-seven people were killed and more than 1,500 people seriously injured. For days afterward, thousands of homes and businesses were without electricity; tens of thousands had no gas; and nearly 50,000 had little or no water. Approximately 15,000 structures were moderately to severely damaged, which left thousands of people temporarily homeless. 66,500 buildings were inspected. Nearly 4,000 were severely damaged and over 11,000 were moderately damaged. Several collapsed bridges and overpasses created commuter havoc on the freeway system. Extensive damage was caused by ground shaking, but earthquake

triggered liquefaction and dozens of fires also caused additional severe damage. This extremely strong ground motion in large portions of Los Angeles County resulted in record economic losses.

The Southern California Earthquake Center (SCEC) has supported an effort to develop a standard 3D reference model for southern California. This velocity model integrates data from multiple disciplines, including seismic imaging, geologic mapping, and geotechnical investigations, and thus is capable to capture the wide range of spatial scales that are important for both basic research and extensive earthquake hazard applications which are necessitated because the dense population and active tectonics in this area and includes precise earthquake location determinations, path and site effect studies, and strong ground motion simulations. These studies require a real three-dimensional (3D) seismic velocity model defined on spatial scales appropriate for those applications.

We apply the NGF method to the Newport Inglewood (NI) fault system located in the Los Angeles basin (Fig. 5.1). An area of $96 \times 87 \times 25.5$ km, in the two horizontal and vertical directions, is selected as study area, and rotated in order to have one horizontal grid axis parallel to the NI fault. The velocity model is based on the elastic part of the SCEC 3D velocity model for the Los Angeles (LA) basin (Version 3, Kohler et al. (2003)). The main goal of the current study is to demonstrate the NGF concept and its functionalities. The depth of a shear wave velocity isosurface, 2.0 km/s, is shown in Fig. 5.2. To reduce the computation work and the size of the data base we truncate the seismic velocities at 1.4 km/s. The basin part with shear wave velocity less than 1.4 km/s is artificially set to 1.4 km/s.

5.2 Newport-Inglewood Fault

The Los Angeles Basin was opened by the tectonic forces of the Pacific plate moving against the North American plate. The primary tear in the rocks that marks this boundary is the San Andreas Fault (transform fault). The break is not just one simple tear but occurs in a broad swath across southern California that includes numerous right lateral strike slip, reverse, normal and thrust faults. The tectonic plate movements are shared by these faults. One of the faults, the Newport-Inglewood Fault diagonally crosses the Long Beach city. It was on this fault that the famous 1933 Long Beach Earthquake occurred. This fault is still considered the most probable source for an earthquake in the Long Beach area. The California Geological Survey has estimated that an earthquake of Magnitude 7.0 is credible on the Newport-Inglewood Fault in the Long Beach area.

The Long Beach, Airport, Recreation Park and Seal Beach oil fields occur along the Newport-Inglewood Fault. The super-giant Wilmington Oil Field occurs between the Newport-Inglewood Fault and the Palos Verdes Fault. Each oil field is formed by rock deformations producing folded geologic strata and by the faulting. Each oil field has numerous faults. Only the faults within the Newport-Inglewood Fault Zone are considered active (movement within the last 11,000 years).

Although the most famous of the faults, the San Andreas, is capable of producing an earthquake with a magnitude of 8+ on the Richter Scale, Seismologists believe that a 6.0 earthquake on the Newport-Inglewood Fault would result in far more death and destruction to the Long Beach city than a “great” quake on the San Andreas, because the San Andreas is relatively remote from the urban centers of southern California. The Newport-Inglewood Fault, on the other hand, runs along or near the coastline of Los Angeles and Orange Counties

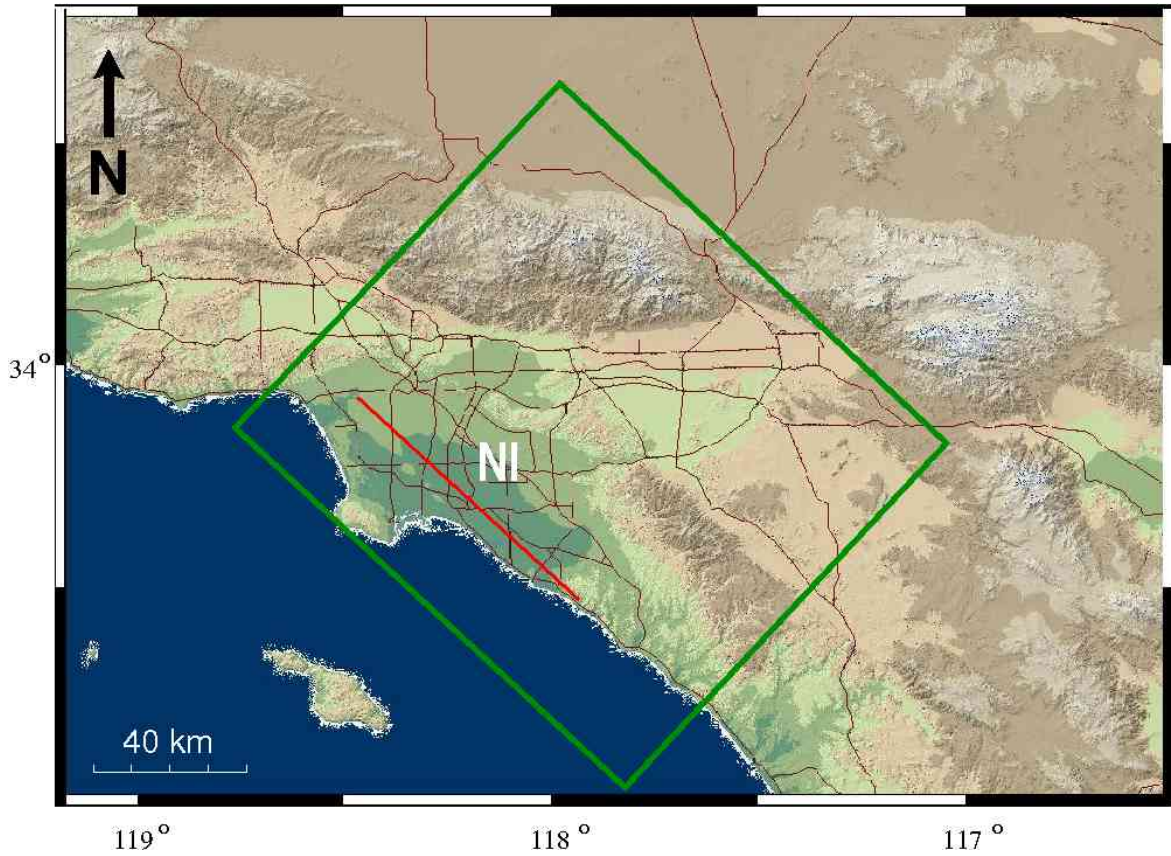


Figure 5.1: Los Angeles area with modeled region (green rectangle) and the idealized Newport-Inglewood fault (NI, red line).

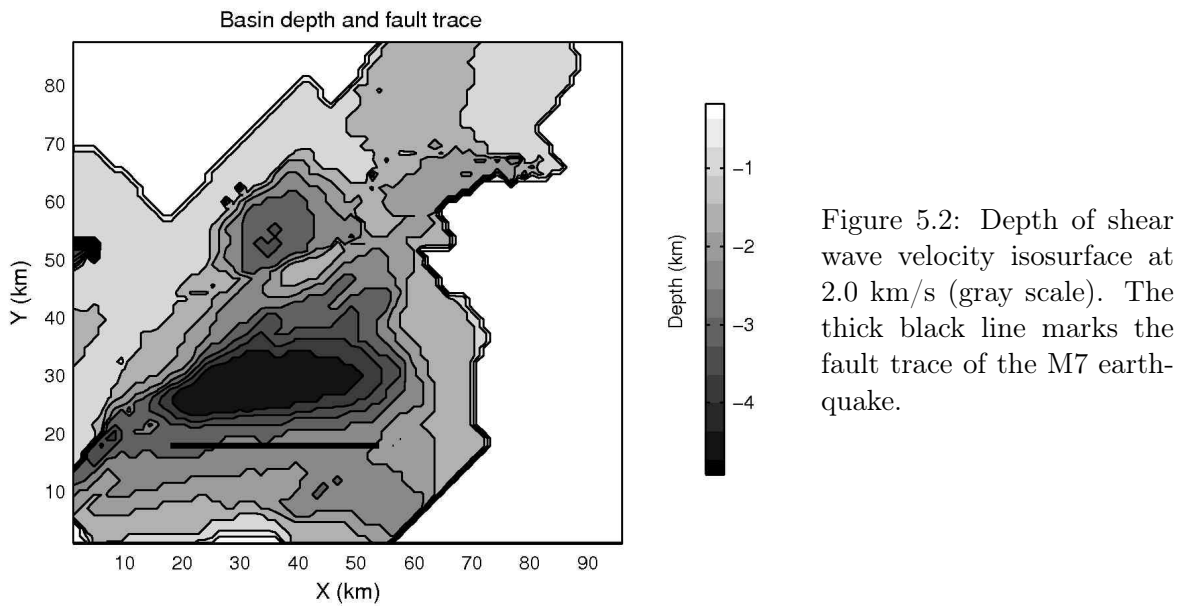


Figure 5.2: Depth of shear wave velocity isosurface at 2.0 km/s (gray scale). The thick black line marks the fault trace of the M7 earthquake.

and directly through the heart of Long Beach. The rupture of this fault was the cause of the 1933 Long Beach Earthquake that killed 115 people (e.g., Barrows, 1974; Hauksson and Gross, 1991; Yeats, 2001).

To sum up, the NI fault is chosen for several reasons: it hosted the M6.4 Long Beach earthquake in 1933, causing serious damage; it is still considered the most probable source for a damaging earthquake to the LA area; the near-vertical plane (Fig. 5.3) can be approximated by a vertical plane to first order in the numerical calculation and the predominant right-lateral slip can be approximated with a pure strike-slip mechanism (Grant and Shearer, 2004).

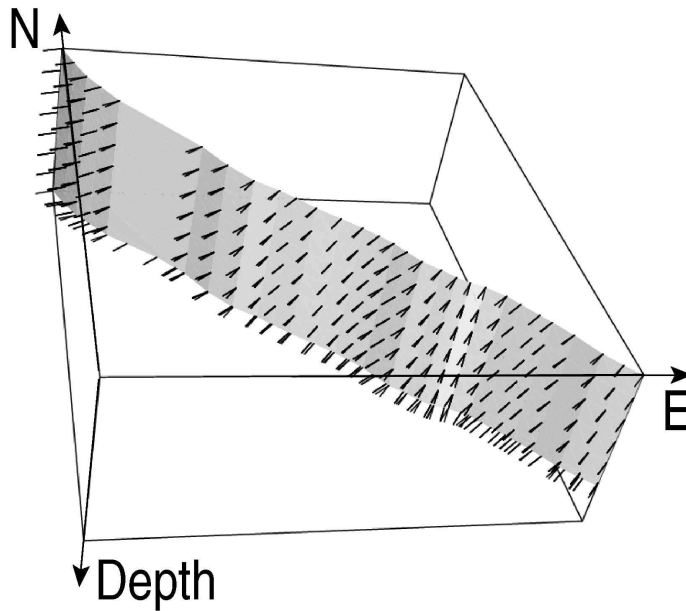


Figure 5.3: Newport Inglewood fault plane. The spatial extension of this fault plane is calculated with the program developed by SCEC Community Fault Model. Small arrows represent the normal vector of the fault plane. The size of the fault plane is $69 \times 20 \text{ km}^2$ (Jennings, 1994).

5.3 Verification: Heterogeneous Medium

The accuracy of the synthesized ground motions as a function of sub-fault size is investigated for an Mw 7 earthquake with the computational setup and source parameters given in Table 5.1 (what should be pointed out is that the grid distance is decreased to 0.3 km to fulfill the requirement by the finite difference method). The fault length L and width W are chosen to be 36 km and 18 km, respectively, with the aim that the final fault geometry will be 120×60 (in grid points), which can be divided into sub-faults with size of 3×3 , 4×4 , 5×5 and 6×6 (in grid points). The top of the fault plane is 1.5 km from the free surface. An Mw 7 finite fault earthquake scenario (quasi-dynamic rupture process calculated with the method of Guatteri et al. (2004), 2D Gaussian auto-correlation function with an isotropic correlation-length of 5 km is adopted, and the final slip distribution is shown in Fig. 6.1) is simulated with three different equilateral sub-faults of side-length 0.3 km (treated as the “continuous” solution, corresponding to the finest grid distance), 1.5 km, and 1.8 km. The ground motions for the latter two sub-fault sizes are compared to those for the “continuous” solution.

As an indicator of the accuracy we compare the peak ground velocity (PGV) over the whole study area covering frequencies up to 0.5 Hz. This choice is somewhat arbitrary and other wave-field characteristics could be used (e.g., shaking duration, or a misfit criterion w.r.t. the

Table 5.1: Verification setup for the heterogeneous model in the Los Angeles basin

Spatial discretization (km)	0.300
Temporal discretization (s)	0.01811
Lowest S-wave velocity (km/s)	1.400
Simulation time (s)	65
Number of cells	$350 \times 320 \times 100$
PML Nodes	15
Fault area (km ²)	18×36
Top Depth (km)	1.5

“*continuous*” solution). Our specific goal here is to demonstrate that hazard-relevant variations due to finite-source scenarios can be efficiently carried out using the NGF methodology.

The relative PGV difference – the PGV difference (x -component) between one discretized solution (sub-fault size of 1.8 km) and the “*continuous*” solution, divided by the PGV of the “*continuous*” solution – is adopted and shown in Fig. 5.4a. The largest relative difference is 9.79% in the position of the PGV at 0.838 m/s.

The waveforms from different solutions are almost identical in the profile shown in Fig. 5.4c with lowest peak correlation coefficient value of 0.988. This can also be seen from the waveform comparison (Fig. 5.4b) for one single station where the biggest relative PGV difference is observed (point P1, Fig. 5.4a). The maximum amplitude difference between the solution for 1.5 km sub-fault side-length and the “*continuous*” one is 0.039 m/s (4.6% in percentage) while that for the solution for 1.8 km is 0.083 m/s (9.79% in percentage). Thus we conclude that solution for 1.5 km sub-fault side-length is accurate enough and can be applied to the generation of the NGF data base.

These results justify the choice of the final parameter setup used to calculate a complete set of NGFs for M7 earthquakes on the NI fault estimated to cover an area of 69×20 km² (Jennings, 1994) (shown in Fig. 5.5 as thick black rectangle). As we primarily focus on differential effects we calculate a fault area of 40 (along strike) \times 13 (along depth) (60×19.5 km² from the north west edge of the NI fault (area covered with small rectangles in Fig. 5.5) to save the total amount of calculation with consideration that this area is also capable to cover the historical Long Beach earthquake, M6.4) sub-fault NGFs (side length 1.5 km) for a grid spacing of 300 m and seismograms up to 0.5 Hz. The complete NGF data base includes all 6 motion components (three translations and three rotations), for the 140×166 equally spaced surface grid points at 600 m distance, and for all sub-faults.

This verification is also carried out in terms of acceleration in case of investigation about this kind of motion. The peak ground acceleration is adopted and the misfit between the discretized solution, the one with side-length of 1.8 km, and the “*continuous*” solution, over the peak ground acceleration of the “*continuous*” solution are shown for the entire study area in Fig. 5.6. As for the velocities, the x -component is used for this illustration. The largest misfit introduced by the discretization is about 12% which is larger than that for the velocity (9.79%) and happens at different station.

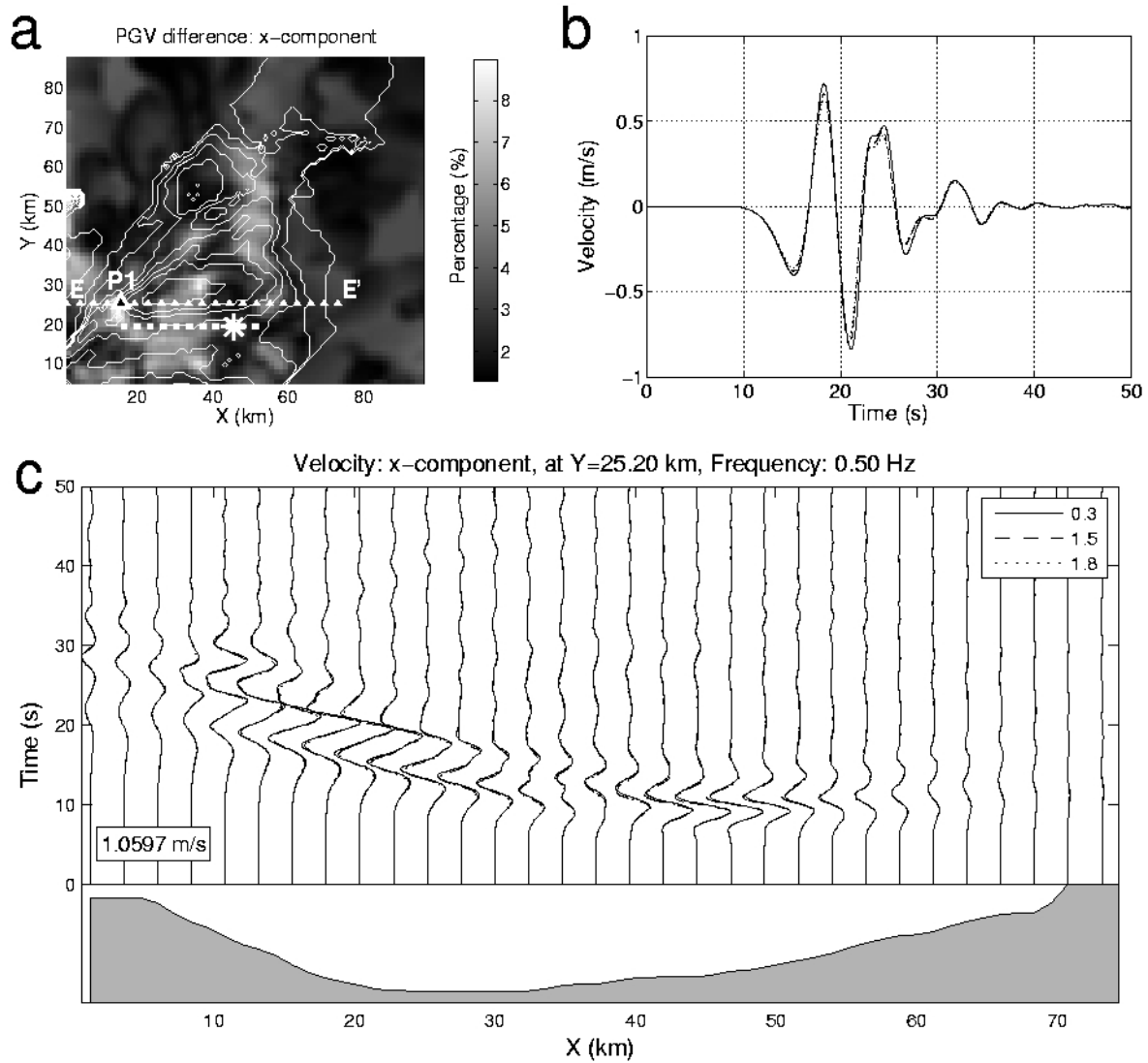


Figure 5.4: Optimal sub-fault size determination for an M7 earthquake in LA basin. **a.** Relative PGV difference distribution (in percentage, see definition in the text) between the discretized solution of 1.8 km and the “continuous” solution. The dashed thick white line marks the fault trace and the big asterisk marks the epicentre. The biggest relative PGV difference is observed at station P1. **b.** Velocity seismograms of differently discretized solutions, i.e. 0.3 km, 1.5 km and 1.8 km, respectively, for station P1 (**a**). **c.** Velocity profile, EE’ (**a**), of differently discretized solutions. The gray area at the bottom shows the isosurface depth of shear wave velocity at 2 km/s.

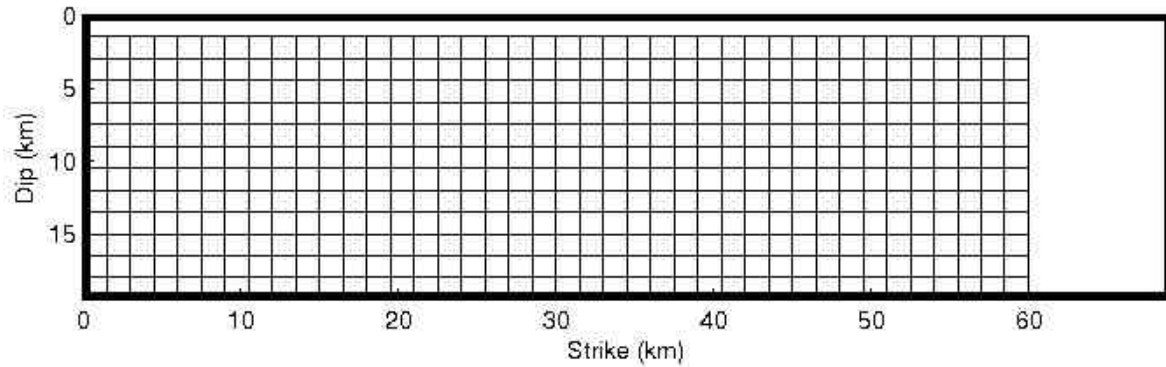


Figure 5.5: Numerical Green's function calculation setting up. The thick black rectangle is the approximate fault plane of Newport Inglewood. Each small rectangle represents a sub-fault whose numerical Green's function is calculated and stored. The free surface is located at 0.

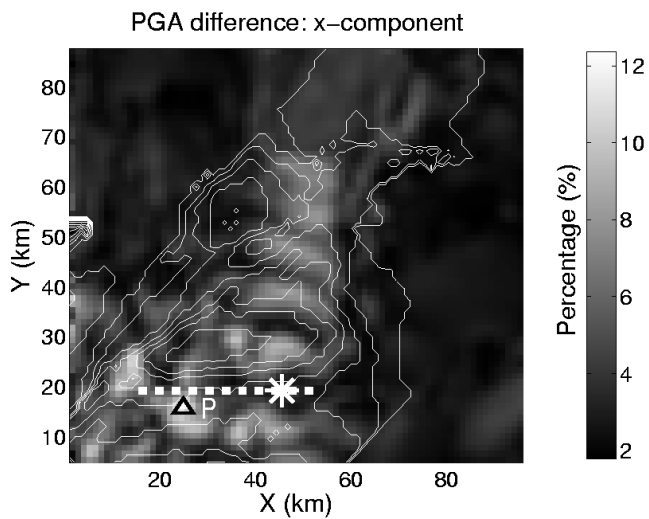


Figure 5.6: Verification of the optimal sub-fault size for M7 earthquakes in terms of acceleration. Relative peak ground acceleration (PGA) difference compared with the “continuous” solution (same definition as the relative PGV difference in text) is shown for the solution of 1.8 km. The thick dashed white line marks the fault trace on which the white asterisk represents the epicentre. The curved white lines are the contours of shear wave velocity isosurface at 2.0 km/s. P is the station where the largest misfit is observed.

5.4 Near-Source Wave Propagation Physics

In the near-field region, the wave propagations are affected by the source complexity and the sub-surface structure. To provide some basic knowledge to people unfamiliar with this topic, we briefly describe the physics about wave propagation in this chapter. The translational and rotational parts of seismic motions are included.

5.4.1 Velocity

Strong earthquakes of the past decade have revealed particularly destructive effects of motions in the vicinity of faults. Seismologist has identified the forward directivity and fling effects as the primary characteristics of near-fault ground motions. These characteristics make near-fault earthquakes unique compared to far field ground motions, which nearly all seismic design criteria are based on. Ground motions in the near source region of large crustal earthquakes are significantly affected by rupture directivity. This effect is strongest at longer periods ($T > 1$ s) and they can have a significant impact on engineered structures. Conventional record processing techniques can typically fully recover directivity pulses. In this section we will discuss the theory and the observation on this effect which will provide the theoretical basis for the future work.

Aki and Richards (2002) presented one source model – point double-couple shear dislocation which has been proven to be the most successful one. Assume a shear dislocation located in the (x_1, x_2) plane which is located in the center of a Cartesian coordinate system x_1, x_2, x_3 (Fig. 5.7). In the local area of one station, the polar coordinates, r, θ, ϕ is defined as specified in Fig. 5.7. The slip direction is along the x_1 axis. Thus, the corresponding displacement field, $u(x, t)$ using the time dependent seismic moment $M_0(t) = \mu \langle \Delta u(t) \rangle A$, associated with a shear dislocation (Fig. 5.7) parallel to a fault surface with area A , shear modulus μ , and average slip $\langle \Delta u(t) \rangle$ across the fault is:

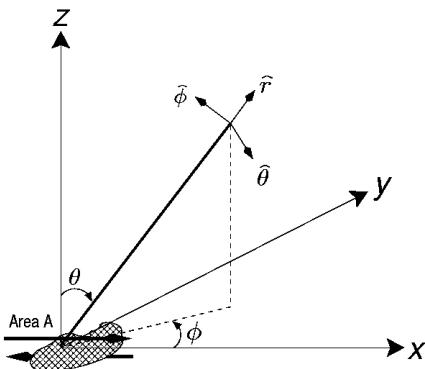


Figure 5.7: Cartesian and spherical polar coordinates for analysis of radial and transverse components of displacement radiated by a shear dislocation of area A and average slip \mathbf{u} (Aki and Richards, 2002).

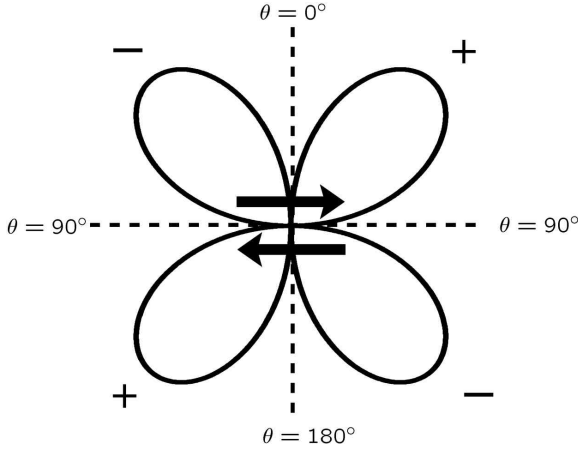


Figure 5.8: Radiation pattern (in plane $\{\phi = 0, \phi = \pi\}$) of the radial component of static displacement field due to a double couple point source.

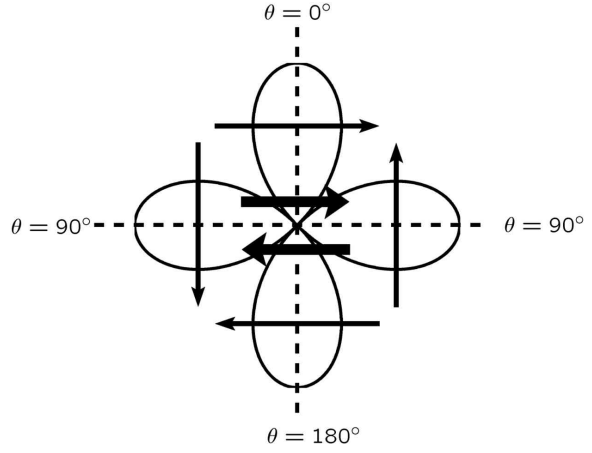


Figure 5.9: Radiation pattern (in plane $\{\phi = 0, \phi = \pi\}$) for SH wave displacement excited by a double couple point source. Four straight arrows point out the direction of the static displacement.

$$\begin{aligned}
 \vec{u}(x, t) = & \frac{1}{4\pi\rho} A^N \frac{1}{r^4} \int_{\frac{r}{v_s}}^{\frac{r}{v_p}} \tau M_0(t, \tau) d\tau \\
 & + \frac{1}{4\pi\rho v_p^2} A^{IP} \frac{1}{r^2} M_0\left(t - \frac{r}{v_p}\right) \\
 & + \frac{1}{4\pi\rho v_s^2} A^{IS} \frac{1}{r^2} M_0\left(t - \frac{r}{v_s}\right) \\
 & + \frac{1}{4\pi\rho v_p^3} A^{FP} \frac{1}{r} \dot{M}_0\left(t - \frac{r}{v_p}\right) \\
 & + \frac{1}{4\pi\rho v_s^3} A^{FS} \frac{1}{r} \dot{M}_0\left(t - \frac{r}{v_s}\right).
 \end{aligned} \tag{5.1}$$

The radiation patterns, A , in each term are given by:

$$\begin{aligned}
 A^N &= 9 \sin 2\theta \cos \phi \hat{r} - 6(\cos 2\theta \cos \phi \hat{\theta} - \cos \theta \sin \phi \hat{\phi}), \\
 A^{IP} &= 4 \sin 2\theta \cos \phi \hat{r} - 2(\cos 2\theta \cos \phi \hat{\theta} - \cos \theta \sin \phi \hat{\phi}), \\
 A^{IS} &= -3 \sin 2\theta \cos \phi \hat{r} + 3(\cos 2\theta \cos \phi \hat{\theta} - \cos \theta \sin \phi \hat{\phi}), \\
 A^{FP} &= \sin 2\theta \cos \phi \hat{r}, \\
 A^{FS} &= \cos 2\theta \cos \phi \hat{\theta} - \cos \theta \sin \phi \hat{\phi}
 \end{aligned}$$

where \hat{r} , $\hat{\theta}$, and $\hat{\phi}$ are unit direction vectors in a spherical polar coordinate system for the source receiver geometry (Fig. 5.7). The superscripts N , I , and F represent the near field, intermediate, and far field terms, respectively, while P and S denote P and S waves, respectively. In the far field, the radiation pattern consists of a radial component, proportional to $\sin 2\theta \cos \phi \hat{r}$ (Fig. 5.8), and a transverse component, proportional to $\cos 2\theta \cos \phi \hat{\theta} - \cos \theta \sin \phi \hat{\phi}$ (Fig. 5.9).

Directivity

When an earthquake occurs, the velocity at which the fault ruptures is approximately the same as the velocity at which shear waves emulate (Somerville, 2002). The accumulated energy is concentrated into the form of a short duration, high amplitude pulse perpendicular to the fault because shear waves are of transverse wave type (Fig. 5.9). The same effect is not observed in the rear of fault rupture direction. As a result the energy is spread over a long duration, and the earthquake record is similar to those of far field earthquakes. The fault normal component of the Rinaldi ground motion velocity history is shown in Fig. 5.10a. Recorded during the 1994 Northridge earthquake, the Rinaldi station was approximately 7.1 km from the fault. As can be seen in the figure, the Rinaldi ground motion showed a clear and distinguished forward directivity pulse. Fig. 5.10b presents the velocity history of the El Centro ground motion recorded from the 1940 Imperial Valley earthquake. The El Centro station was approximately 8.3 km away from the fault but the site was located in the rear of fault rupture direction. A high-amplitude, short duration pulse was not seen in the fault normal component and the ground motion resembles a typical far field ground motion.

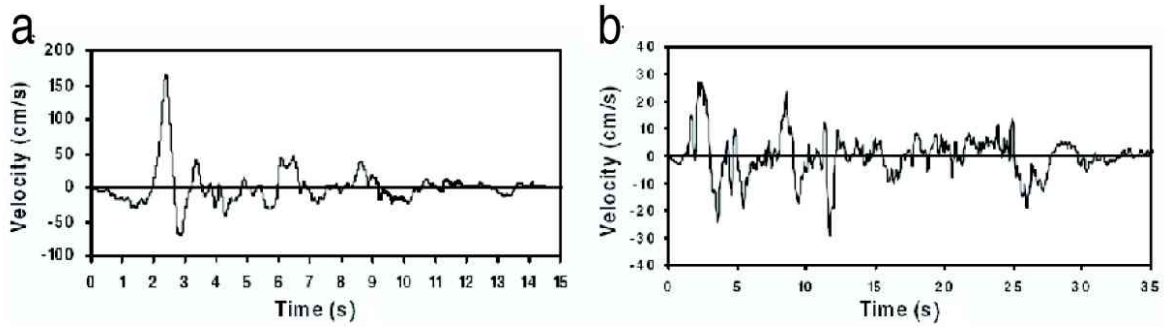


Figure 5.10: Velocity histories of Rinaldi (a) ground motion and El Centro (b) ground motion

5.4.2 Rotation

Cochard et al. (2006) presented the solution of the static rotation field, $\omega(x, t)$, for a double couple point source (slip function $M_0(t)$), in an infinite homogeneous, isotropic medium (with density of ρ , shear wave velocity β and P -wave velocity α) as:

$$\omega(x, t) = \frac{-A^R}{8\pi\rho} \left[\frac{3}{\beta^2 r^3} M_0 \left(t - \frac{r}{\beta} \right) + \frac{3}{\beta^3 r^2} \dot{M}_0 \left(t - \frac{r}{\beta} \right) + \frac{3}{\beta^4 r} \ddot{M}_0 \left(t - \frac{r}{\beta} \right) \right] \quad (5.2)$$

where

$$A^R = \cos \theta \sin \phi \hat{\theta} + \cos \phi \sin 2\theta \hat{\phi} \quad (5.3)$$

is the radiation pattern of the three components (one radial component being zero and two transverse components). This radiation pattern is plotted in Fig. 5.11. Comparing with the radiation pattern of the far-field shear wave displacement (Fig. 5.9), it is expected that more directivity should be observed in the fault-parallel component of rotation instead of the fault-perpendicular component which happens in the translation part of ground motion.

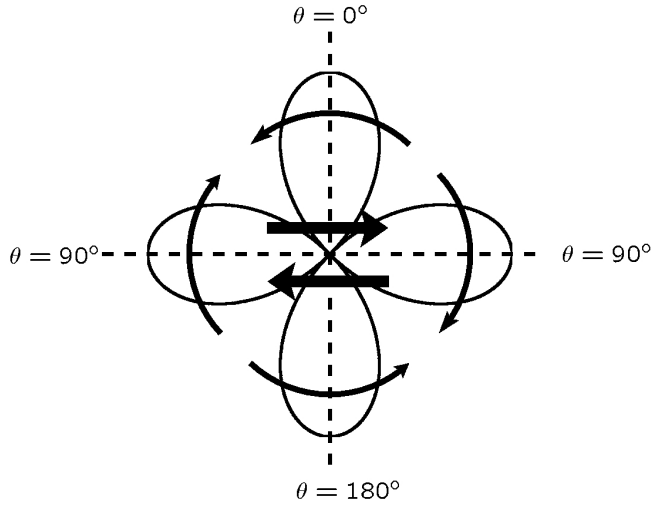


Figure 5.11: Radiation pattern (in plane $\{\phi = 0, \phi = \pi\}$) of static rotation field for a double couple point source (Cochard et al., 2006). Four curved arrows indicate the direction of the static rotation.

5.5 Conclusions

In this chapter we thoroughly describe the working area and the target fault system. Due to the limitation of the finite difference method, the velocity was truncated at a specific shear-wave velocity. In other words, the media are restricted to firm rock from the view point of all popular definition of local site condition. Thus the strong effect due to the near surface soil structure can not be considered during the numerical Green's function generation which could be reinforced in the future by taking the advantages of some other tools. Also the wave propagation is restricted to the iso-tropic, elastic part. The fault plane is also simplified and represented by a vertical plane which is not true somewhere, especially at the northwest tip where the fault system is found to be multi-segment.

After settling down the major region, we verify the optimal sub-fault size for earthquakes simulated with a quasi-dynamic rupture process and present the quantitative results. With a heterogeneous media presented, the misfit is different than that of the homogeneous media, especially at the region where the basin depth changes very fast. In this verification, only one quasi-dynamic process is adopted while the fact is that the more rupture process is implemented and verified against the misfit energy, the more secure is the quantitative result, at least in the region surrounding the fault plane where the source scenario will strongly affect the seismic motions.

Since it is hard to provide an analytical solution to the wave propagation problem in a 3D media, we take the solution with sub-fault size equal to the grid-length coherent with the numerical method, as the "continuous" solution and use it as the true continuous solution to measure the misfit led by the discretization of the source. Thus the quantitative result about the optimal sub-fault size strongly depends on the way how we approximate the true continuous solution. The smaller the grid-length adopted, the tinier piece the fault plane is discretized into, and the more accurate is the approximate "continuous" solution compared with the true continuous solution. Anyway, the quantitative results will insure us inside a certain accuracy range when the numerical Green's function data base is built up.

Because our working area is restricted to the near-field region, the near-field and intermedia term of the wave propagation physics are compatible to the far-field term with respect to the controlling of the ground motion. In order to provide some basic physics to help people without pre-knowledge to understand the illustration of our future results, we describe the complex

wave propagation in this region. At the mean time, how the rotational part of ground motion varies inside this region is also discussed.

With the NGF data base we begin to synthesize a few earthquakes with different source parameters. The aim is to provide the spatial map about how the peak ground motions change inside the study area. The first source parameter took into account is the hypocentre location which can be located anywhere of the seismogenic zone. The next chapter will focus on this topic.

Chapter 6

Application: Hypocentre Location Effect

¹ **ABSTRACT:** As the first example we use the data base to estimate variations of surface ground motion (e.g., peak ground velocity (PGV)) due to hypocentre location for a given final slip distribution. The results show a complex behavior, with dependence of absolute PGV and its variation on asperity location, directivity and local structure. Hypocentral depth may affect PGV in a positive or negative way depending on the distance from the fault and the location with respect to basin structure. The calculations are compared to another research. And confirmative conclusions are acquired about that comparison.

6.1 Introduction

A question of considerable practical relevance to estimates of seismic hazard is how variations of the hypocentre location for a given final slip distribution influence the shaking for a characteristic earthquake of a given magnitude. The kinematic explanation for that question is: an earthquake is a shear dislocation that begins at a point on a fault and spreads at a velocity that is almost as large as the shear wave velocity. The propagation of fault rupture toward a site at a velocity close to the shear wave velocity causes most of the seismic energy from the rupture to arrive in a single large pulse of motion that occurs at the beginning of the record. This pulse of motion represents the cumulative effect of almost all of the seismic radiation from the fault. The radiation pattern of the shear dislocation on the fault causes this large pulse of motion to be oriented in the direction perpendicular to the fault plane, causing the strike-normal component of ground motion to be larger than the strike-parallel component at periods longer than about 0.5 seconds. However, not all near-fault locations experience forward rupture directivity effects in a given event. Backward directivity effects, which occur when the rupture propagates away from the site, give rise to the opposite effect: long duration motions having low amplitudes at long periods. The conditions for generating forward rupture directivity effects are readily met in our data-base generation, i.e., strike-slip faulting, where the rupture propagates horizontally along strike either unilaterally or bilaterally, and the fault slip direction is oriented horizontally in the direction along the strike of the fault.

Amongst many other possibilities, this is the question we will focus on in this sample study.

¹A manuscript on this chapter is ready for submission to Geophys. J. Int.

6.2 Seismogenic Zone

An earthquake occurs when elastic strain that has gradually accumulated across a fault is suddenly released in the process of elastic rebound. The elastic energy stored on either side of the fault drives the motion on the fault. Active rupture area can vary from a few m² for the weakest detectable earthquakes to several thousands of km² for large earthquakes. In continental zones the depth range of earthquake origins, the so called seismogenic layer spreads from shallow depth to a maximum of 10 to 30 km depending on the individual region and its tectonic setting. The bottom limit of this seismogenic zone is associated with a mechanical limit below which deformations are released in plastic flow. There also observations that there are both upper and lower seismicity cutoffs on well-developed faults (Marone and Scholz, 1988). Table 6.1 gives the depth range where 90% aftershocks happen on a few large seismic active fault planes (strike-slip mechanism) (Scholz, 1990, page 131).

Table 6.1: Depth for aftershocks

Earthquake	Time range	Aftershocks	Seismogenic zone (km)
Imperial Valley	1977 – 1983	865	6.5 – 13.5
Morgan Hill	1984	720	2.5 – 10.0
Parkfield-Chalome	1966	375	3.0 – 13.0
Parkfield Section	1969–1986	630	4.0 – 13.0

Fischer and Mills (1991) reported that the 1981 Oceanside cluster (swarm of 19 $M < 3.0$ earthquakes, 100 km south of the Newport Inglewood fault) has a mean depth of 13.0 km. Morton and Miller (1981) and Fischer and Mills (1991) mapped and compiled another cluster of seven similar microearthquakes occurred offshore of Newport Beach in 2000 at a depth of approximately 6.5–7.0 km which is near the offshore of Newport Inglewood fault zone. To sum up, in order to investigate the hypocentre location effect on the ground motions, it is reasonable to restrict the seismogenic zone to the range with depths of 5–15 km.

6.3 Set up

The NGF data base thus calculated allows us - within the limits of the method (e.g., reliable frequency range) - to synthesize ground motions from arbitrary strike-slip histories on the NI fault for the complete study area. We assume the existence of a characteristic M7 earthquake on the entire NI fault and synthesize ground motions for a 4×6 regular grid of hypocentre locations in the seismogenic zone (5 - 15 km depth) as indicated in Fig. 6.1. The final slip distribution is generated randomly with a given isotropic correlation length (5 km) based on 2D Gaussian auto-correlation space function (equation 1 in Mai and Beroza, 2002). The slip histories are calculated quasi-dynamically following Guatteri et al. (2004) accounting for the accelerating tendency of the crack front due to dynamic loading and the high stress-drop promotion of fast rupture propagation. The shear-modulus on the fault is kept constant and corresponds to a shear velocity of 3.2 km/s.

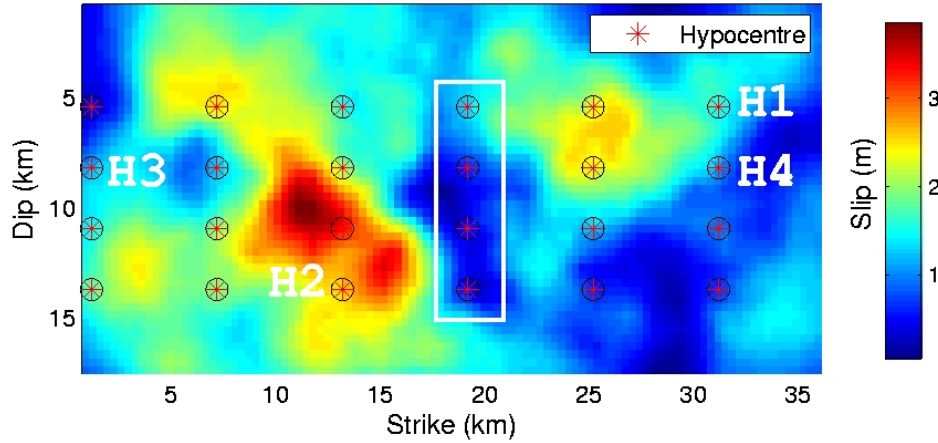


Figure 6.1: Final slip distribution of an M7 earthquake on NI fault and hypocentre grid (red asterisks, for investigation of hypocentre location effect on ground motion). H1, H2, H3 and H4 show the example hypocentre locations for more detailed discussions.

6.4 Velocity Snapshots

In Fig. 6.2, snapshots of the y -component velocity for one scenario (hypocentre H3 in Fig.6.1) on the surface are shown. Source and basin related effects on ground motion are distinct in this figure. Most energy is recorded at the area right to the fault plane due to the unilateral rupture propagation from left to right. Wave propagation is slowed down by the basin with low velocity in the area A at time 28 s. Basin amplification effect is observed in area B (time 38 s) and C (time 43 s), where largest of velocity of the whole study area, at this time, happens right at the edge of the basin.

6.5 Two Hypocentre Examples

First, the ground velocities of different components simulated with two example hypocentres, H1 and H2 (Fig. 6.1), are shown². H1 is located at the right edge of the fault plane and thus a unilateral rupture propagation is implemented into the source, whereas H2 is close to the middle of the fault plane and the rupture propagates bilaterally. The peak ground velocity (PGV) distributions are shown in Fig. 6.3.

The maximum peak ground velocities of the two horizontal components of the entire study area are equivalent and three times larger than that of the z -component. The y -component PGVs inside the small basin, region B, are larger than its neighboring area (Fig. 6.3 bottom).

In the area surrounding the north-west (NW) tip of the fault trace where the rupture propagates towards, for the example of H1, larger PGVs are observed compared with the example of H2 in y - and z -component (Fig. 6.3 middle and bottom). Whereas for the x -component, in this area, H2 leads to larger PGVs than H1.

For H1 (Fig. 6.3 Left), for all three components, the largest PGV location is close to both the NW edge of the fault plane and to the edge of the basin. The large PGV area is also very close the slip asperity area on the fault plane (Fig. 6.1). The joint contribution of the three

²All the PGV distributions corresponding to these 24 hypocentres are shown in Appendix A.

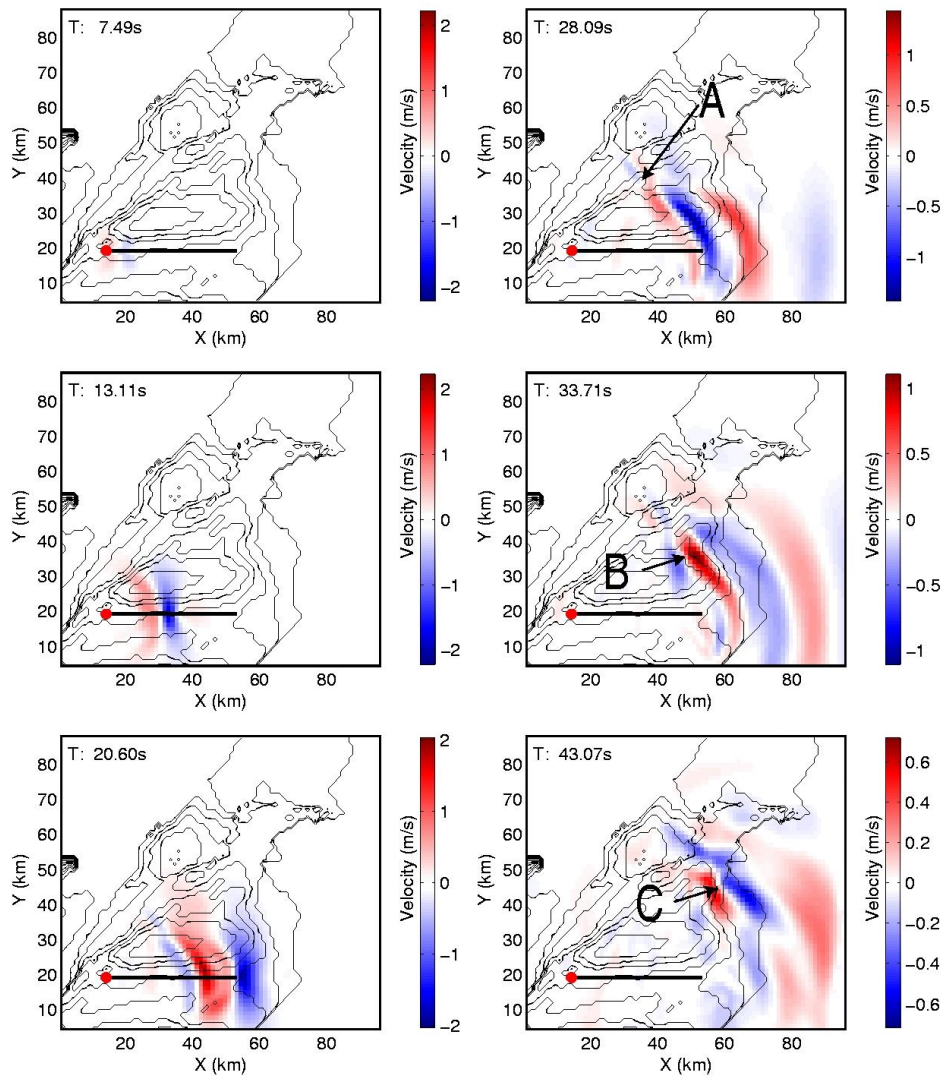


Figure 6.2: Velocity snapshots (y -component) at different times from hypocentre H3 in Fig. 6.1. Black thin lines show the contours of isosurface of shear wave velocity at 2 km/s. Thick black line shows the fault trace. Note the change of the color scale. Areas A, B and C are depicted to illustrate the structure effect on wave propagation.

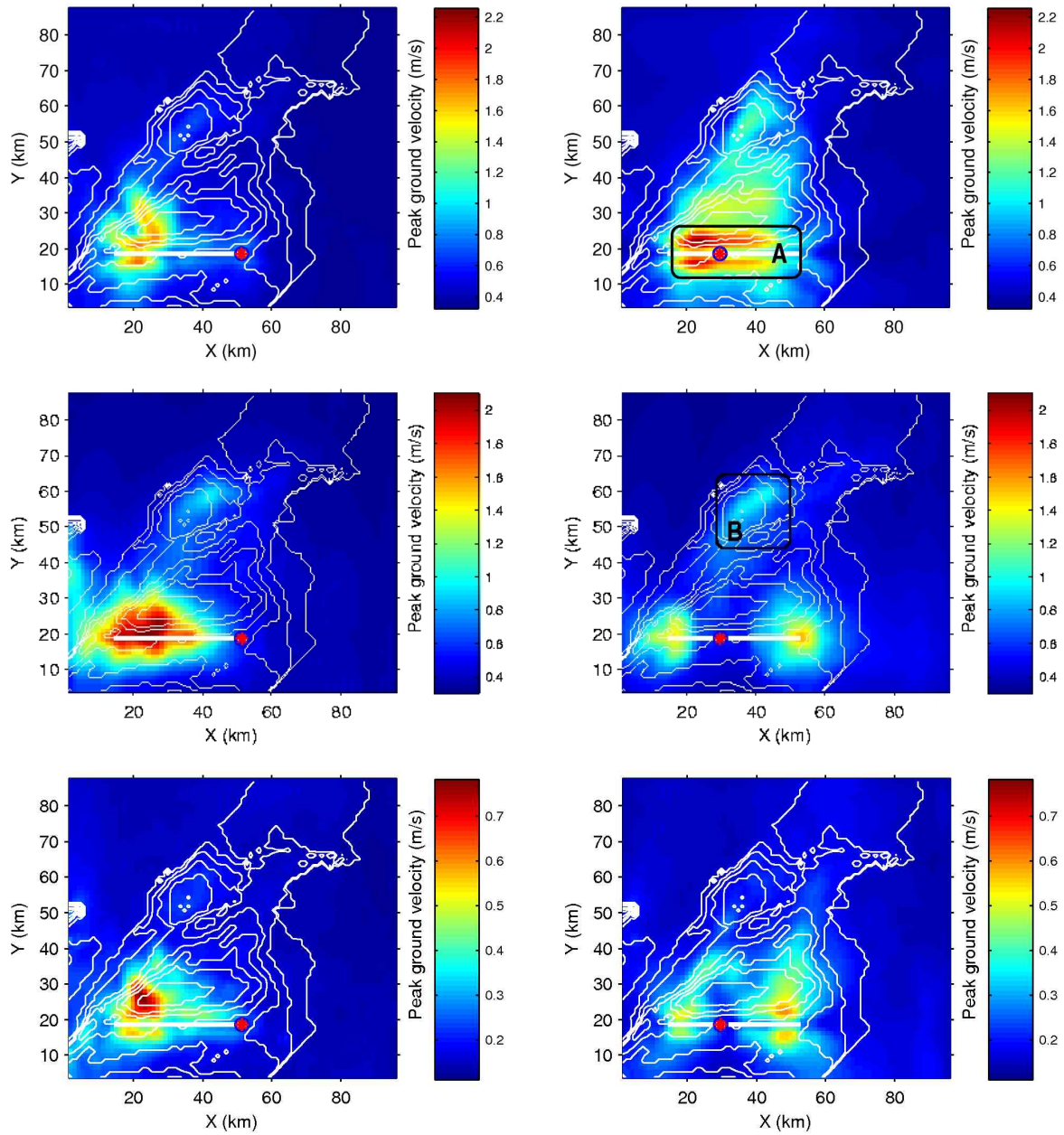


Figure 6.3: PGV distributions for two example hypocentres. **Left.** H1. **Right.** H2. From top to bottom are x -, y - and z -components, respectively. The epicentres are indicated as red asterisks. The straight white line indicates the fault trace. Thin curved white lines are contours of the seismic velocity model. Note the color scale difference between different components. Region A and B are chosen for illustration.

major effects, i.e., the forward directivity effect, the basin amplification effect and the high slip elevation, dominate the PGV distribution for this hypocentre location. Small velocity amplitudes are observed in the area behind the rupture propagation which can be explained by the backward directivity effect.

For the hypocentre H2 (Fig. 6.3 right), there are large PGVs inside the entire basin for the x -component. In the two regions surrounding the two tips of the fault trace, large PGVs are observed (y -component, Fig. 6.3 middle right). In this case the rupture starts from the middle of the fault trace and propagates bilaterally to these two regions.

Two profiles are chosen and the velocity seismograms on them are shown. The first profile (Fig. 6.4) is parallel to the fault trace, located at $y=28.80$ km and across the basin edge. For the hypocentre H1 (unilateral rupture process), in the range of $x \in [32, 48]$ km (far from the basin edge), the y -component velocity seismograms are characterized with one major impulse. Basin effects such as amplitude amplification and duration time elongation are clearly observed in the range of $x \in [15, 30]$ km for all the three components. And for the y -component velocity, the duration time and the amplitude change less than for the other two components. For H1, there are almost no perturbations in the range of $x > 50$ km where the backward directivity effect controls the seismic motion generation (this range is far from the fault plane and outside the basin).

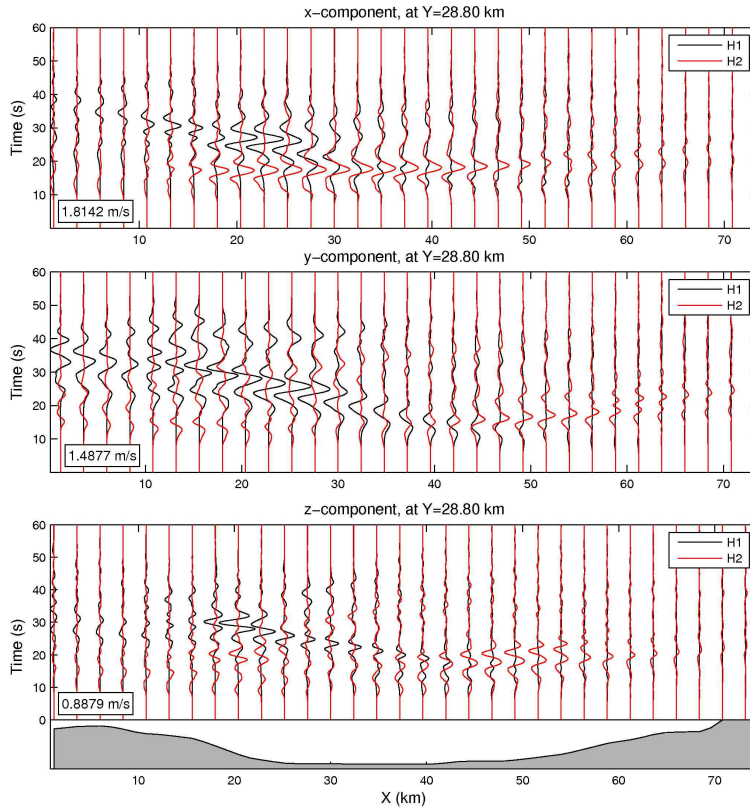


Figure 6.4: Fault parallel velocity profile for two example hypocentres. From top to bottom are the x -, y - and z -components, respectively. The shear wave velocity isosurface depth (at 2.0 km/s) is depicted in the bottom as the shadowed area. The maximum velocity amplitude across this profile is shown with the inlet number.

The second profile (Fig. 6.5) is perpendicular to the fault trace and located at $x=33.60$ km. This profile is across the fault plane, the bigger basin and the small basin (in the range of $y \in [50, 65]$ km). We first focus in a small range: $y \in [15, 20]$ km. The x -component seismograms are characterized with one major impulse while the y -component seismograms

are with two impulses. The largest velocity amplitude of the x -component (fault parallel) is 2.16 m/s which is larger than that of the y -component (fault perpendicular), 1.92 m/s. Again the basin amplification effect on the amplitude and the duration time elongation are observed for all three components. For the x - and z -component, there is a phase change of the first arrival when moving across the fault trace. The velocity amplitudes on the fault trace are very small both for H1 and H2.

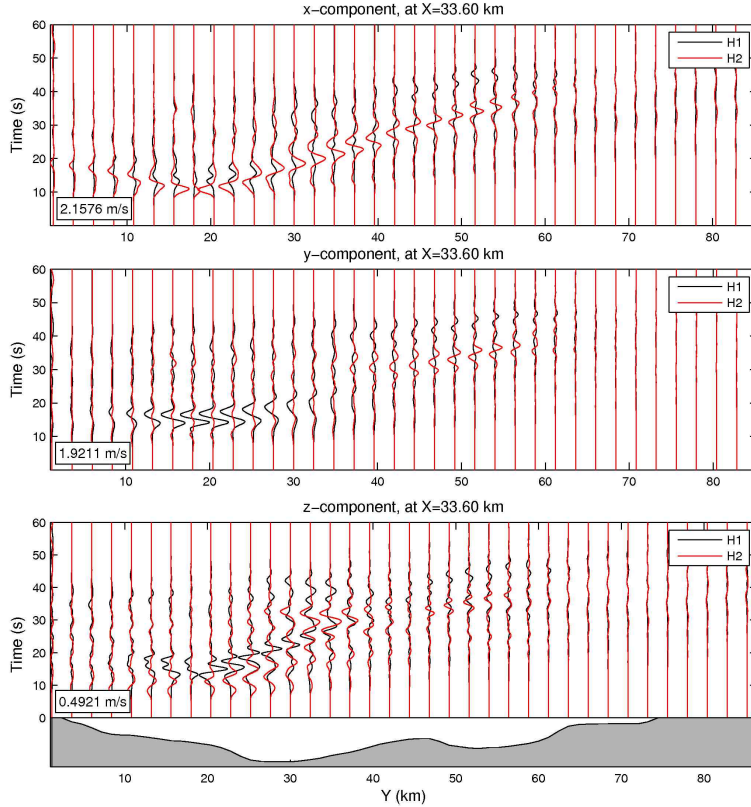


Figure 6.5: Fault perpendicular velocity profile for two example hypocentres. From top to bottom are the x -, y - and z -components, respectively. The shear wave velocity isosurface depth (at 2.0 km/s) is depicted in the bottom as the shadowed area. The maximum velocity amplitude across this profile is shown with the inlet number.

6.6 Inter-event Variations of Ground Motion

The parameter study in the hypocentre space allows us to extract the PGVs of all 24 simulations containing the dominant features of the two previously shown examples (e.g., basin wide shaking, fault-distance dependent ground motion, and ground motion elevation by the slip asperity). The variations of the hypocentre-dependent ground motions can be expressed by relating the variance and the maximum of the PGV to the mean PGV at each point of the surface grid. Two ratios are calculated and shown to characterize the variations: R_{SD} – the one of the standard deviation relative to the mean value, and R_{max} – the one between the maximum value and the mean value. The results are illustrated for all the three components in Fig. 6.6. The maximum value will provide the ground motion range excited by this set of hypothetical M7 earthquakes (different in hypocentre location). The ratios, R_{SD} and R_{max} , are used to show the possible range of the variation.

In the region B, the maximum velocity of the x -component (Fig. 6.6 top left) is compatible to that of the y -component (Fig. 6.6 middle left) and almost three times larger than that of

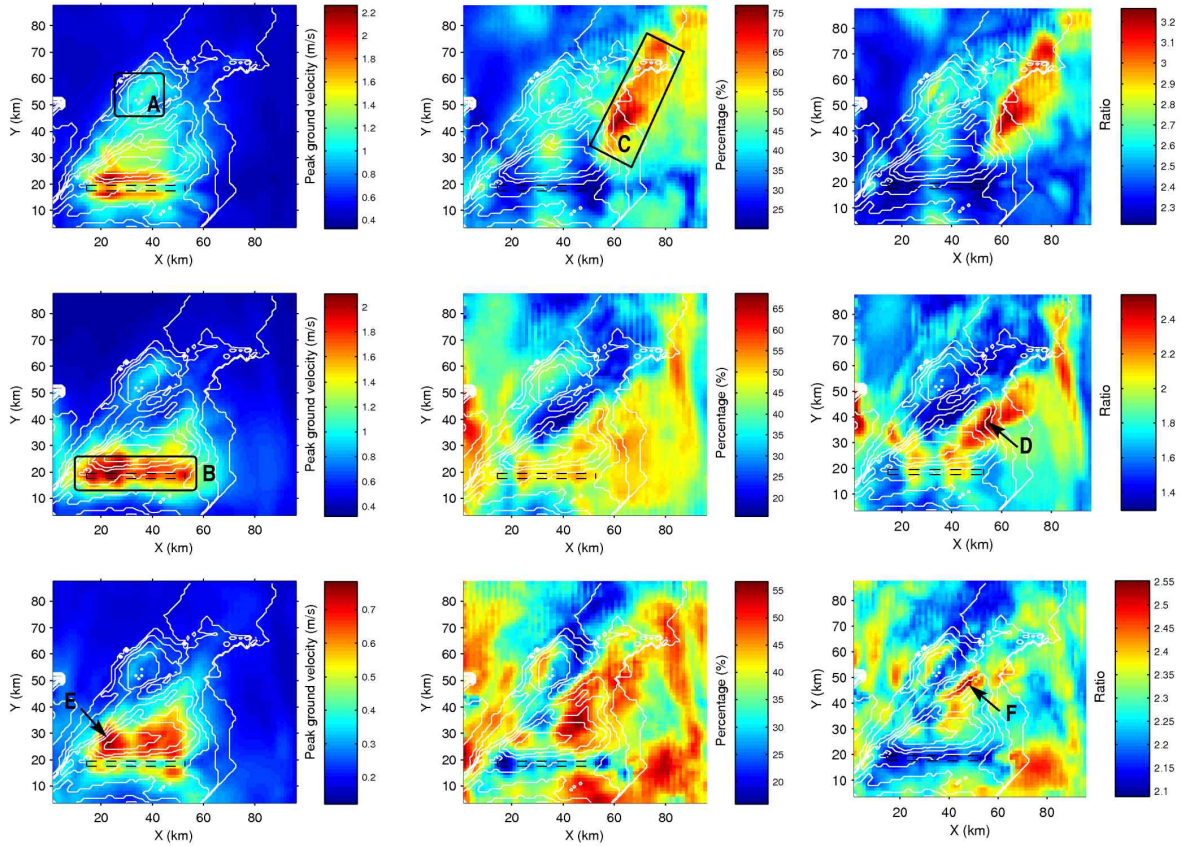


Figure 6.6: Statistics of the PGV distributions due to varying hypocentres. **Left.** Maximum value. **Middle.** The ratio between the standard deviation (SD) and the mean value (in percent). **Right.** The ratio between the maximum value and the mean value. From top to bottom are x -, y - and z -components, respectively. The dashed black rectangle indicates the fault trace. Thin curved white lines are contours of the depth of the shear wave velocity isosurface at 2.0 km/s. Regions A, B and C and stations D, E and F are picked up for more detailed discussion.

the vertical component (Fig. 6.6 bottom left). For the fault perpendicular component, the largest velocity happens right on the fault projection (Fig. 6.6 middle left), while that is not the case for the other two components (Fig. 6.6 top and bottom left). The largest velocity of the x -component is not right on but very close to the fault projection (Fig. 6.6 top left). While the vertical component velocity has the largest value at the station E which is located at the basin edge and a certain distance from the fault projection (Fig. 6.6 bottom left). Inside the basin, all three components of velocities are elevated (Fig. 6.6 left) and the x -component is the most obviously one when we focus on the small basin marked as region A.

The spatial distribution of the ratio, R_{SD} , is also shown. The distribution of this variable shows where large variation will be introduced into the ground motions when the hypocentre location is varied. The results are shown in the middle column of Fig. 6.6. For the x -component (fault parallel component), in the region C where the basin depth changes dramatically, the largest R_{SD} (around 70%) is found (Fig. 6.6 top middle). The R_{SD} in the region C is also larger than the left parts of the study area. This distribution is not observed for the other two components. For the other two components, R_{SD} is large in the regions off the two tips of the fault trace, or at stations which are located at the position with angles to the fault trace smaller than 45° . Right on the fault projection, the R_{SD} of the fault perpendicular component (y -component) is around 50% and larger than that of the other two components. For the x - and z -components, whereas, smaller R_{SD} is observed right on the fault projection, when compared to the neighboring regions. In the small basin (region A), there is always large R_{SD} observed when compared to the neighboring area, which distinctly indicates that the medium will also amplify the variations.

The spatial distributions of the ratio R_{max} (between the maximum value and the mean value) are shown in the right column of Fig. 6.6 for all three components. For the x -component, the distribution of this ratio is quite similar to that of the ratio R_{SD} (between the standard deviation and the mean value). Both the largest R_{max} and the largest R_{SD} happen at the same location, namely in the region C. The largest R_{max} for the x -, y - and z -components over the entire study area are around 3.3, 2.5 and 2.5, respectively, while the smallest ratios are 2.2, 1.3 and 2.1. R_{max} of the vertical component is distributed inside a much narrower band than the other two components. The expansion in terms of R_{SD} is almost equal between different velocity components. The slight difference is the different structure amplification effect on the y -component (at station D) and the z -component (at station F). For the y -component, the largest R_{max} over the entire study area is located at station D at the basin edge. Since station F is right above the middle of the fault projection where the directivity effect is small, focusing on the R_{max} at this station for the z -component, we conclude that the structure has bigger contribution to the variation of this ratio than the ratio R_{SD} .

Observing the different distributions of the variations (R_{SD} and R_{max}) or the maximum value between different components, we would like to conclude that the directivity will dominate more obviously the fault perpendicular component than the other two components. This conclusion explains, also, why large variations are observed right on the fault trace for the y -component, but not for the other two components.

The modulus of the two horizontal velocity components is used in the process of seismic hazard assessment. The resulting distribution for that component is shown in Fig. 6.7 which illustrates where large variations of ground motions are expected when we change the hypocentre location. These variations (ratio between the standard deviation and the mean value) are distributed symmetrically around the fault edges with some amplification from the basin edges particularly on the south east fault trace end (inside region A). Large variation

(more than 40%) are just outside the basin. These regions are where the forward directivity effect dominates. Finally, we conclude the forward directivity effect has the largest part on controlling the seismic motions. The relatively higher ratio in the small basin around station R1 shows the medium effect.

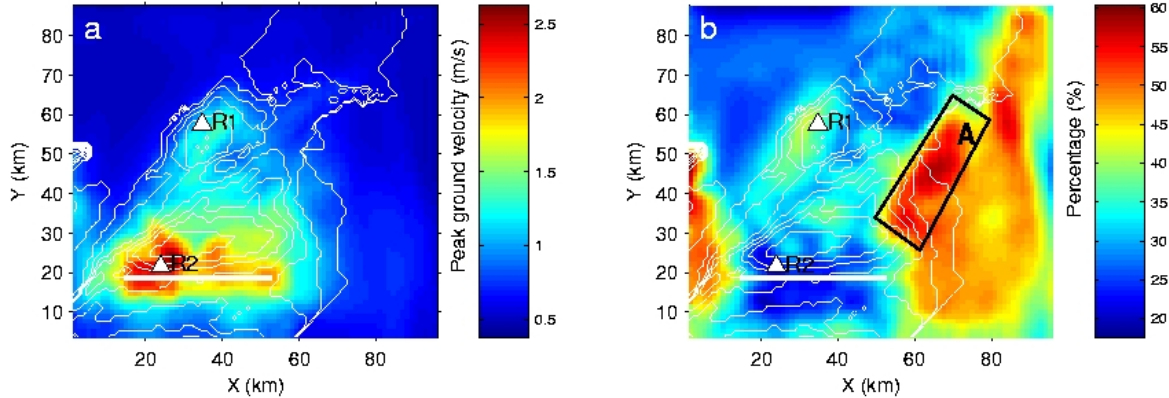


Figure 6.7: Statistics of the PGV distributions due to varying hypocentres: modulus component. **a.** Maximum of PGVs for the combination of all 24 simulations. **b.** The ratio between the standard deviation and the mean PGV value (combination of all 24 simulations, too) in percent. R1 and R2 are the two example positions chosen to show more detailed results. Region A is chosen to show the basin amplification on the variation.

We complete this study by investigating the relationship between PGV and source depth for all simulated scenarios, at two receivers R1 and R2 indicated in Fig. 6.8 (R1, 40 km from the fault, inside the basin; R2, close to the fault). Horizontal velocity seismograms (fault-parallel component) are shown for receivers R1, R2 and four different hypocentral depths (same epicentre) as indicated in Fig. 6.1 (enclosed with the white rectangle). The PGVs (and variance) for all 24 simulations at receivers R1, R2 are displayed as a function of source depth in Fig. 6.8c, 6.8d, respectively. For the distant receiver (R1, Fig. 6.8c) the mean PGV increases slightly with source depth, while the variance is much larger for deeper events, indicating a stronger path-dependence for wave fields arriving from deep sources than from shallow sources. The opposite behavior is observed for receiver R2 close to the fault (Fig. 6.8d) where the source will dominate the ground motion.

6.7 Comparison with the Empirical Results

Although the Newport Inglewood fault system is thought to be seismically active – an Mw 7.0 earthquake is believed to happen in the near future, there are no records from historical earthquakes. We compare our results against the empirical tools developed for the Los Angeles area in this section.

We compare the acceleration response spectra (PSA) at period of 4.0 sec, considering that the seismograms are low-pass filtered at period of 2.0 sec which is determined by the cut-off frequency of the finite difference method to avoid numerical dispersion. The low-pass filtering effect on the resulting acceleration seismograms are illustrated at first. Four stations are chosen and the Fourier amplitude spectra are shown in Fig. 6.9. Due to this filtering, the

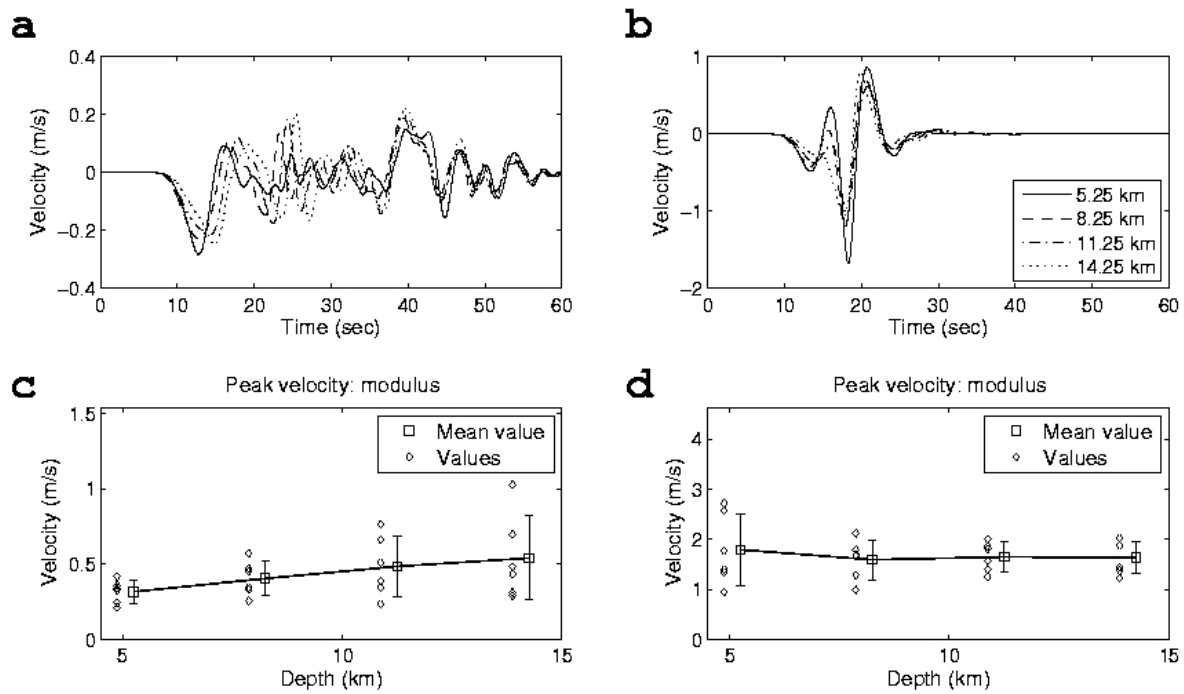


Figure 6.8: **a+b**: Velocity seismograms (fault-parallel component) for the M7 earthquake with same epicentre but varying source depth (see Fig. 6.1) at receivers indicated in Fig. 6.7a. **a**. R1, approx. 40 km off fault. **b**. R2, close to the fault trace. **c+d**: PGV as well as mean and variance for all simulations. **c**. R1; **d**. R2. Mean and individual values are offset for illustrative reasons.

acceleration amplitude spectrum at period 2.0 sec (0.5 Hz) is smaller than that at period of 4.0 sec (0.25 Hz) for almost all the stations and all the components. Considering the acceleration response spectrum at one frequency, f_0 , depends on the Fourier spectrum in the frequency range which includes f_0 (Hu et al., 1996), and the fact that the Fourier spectra are flat at the two sides around period 4.0 sec, it makes sense that we chose the period of 4.0 sec for the comparison.

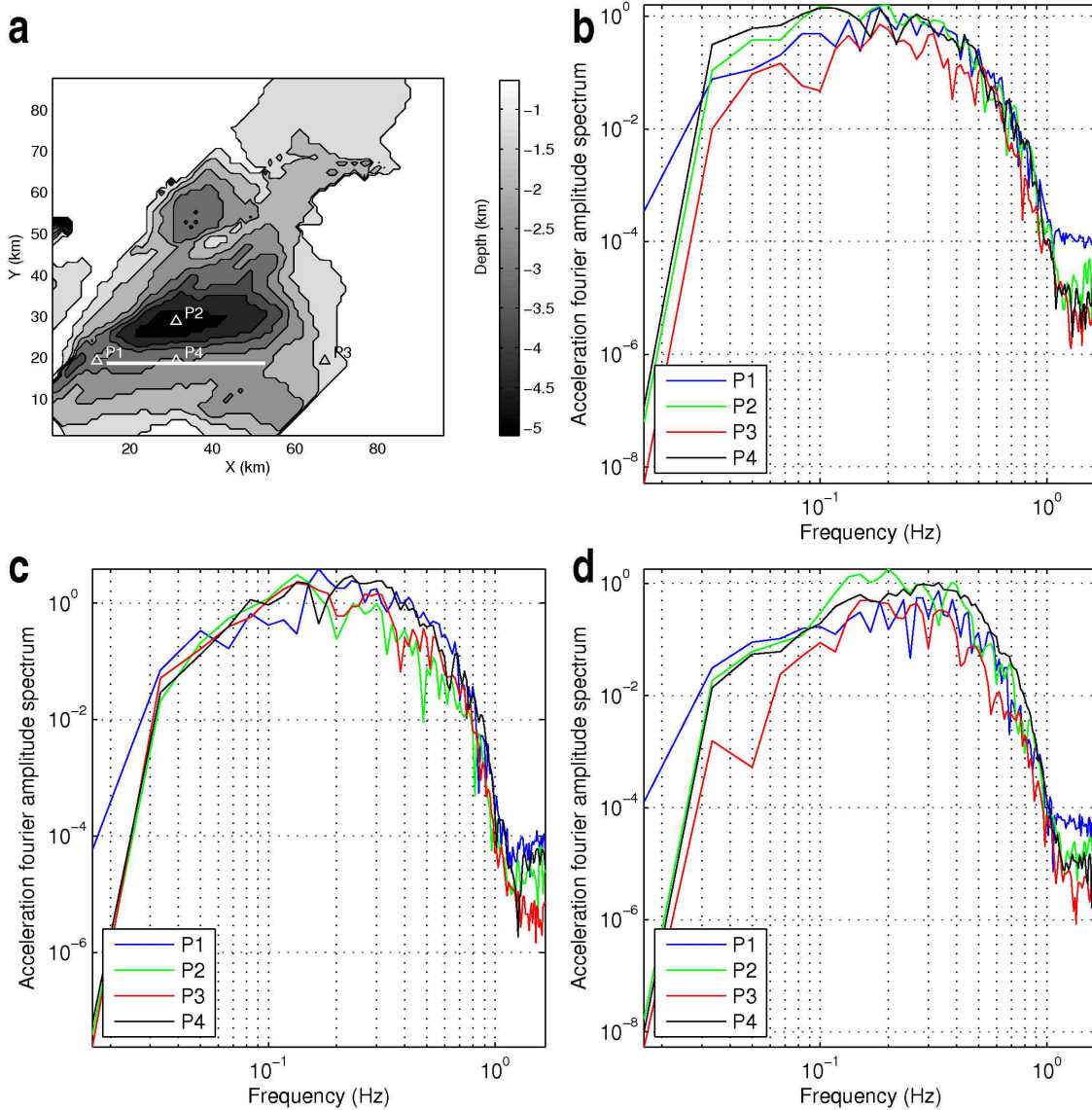


Figure 6.9: Acceleration amplitude spectra at four example stations. **a.** Basin depth (gray scale), fault trace (thick white line) and four example stations, P1, P2, P3 and P4 (hollow triangles). **b.** x -component. **c.** y -component. **d.** z -component.

The empirical attenuation relationship (ground motions against distance and magnitude) published in Campbell and Bozorgnia (2003) is popularly used for the southern California region. The appropriately simplified version for our case – hard rock site condition, pure

strike slip source mechanism, proper magnitude (M_7) and vertical fault plane is:

$$\ln Y = c_1 + c_2 \cdot M_w + c_3 \cdot (8.5 - M_w)^2 + c_4 \cdot \ln \left(\sqrt{f_2(M_w, r_{seis}, S)} \right) + c_{14} + \varepsilon, \quad (6.1)$$

where Y is the peak acceleration response spectrum and the distance scaling characteristics are given by

$$f_2(M_w, r_{seis}, S) = r_{seis}^2 + g(S)^2 \cdot (\exp [c_8 \cdot M_w + c_9 \cdot (8.5 - M_w)^2])^2, \quad (6.2)$$

in which the near-source effect of local site conditions is given by (in our case the firm rock)

$$g(S) = c_5 + c_7. \quad (6.3)$$

The standard deviation, $\sigma_{\ln Y}$ which stands for the data variation during the regression process, is defined as a function of magnitude

$$\varepsilon = \sigma_{\ln Y} = c_{16} - 0.07 \cdot M_w \quad \text{for} \quad M_w < 7.4. \quad (6.4)$$

All the parameters in equation 6.1 are shown in table 6.2.

The distance term, r_{seis} , is taken as the fault distance – the shortest distance between a station and the fault plane. The results are shown in Fig. 6.10 for different components. Each point in this figure represents a PSA value (the geometric average of two horizontal components, or the vertical component, respectively) at a station whose distance from the fault plane is represented by the x -axis. The empirical attenuation relationship of the PSA as a function of the fault distance is represented by the thick black line while the log-normal standard deviations, $\pm\varepsilon$, are shown with the two by-side dashed lines.

First, the mean value of our results fits well with that predicted with the empirical way at all distance ranges for the horizontal average component and the vertical component. Secondly, the PSA from our simulations stop to increase any more or begin to saturate within a very short distance (3 km) from the fault plane. Thirdly, for the horizontal average component, there are obviously high PSAs in the fault distance range of A. This fault distance range, referring to one of the subfigure in Fig 6.6, includes the small basin where basin amplification is observed in terms of the maximum ground velocity. The one predicted by the empirical relation, however, decreases smoothly in this range.

Table 6.2: Coefficients and Statistical Parameters for the PSA attenuation relationship

$T_n(sec)$	c_1	c_2	c_3	c_4	c_5	c_7	c_8	c_9	c_{14}	c_{16}
Average Horizontal Component										
2.0	-4.311	0.812	-0.180	0.019	-0.964	0	0.842	-0.187	-0.916	1.021
3.0	-4.817	0.812	-0.193	0.019	-0.964	0	0.842	-0.200	-0.873	1.021
4.0	-5.211	0.812	-0.202	0.019	-0.964	0	0.842	-0.209	-0.889	1.021
Vertical Component										
2.0	-5.292	0.756	-0.180	0.012	-0.812	0	0.931	-0.222	-0.503	1.031
3.0	-5.748	0.756	-0.193	0.012	-0.812	0	0.931	-0.238	-0.539	1.031
4.0	-6.042	0.756	-0.202	0.012	-0.812	0	0.931	-0.248	-0.606	1.031

Most large earthquakes are found to be unilaterally ruptured (rupture starts from one side of the fault plane), on which the empirical attenuation relationships are developed. However, in this study, the hypocentres are assumed to uniformly distribute on the seismogenic zone – a band zone through the fault plane in the strike direction. The rupture could start from the middle of the fault plane (in strike direction), thus bilateral rupture process is included. The co-existence of the unilateral and bilateral rupture process will lead to larger ground motion variation, at least in the near-source region where the source scenario dominates the generation of seismic motion.

The relative position between the basin and the broken region are fixed in our study. The accumulation of the basin effect on the ground acceleration, thus, produces the high value at the fault distance of 30-50 km for the horizontal average component. And since the basin is not far enough from the fault plane, the source effect will also play a big role on the ground motion which explains why there is no obvious basin effect observed for the vertical component in this study.

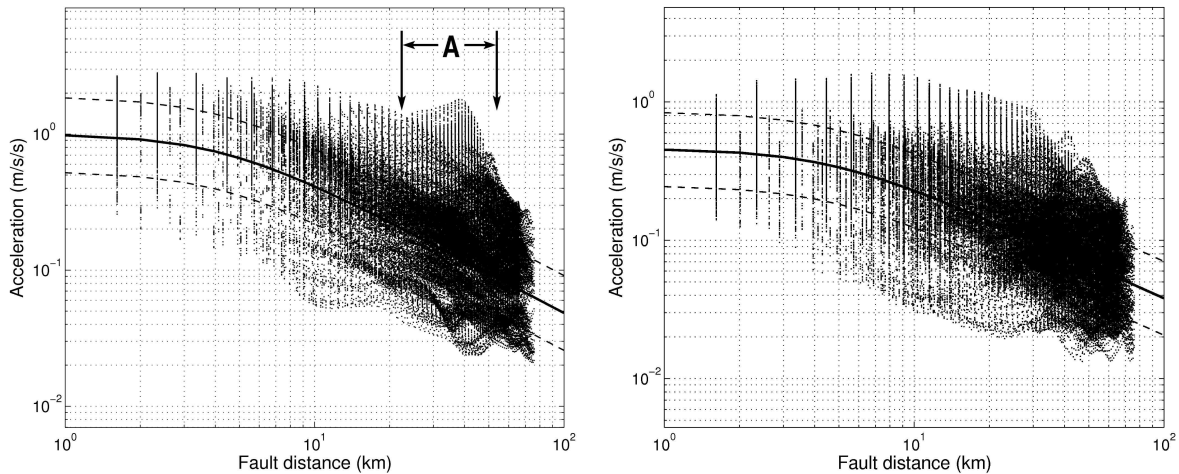


Figure 6.10: Comparison with empirical results in terms of acceleration response spectrum at period of 4.0 sec against fault distance. **Left.** Average of two horizontal components. **Right.** z-component. The result from the empirical relationship is represented by the thick black line together with the log-normal standard deviation (dashed black lines). Black dots are acceleration response spectrum (PSA) values from our simulation. Distance range A is picked up for more detailed discussion.

6.8 Conclusions

We introduced the concept of numerical Green's functions (NGF) that can be applied to discretized faults or fault systems in 3D media allowing the calculation of earthquake scenarios from arbitrary slip histories. NGF data bases allow a systematic study of source related uncertainties/variations of seismic hazard relevant wave field properties (peak ground motions, static displacements and rotations, shaking duration, etc.) varying slip distributions (e.g., asperity locations), slip and rupture velocities, hypocentre locations, etc.. Particularly interesting is the possibility to apply high-resolution slip histories from dynamic rupture simulations and investigate their relevance to shaking hazard.

In this chapter we design a hypocentre grid located inside the seismogenic zone of the Newport-Inglewood fault and investigate how the variation of hypocentre location will affect the ground motion within a 3D medium. The resulting ground motions enable us to provide the possible ground motion range (maximum plus variation) inside our study area during the possible future M7 earthquakes.

First, the pure-strike slip source mechanism restricts the ground motion to the horizontal movement. The movement of one point in the vertical direction is three times smaller than in the horizontal directions. Secondly, for the fault perpendicular component and the vertical component, large variations (largest value around 70% with respect to the variance relative to the mean value) are introduced by the varying hypocentre at the regions with smaller angles to the fault trace. The directivity dominates the generation of ground motion inside those regions. Considering that one of these regions is already outside the basin and thus less structure effects will be observed, the single change of the hypocentre location is capable to introduce large variations to the ground motions. The large variations of peak ground velocity at regions off the two tips of the fault trace are also observed in Gallovič and Brokešová (2007b) for a homogeneous model whose frequency range is much higher than ours. Thirdly, for the fault parallel component, at the edge of the basin where the medium parameters change rapidly and the directivity controlling vanishes, there are still large variations observed. Under-surface structure is important to explain the variations of that component of ground motion.

The results are also compared with one popularly used empirical tool – the peak acceleration response spectrum (PSA) attenuating with the fault distance. At the period of 4 sec, our results match with that method with an extra emphasis on the basin effect.

Varying hypocentre location is one way to put more complexity into the source scenarios, the other interesting topic is to fix the hypocentre location but vary the final slip distribution and investigate how the ground motion varies. We will work on that subject in the next chapter.

Chapter 7

Application: Slip History Effect

¹ **ABSTRACT:** Finite-fault source inversions reveal the spatial complexity of earthquake slip over the fault plane. In this study, several possible earthquake scenarios of Mw 7.0 are simulated with different quasi-dynamic finite source models for the Newport Inglewood (NI) fault system in the Los Angeles (LA) basin embedded in the 3D SCEC community velocity model version 3. We make use of the recently developed Numerical Green's Functions method and synthesize ground motions from a data base of 3D Green's functions, calculated for a discretized model of the NI fault. This allows efficient simulation of arbitrary slip histories. We investigate the effects of the various slip histories on peak ground velocities and the related uncertainties in ground motion prediction for our study area. The results confirm that the fault perpendicular components of motion are dominated by directivity effects while the fault parallel component is influenced both by the slip distribution and the basin structure.

7.1 Introduction

A major goal of hazard related seismology is to be capable of providing strong ground motions that can be used in engineering analysis (Aki and Richards, 2002). However, this goal is hard to achieve because there are not sufficient observations of ground motions in zones at risk of large earthquakes to satisfy the demands of modern earthquake engineering practice, especially for the region close to major active faults. With the development of modern computer technology, the numerical method for calculation of the full wave-field will complement these demands and play a more and more central role in reliably estimating shaking hazard (e.g., Olsen and Archuleta, 1996; Olsen, 2000; Ewald et al., 2006). The main influences on ground motions can be split into two phenomena: (1) 3D wave propagation effects from the fault to the station through the crust; (2) intrinsic source effects resulting from the diversity of fault slip histories. While the first effect can be continuously improved by incorporating new results from tomographic tools and/or direct measurements (e.g., borehole information), the uncertainty concerning source behavior remains and it is unquestionable that hazard relevant ground motion characteristics for earthquakes of a given size will strongly depend on rupture properties such as directivity, static slip, rupture speed, and rise time. Thus it appears useful to estimate ground motions due to many "characteristic earthquakes" of a specific seismically active region

¹Wang, H. J., H. Igel, A. Cochard and M. Ewald, Third International Symposium on the Effects of Surface Geology on Seismic Motion Grenoble, France, 30 August - 1 September 2006.

with different slip scenarios, in order to account for rupture related ground motion variations. This goal is achieved in this section.

The directivity effect has recently been given more attention by seismic engineers in the near-source region seismic motion prediction since it has a first order effect on ground motion (Anderson, 2003). It was first suggested to explain the accelerograms of the 1966 Parkfield earthquake (e.g., Aki, 1967; Haskell, 1969). Kinematic finite source simulations in a homogeneous medium were carried out to investigate source related effects (e.g., Archuleta and Hartzell, 1981; Anderson and Luco, 1983a,b). In the region towards which the rupture propagates, the fault perpendicular component was found to have the strongest absolute amplitude. Somerville et al. (1997) develop empirical ground motion prediction relations based on several strong motion observations.

At the same time, some source parameters (static slip, rupture velocity, rise time, slip velocity) are found not to be uniform on the fault plane. Images of the spatial and temporal evolution of earthquake slip on fault planes provide compelling evidence that fault displacement is spatially variable at all resolvable scales, as also inferred from inversions of geodetic data (e.g., Larsen et al., 1992; Bennett et al., 1995). Investigations of strong ground motion also indicate the spatial variability of the rupture velocity (e.g., Archuleta, 1984; Beroza and Spudich, 1988; Bouchon et al., 2000). Herrero and Bernard (1994) proposed a model in which the rise time depends on the wave number of a spatially variable slip distribution. This source physics complexity appeals for thorough description of the source process when calculating seismic motion.

Those two contributions to ground motion variations are investigated in this paper. The pre-created Numerical Green's Function database is used to synthesize different slip histories in order to provide a possible ground motion range for one hypothetical earthquake of Mw7.0. Using the pseudo-dynamic approach of (Gattereri et al., 2004) for generating realistic rupture scenarios, 20 different slip histories are created and ground motions at the surface of the study area are synthesized. We characterize the resulting seismic shaking with maximum and mean values, as well as standard deviation of all the 20 resulting peak ground velocity (PGV) distributions. This allows a quantitative discussion of 3D structural vs. source related effects.

7.2 Slip Histories

Huge variation of strong ground motion observed in the near-source can be described and explained with several phenomena like directivity, near-source impulse, and static offsets, which are strongly affected by the geometrical and dynamic characteristics of the faulting. In order to understand those phenomena and the associated uncertainties, how the ground motion varies with many different slip histories is worthy of an investigation. In the following sections we first describe the set up of the synthetic experiment, describe the source processes and analyze the resulting ground motions.

In this study, we synthesize 20 different "characteristic earthquakes" with magnitude Mw 7.0 with the forward NGF method to investigate source related variations. The fault length L and area A are calculated using the relationship by Wells and Coppersmith (1994), $\log L = -2.57 + 0.62 Mw$ and $\log A = -3.42 + 0.9 Mw$, and the scalar moment M_0 is related to magnitude through the empirical relation introduced by Kanamori (1977). The final average slip D is linked to the scalar moment, M_0 , shear modulus μ , and fault area A by $M_0 = \mu DA$. Since no surface faulting was observed in the 1933 M_w 6.4 Long beach earthquake, the M_w

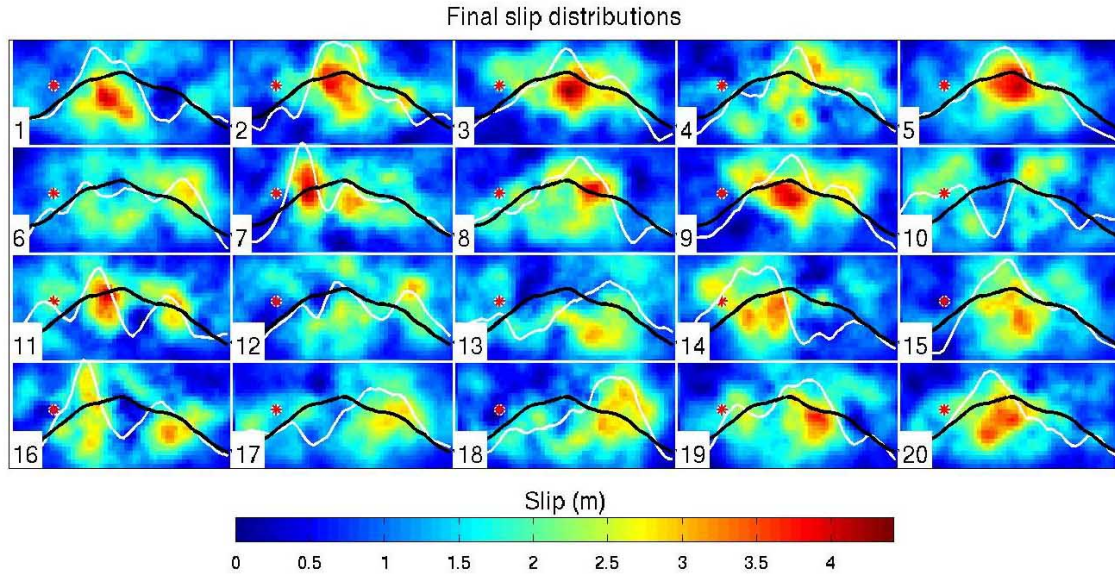


Figure 7.1: Numbered slip histories used in the simulations. Red asterisks mark the hypocentres. White and black lines show the comparison of single cumulative slip to the mean cumulative slip (of all slip histories), respectively. Slip histories are derived following [Guatteri et al. \(2004\)](#). Fault dimensions are 39×18 km, in strike and dip direction.

7.0 earthquake is also assumed to be buried inside the crust and the top edge of the fault is set at 1.8 km in depth.

The method published in [Guatteri et al. \(2004\)](#) is adopted to generate the quasi-dynamic rupture processes including the accelerating trends of the crack front due to the dynamic loading from the rupture area. The phenomenon that local high stress drop promotes fast rupture propagation is also accounted for. In this method, the final slip distribution is generated randomly with a given isotropic autocorrelation length (5 km). Rupture velocity and rise times are calculated as a function of the final slip distribution and the hypocentre location. The hypocentre remains fixed in order to focus on the ground motion variations due to slip histories. The shear velocity relevant for the slip histories is kept constant at 3.2 km/s and the rupture velocity is restricted to the range $[0.6, 0.8]$ times shear velocity. The 20 final slip distributions calculated with this method are shown in Fig. 7.1.

7.3 Average PGV Characteristics

First, the effect on different components of ground motion is illustrated in Fig. 7.2 with mean values of all 20 PGV distributions on the surface for three components. The area, with mean PGV of y -component larger than 0.8 m/s (black rectangular, Fig. 7.2, middle), is the area towards which the rupture propagates and where directivity plays the most obvious role. We name that area A. The maximum value of mean PGV in this area A for the y -component (fault perpendicular) is around 1.7 m/s, and almost twice larger than that for the x -component (fault parallel) and almost three times larger than that for the vertical component (note the different color scale). At the same time elevated mean PGV is observed inside the basin but

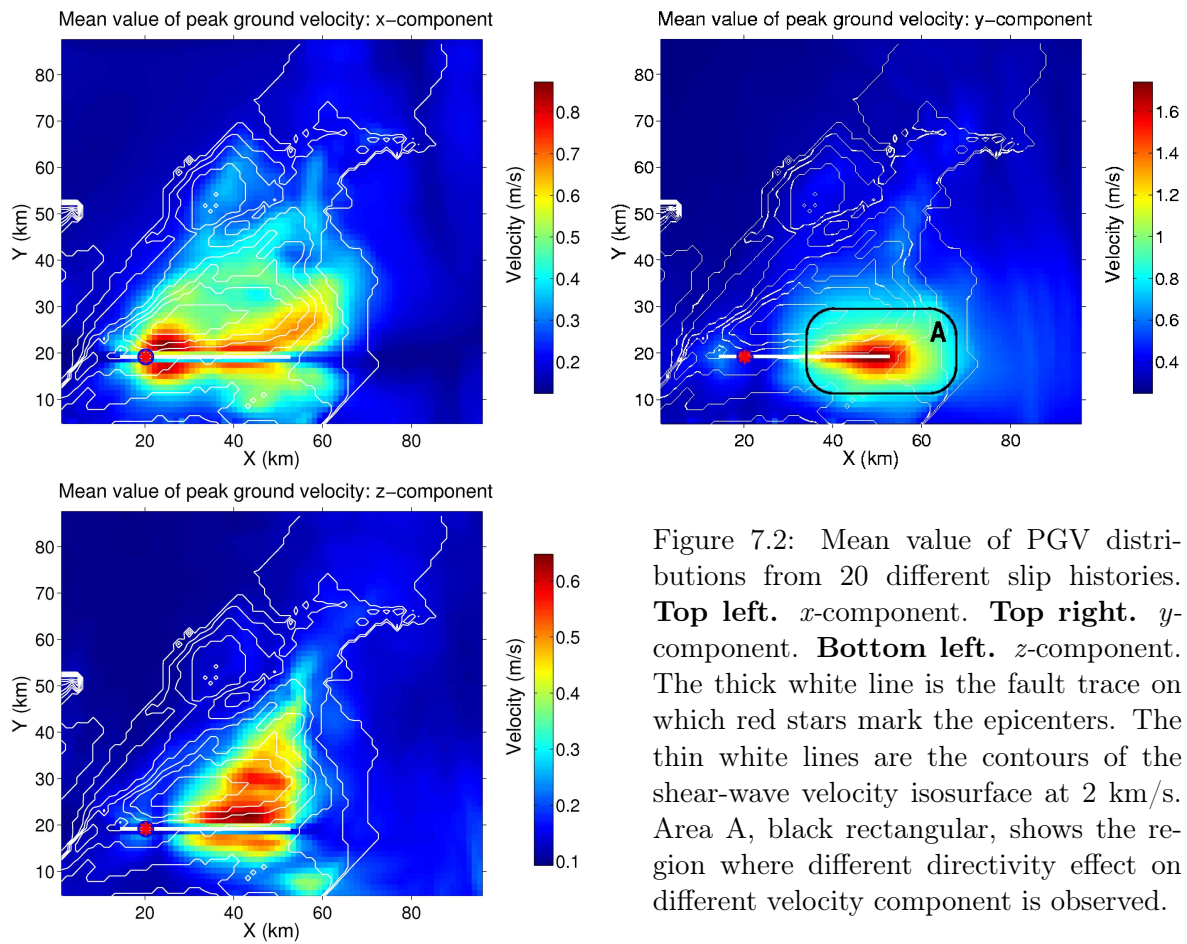


Figure 7.2: Mean value of PGV distributions from 20 different slip histories. **Top left.** x -component. **Top right.** y -component. **Bottom left.** z -component. The thick white line is the fault trace on which red stars mark the epicenters. The thin white lines are the contours of the shear-wave velocity isosurface at 2 km/s. Area A, black rectangular, shows the region where different directivity effect on different velocity component is observed.

outside area A both in the x -component and the vertical component indicating the influence of basin structure and the slip variation. Thus it can be concluded that the fault perpendicular component is dominated by the directivity effect and the fault parallel and vertical components have significant contribution from the 3D structure (basin effects) and slip distribution.

7.4 Source Dependent PGV Variations

To study the effects of various slip histories in more detail, we take four different slip histories as example and show the resulting PGV distributions (Fig. 7.3)². These four slip histories are considered to be representative and their slip distributions are shown in the top of Fig. 7.3. Slip 5 has a distinct asperity area right in the middle of the fault. Slip 7 has a smaller asperity area with very large slip close to the hypocentre. Slip 10 has a more uniformly distributed slip. Slip 16 has two asperity areas and the major part is located in the bottom half part of the fault. For slip 16, seismic motions have smaller amplitudes compared to the other three slip models because the most part of slip occurs in the bottom half part and further from the surface. Slip 5 gives a large PGV in the region close to its high slip asperity, especially in the x -component, indicating that large seismic motion is expected in the area close to asperities. This effect can also be seen in the results of slip 10 – there is a low PGV band between two high PGV areas along the fault plane that coincide with low cumulative slip as indicated in Fig. 7.1. This may also be responsible for the sharp increase in PGV (y -component) beyond the area of low cumulative slip. Comparison of different components of PGV between the area inside the basin but far from the fault, and the area, A, close to the fault, suggests that the directivity plays a more important role on the component perpendicular to the fault plane.

Considering the complex PGV distribution on the surface due to different slip histories, it is instructive to present the possible range, namely maximum and variation of shaking deduced from the 20 earthquakes for the Newport Inglewood fault. Two ratios are calculated and shown to characterize the variations: R_{SD} – the one of the standard deviation relative to the mean value, and R_{max} – the one between the maximum value and the mean value. We show those ground motion characteristics in Fig. 7.4. To give a further illustration of the directivity effect, those shaking variations related to the two horizontal velocity components, x and y , are also shown.

At the far end (far from the epicentre) of the fault trace (region A, Fig. 7.4 top middle), the maximum value of y -component is around 2.5 m/s while it is less than 1.5 m/s for the x -component. In region A, large differences in terms of standard deviation are also found between these two horizontal components. For the y -component, around this fault trace tip, the maximum PGV and the standard deviation are obviously larger than its neighboring region and the epicentre neighboring regions. Whereas those variables are quite smooth in this region for the x -component and smaller than in the epicentre neighboring regions. The directivity effect plays a much larger role in the y -component than in the x -component. At this far end of the fault trace, no large variation (R_{SD} and R_{max}) is found for both the two horizontal components.

The largest standard deviation and velocity value of the x -component are located near the epicenter (Fig. 7.4, top and second line, left). Large values of R_{SD} and R_{max} exist, however, a little further from the epicentre and the fault projection, in the region C where the medium parameters change rapidly (Fig. 7.4, third and bottom line, left), instead of the region where

²All the PGV distributions corresponding to these 20 slip histories are shown in Appendix B.

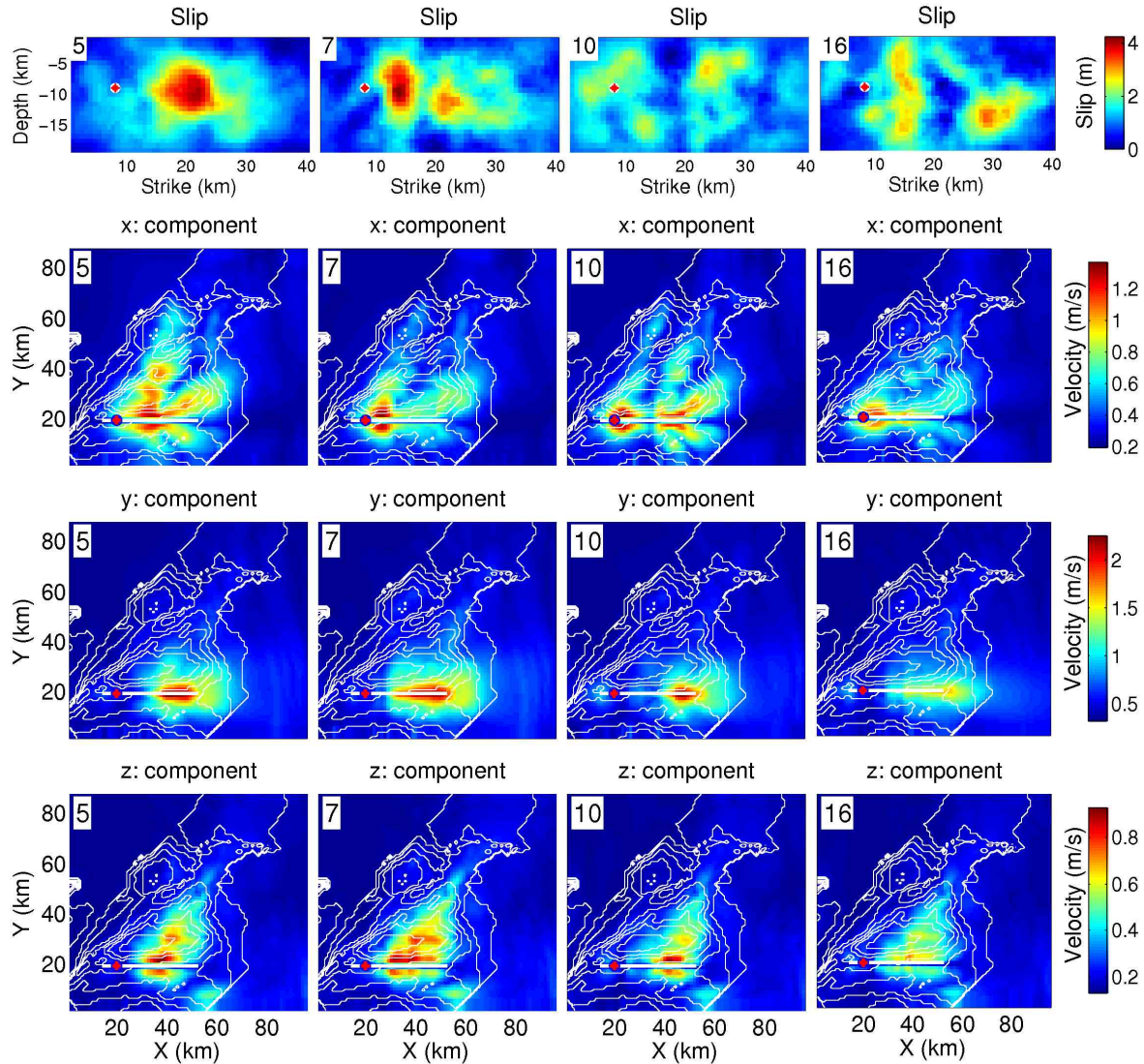


Figure 7.3: Peak ground velocity distributions for slip 5, 7, 10 and 16 for all three components. The corresponding slip distributions are shown at the top. The thick white line is the fault trace on which red stars mark the epicenters. The thin white lines are the contours of the shear-wave velocity isosurface at 2 km/s. Note the different color scale.

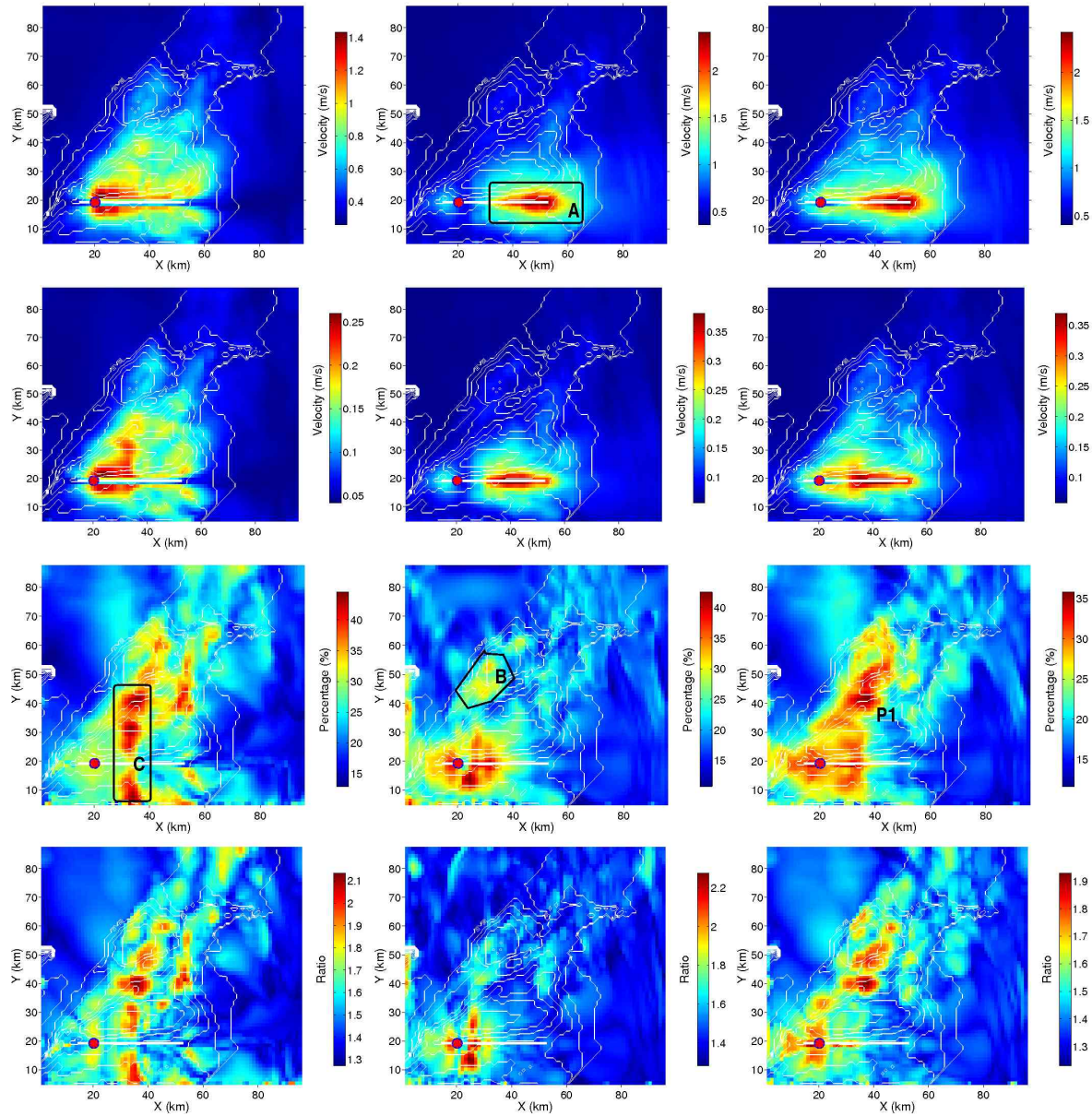


Figure 7.4: PGV – maximum, standard deviation and the variation (measured by two ratios: the one between the standard deviation and the mean value; and the one between the maximum value and the mean value) for two horizontal and modulus components. **Top.** Maximum value. **Second line.** Standard deviation. **Third line.** Ratio between the standard deviation and the mean value. **Bottom.** Ratio between the maximum value and the mean value of the individual PGVs. **Left.** x -component. **Middle.** y -component. **Right.** Modulus component (length of velocity vector). The thick white line is the fault trace on which red stars mark the epicenters. The thin white lines are the contours of the shear-wave velocity isosurface at 2 km/s. P1 is the station with the highest ratio. Regions A and B are picked up for detailed discussion.

source scenarios change rapidly (around the fault trace). The largest ratio is found right at the basin edge. The basin structure obviously introduces more variations to the seismic motion than the slip history complexity.

For the y -component (fault perpendicular) (Fig. 7.4, middle column) the PGV distribution is completely different from that of the x -component (fault parallel). Both R_{SD} and R_{max} are different to those of the fault parallel component in terms of spatial distribution. The large ratios are mainly restricted in the region surrounding the epicentre (largest: 43% and 2.2). From all the forward observations we conclude the y -component (fault perpendicular) strongly depends on the source in the near-field region. For the y -component, the medium effect is also obvious when we get a little further from the source region, e.g., in the region B.

The spatial distributions of ration R_{max} are quite similar to those of the ratio R_{SD} for different components. The largest values are observed at the same locations. The contributions from the source and the medium complexity are similar with respect to different velocity component. The slight difference is the spatial distribution of ratio R_{max} is coarser than that of the ratio R_{SD} . At the small basin edge, region B, a much sharper change is observed in the modulus component in terms of ratio R_{max} (Fig. 7.4 bottom line, right) than ratio R_{SD} (Fig. 7.4 third line, right). Medium amplification is more obvious for this ratio.

The maximum PGV distribution of the modulus component, i.e. the length of the velocity vector (Fig. 7.4, top right) looks similar to the fault perpendicular component (Fig. 7.4, top middle): the largest values are both around 2.5 m/s (larger than the x -component: 1.4 m/s), and the spatial distribution patterns are similar. The ratio between the standard deviation and the mean value seems to be the combination of the two horizontal components – to be large both in the regions surrounding the epicentre and close to the basin edge. The largest ratio (between the SD and the mean value) for the entire area is 40%, at point P1 (Fig. 7.4, bottom right) which is at the basin edge like the x -component. The maximum seismic motions on the surface are dominated by directivity. But the variations receive more contributions from the source effect which depends on how far from the fault trace. Around the epicentre, the variations are dominated by the source complexity. Close to the basin edge, the variations are dominated by the medium.

The ratios between the maximum value and the mean value (Fig. 7.4 bottom) are quite similar to the ratios between the SD and the mean value (Fig. 7.4 third line) with respect to the spatial distribution. The slight difference is observed between the regions outside and inside the basin. The basin effect is not as distinct as observed in the ratio between the SD and the mean value (Fig. 7.4 third line).

7.5 Discussions and Conclusions

In this study we investigated the source dependent contribution to the strong ground motion in 3D medium with specific application to a characteristic M7.0 earthquake on the NI fault in the Los Angeles basin. The fault perpendicular component (y) exhibits at least twice larger peak velocity amplitudes than the fault parallel components (x , z) in the area around the right part of the fault, that is, in the direction towards which the rupture is propagating. This phenomenon is also observed in the strong ground motion measurement and is a crucial aspect in earthquake hazard and risk analysis.

Seismic shaking variations due to various rupture processes are also investigated in this study. The static slip (input parameter for kinematic finite source simulations) is impor-

tant when calculating seismic motions because the area with large static slip (asperity area) will introduce elevated seismic motions. In combination with directivity, it can increase the complexity of surface seismic shaking.

Comparing the modulus component of PGV with those of the two horizontal components for an M7 strike-slip earthquake, we conclude that the modulus component is dominated by the fault perpendicular component in terms of absolute value while equally by the two horizontal components in terms of relative variation. The different effect due to directivity and slip history, respectively, should be considered when doing ground motion prediction, at least in our specific case, that is, NI fault and LA basin.

The results shown here indicate that to reliably estimate shaking hazard for specific earthquake scenarios, the source dependent effects should be taken into account. This necessitates calculation of many different slip histories to fully account for the associated uncertainties. In the (long-) period range considered in this paper there is a remarkable difference between the finite-source effects on the various motion components, mixed with effects of the 3D structure. More simulations will be necessary in the future to quantitatively estimate the contributions of small scale structures and source effects at higher frequencies.

Rotational motion is also recorded during the numerical Green's function generation process which enable us to investigate the how the ground rotation varies according the variation of different parameters as discussed for the translational part of motion in the forward two chapters. The results are shown, analyzed and compared with the translational motion in the next chapters.

Chapter 8

Application: Rotation Rate

ABSTRACT: Recently, the instrument technology (e.g., ring laser) is capable to accurately record the rotational motion observation. However, due to the scarcity of the data, the systematic rotation variation in 3D media is still a challenge. In order to answer that question, we simulate several M7 earthquakes with different source scenarios on the Newport-Inglewood (NI) fault embedded in the 3D Los Angeles Basin and. The recently calculated data base with several hundred numerical Green's functions for a discretized model of the NI fault allows arbitrary finite-fault scenarios to be synthesized by superposition. We investigate source and basin structure effects on the rotational components of ground motion (e.g., peak ground rotation rates and their variation or horizontal gradients) and compare with the translations. Only the rotations from the seismic source with assumption of linear elasticity are considered.

8.1 Introduction

In conventional earthquake engineering, seismic loads on structures are formulated only in terms of the three translational ground motion components. Nevertheless, each site on the surface can be subjected to six kinds of motion: three translations along x -, y - and z -axes as well as three rotations about these axes. While the building response shaken by translational motions has been long investigated, building response of the rotational motions is just at the beginning.

The engineering importance of rotational components of seismic strong ground motion was noted during late sixties and early seventies of the last century (e.g., [Newmark and Hall, 1969](#); [Newmark and Rosenblueth, 1971](#)). There are many reports about rotations of tombstones and stone lanterns during large earthquakes (e.g., [Yamaguchi and Odaka, 1974](#)). [Zembaty \(2006\)](#) also pointed out that the rotation effects become especially important in the case of high buildings. Difference models have also been studied and used to evaluate the effects of torsional excitation (e.g., [Gupta and Trifunac, 1987, 1989, 1990](#)) and of rocking excitation (e.g., [Gupta and Trifunac, 1988, 1991](#)). These studies have shown that torsional and rocking excitations can be significant and with combinations of structural and soil properties are important for such excitation. For example, rocking excitation becomes important for tall structures supported by soft soil while torsional excitations can dominate in the response of long and stiff structures supported by soft soils ([Zembaty and Boffi, 1994](#)). These buildings are very sensitive to angular momentum carried by rotation waves. Moreover, incident rotational waves interact with the geological structure (e.g., granular medium) and may lead to their softening, degradation,

damage or fracture. Geological media with rotational degrees of freedom (e.g., the so-called “liquid sands”) are extremely sensitive to any rotational motions or vibrations.

A question whether the rotation motions at seismic source can propagate in a form of wave through geological layers from the seismic source to a distant recording station seems still open. Recent theoretical studies (e.g., [Teisseyre, 2004](#); [Boratyński and Teisseyre, 2004](#)) and observational results bring a positive answer to this question. An interesting contribution in this field was a simulation study of rotational effects in layered media and near-field excitations by [Bouchon and Aki \(1982\)](#). They simulated rotational ground motions near earthquake faults buried in layered media for strike-slip and dip-slip fault models, and obtained a maximum rotational velocity of 1.5×10^{-3} rad/s produced by a buried 30 km (seismic moment of 8×10^{18} Nm) long strike-slip fault with slip of 1 m.

Such small rotational motions are difficult to be measured. Deployment of strong motion accelerographs in many seismic areas of the world during the past seventy years has produced data on translational components of motion during many strong earthquakes. This data describes strong motion in three orthogonal directions (two horizontal and one vertical), but because the spacing of the recording sites is much larger than the wavelengths of the recorded motions, little is known today about the accompanying differential and rotational motions.

The ground rotational motions were observed by [Nigbor \(1994\)](#), [Spudich et al. \(1995\)](#), [Stedman et al. \(1995\)](#), [McLeod et al. \(1998\)](#), [Spillman et al. \(1998\)](#), [Takeo \(1998\)](#), and [Igel et al. \(2005\)](#). The measurements carried out by [Takeo \(1998\)](#) were recorded in the near-source region of earthquakes. The measurements by [Spillman et al. \(1998\)](#) were carried out far from an earthquake source (200 km and more).

Many questions related to the rotational motions remain open: up to now, we have no reliable data on propagation properties (velocity and attenuation) of such energy through geological media and on the influence of distance from source to the recording station. Translational and rotational components of strong motion radiated from an earthquake source are modified along the propagation path through interference, focusing, scattering, and diffraction. For the velocities, complex variations are observed in [chapter 6](#) and [chapter 7](#) with respect to the varying hypocentre location and varying slip history. In this chapter, how the ground rotation rates vary with these source and sub-surface parameters are investigated. The results are shown and analyzed.

In recent decades ring laser technology succeeded in detecting small variations of the earth’s rotation rate introduced by earthquakes. At teleseismic distances the seismic wave field can be well approximated with plane waves. Under this assumption, a direct comparison between rotation rate around a vertical axis and transverse acceleration (recorded by a standard seismograph) is possible – translations and rotations are in phase and their amplitudes scaled by twice the horizontal phase velocity. [Igel et al. \(2005\)](#) study similarity between the collocated translations and rotations by taking the advantage of the new developed instrument – ring laser. Their observations showed over a very broad frequency range (1–150 sec) that the waveforms have the expected similarity and the amplitude ratios allow an accurate estimate of horizontal phase velocities ([Igel et al., 2005](#); [Cochard et al., 2006](#)). In the near source region, the fundamental assumption of the above mentioned study – the plane wave propagation – could not hold any more. But what the comparison between the translation and the rotation will reveal is still considered an interesting topic. This is the one of the targets of this chapter, too.

To sum up, we will try to solve the following central questions in this chapter:

1. What are the peak ground rotation rates to be expected for M7 earthquakes?
2. How does the structure affect the spatial distributions?
3. What are the source-dependent variations?
4. How do these variations (spatial distribution) compare with those of the accelerations?
5. What can we learn from the joint processing of rotation and acceleration?

8.2 Verification

First, as what has been done for the velocity part of ground motion, we check if the sub-fault with side-length of 1.5 km (optimal sub-fault size) works well. The computational setup and source parameters are given in Table 5.1. The fault length L and width W are specifically chosen to be 36 km and 18 km with the aim to get uniform sub-fault discretizations with size of 3×3 , 4×4 , 5×5 , and 6×6 , respectively (in grid points, considering the total number of grid points that the fault plane occupies being 120×60). The quasi-dynamic rupture process adopted is calculated with the method published in Guatteri et al. (2004), with 2D Gaussian auto-correlation function used and an isotropic correlation-length of 5 km adopted. The final slip distribution is shown in Fig. 6.1. An M7 finite fault earthquake scenario is first simulated with a sub-fault of side-length 0.3 km (treated as the “continuous” solution, corresponding to the finest grid distance). The ground rotation rates for the two larger solutions are compared to those for the “continuous” solution, respectively.

The z -component of rotation rate has much larger absolute amplitude than the other two components because of the pure-strike slip source mechanism, and thus is used to illustrate the results (see Fig. 8.2). The peak ground rotation rates (PGRRs) covering frequencies up to 0.5 Hz from different solutions are compared over the entire study area. The ratio – the PGRR difference between one discretized solution (sub-fault size of 1.8 km) and the “continuous” solution, divided by the PGRR of the “continuous” solution – is shown in Fig. 8.1a. The largest relative difference is 18% in the position of P1. The waveforms from different solutions are almost identical in the profile shown in Fig. 8.1c with lowest peak correlation coefficient value of 0.991. This can also be seen from the waveform comparison (Fig. 8.1b) for one single station where the biggest relative PGRR difference is observed (point P1, Fig. 8.1a). The maximum amplitude difference between the solution for 1.5 km sub-fault side-length and the “continuous” one is 4.1×10^{-5} rad/s while that for the solution for 1.8 km is 7.2×10^{-4} rad/s. Thus we conclude that solution of 1.5 km sub-fault side-length is also accurate enough for the rotation rate part.

8.3 Effect due to Hypocentre Location

How the variations of the hypocentre location, for a given final slip distribution, influence the ground rotation rate, during a characteristic earthquake of a given magnitude, is investigated in this section. We assume the existence of a characteristic M7 earthquake on the entire NI fault. A 4×6 grid of hypocentres in the seismogenic zone (5 - 15 km depth) as indicated in Fig. 6.1 is designed. These hypocentres are implemented into the synthesization and the resulting ground motions are presented in this section.

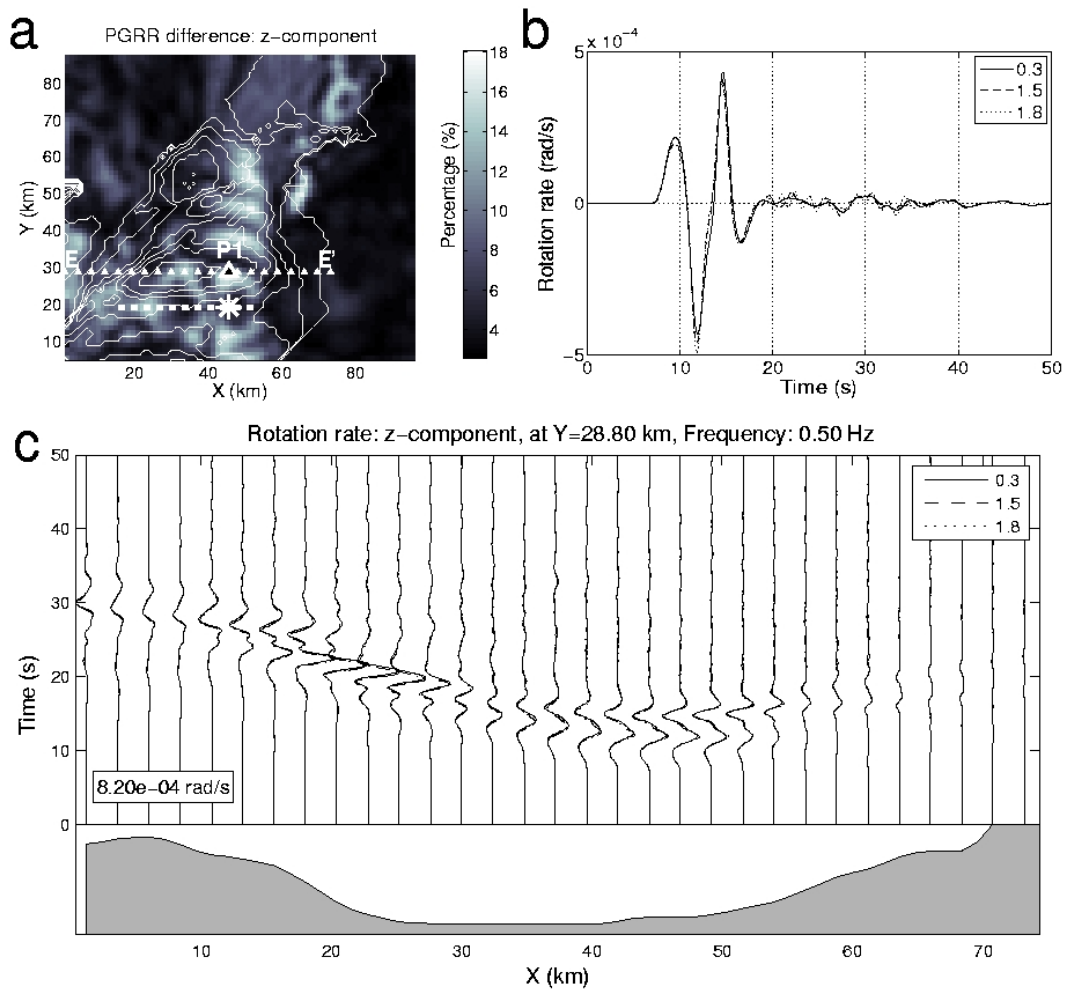


Figure 8.1: Effect of sub-fault size on rotation rate. **a.** Relative PGRR difference (z -component) between the solution of 1.8 km and the “continuous” solution. The dashed thick white line marks the fault trace. **b.** Rotation rate seismograms from different solutions (0.3 km, 1.5 km and 1.8 km) at receiver P1 (largest misfit). **c.** Rotation rate profile along EE’ (**a**) in which the depth of shear wave velocity isosurface at 2.0 km/s is shown at the bottom (gray scale). The largest rotation rate amplitude across this profile is shown with the inlet number.

8.3.1 Two Examples

Two hypocentres, H1 and H2 (Fig. 6.1)¹, are chosen as examples and the properties of the corresponding ground rotation rates are illustrated, analyzed and compared to the ground velocity and acceleration in this section.

First we show how the peak ground rotation rates (PGRRs) vary on the working area for different components in Fig. 8.2. All over the working area, the PGRRs of the z -component (Fig. 8.2 bottom) are 10 times larger than those of the x -component (Fig. 8.2 top) and almost 5 times larger than those of the y -component (Fig. 8.2 middle). However, for the case of velocity (Fig. 6.3), the peak ground velocity of the z -component is only a half of the two horizontal components. This is explained by the source mechanism adopted – pure strike slip and vertical fault plane. That specific source mechanism will produce large velocity difference in the x -component across the fault trace in the y direction. Thus big vertical rotation rate, which is proportional to the space derivative of the two horizontal velocity components, is produced.

For the x -component, for the hypocentre H2 – the epicentre is located in the center of the fault trace – there are two obvious regions around the fault trace tips where the rotation rates are much larger than the surrounding regions (Fig. 8.2 top right). The rotation rates inside these two regions are not much less different than the other two components. These regions with obviously uplifted amplitudes do not exist for the other two components any more. Just as theoretically predicted in chapter 5, the directivity effect dominates this component of rotation rate. For the hypocentre H1, the rotation rates at stations around the left fault trace tip is much larger than those around the right fault trace tip. This finding could also be explained with the forward directivity effect.

For hypocentre H2, the y - and z -component of rotation rate have larger amplitudes in the region close to the left tip of the fault trace than the right one. Considering the epicentre location, this observation leads to a conclusion about the medium amplification.

Two profiles are chosen and the rotation rate seismograms on them are shown in the following two figures. The one in Fig. 8.3 is parallel to the x -axis, located at $y = 28.80$ km and across the fast basin-depth-change area ($x \in [7, 30]$ km). The other one in Fig. 8.4 is parallel to the y -axis, located at $x = 33.60$ km, across the fault trace and the small basin in the range of $y \in [47, 64]$ km. In Fig. 8.3, for both hypocentres and for all three components, the amplitudes get larger when x increases to 10 km where the basin depth gets larger. The same increasing of amplitude is also observed in Fig. 8.4 when y decreases to 62 km where the basin becomes deeper. In Fig. 8.4, in the range $y > 64$ km, due to the basin blocking, almost no energy is observed, compared to the other stations on this profile, even for the case of hypocentre H2 – a bilateral rupture process. At the two sides of the fault trace, for the first arrival, there are phase change for the y -component and the z -component, but not for the x -component (Fig. 8.4).

8.3.2 Inter-event Variations of Rotation Rate

Two statistic parameters – the maximum value and the variations all 24 simulations are shown for all the three components in Fig. 8.5 to give a general image of the ground motion variations which contains the dominant features shown by the two previous examples, like

¹All the PGRR distributions corresponding to these 24 hypocentres are shown in Appendix A.

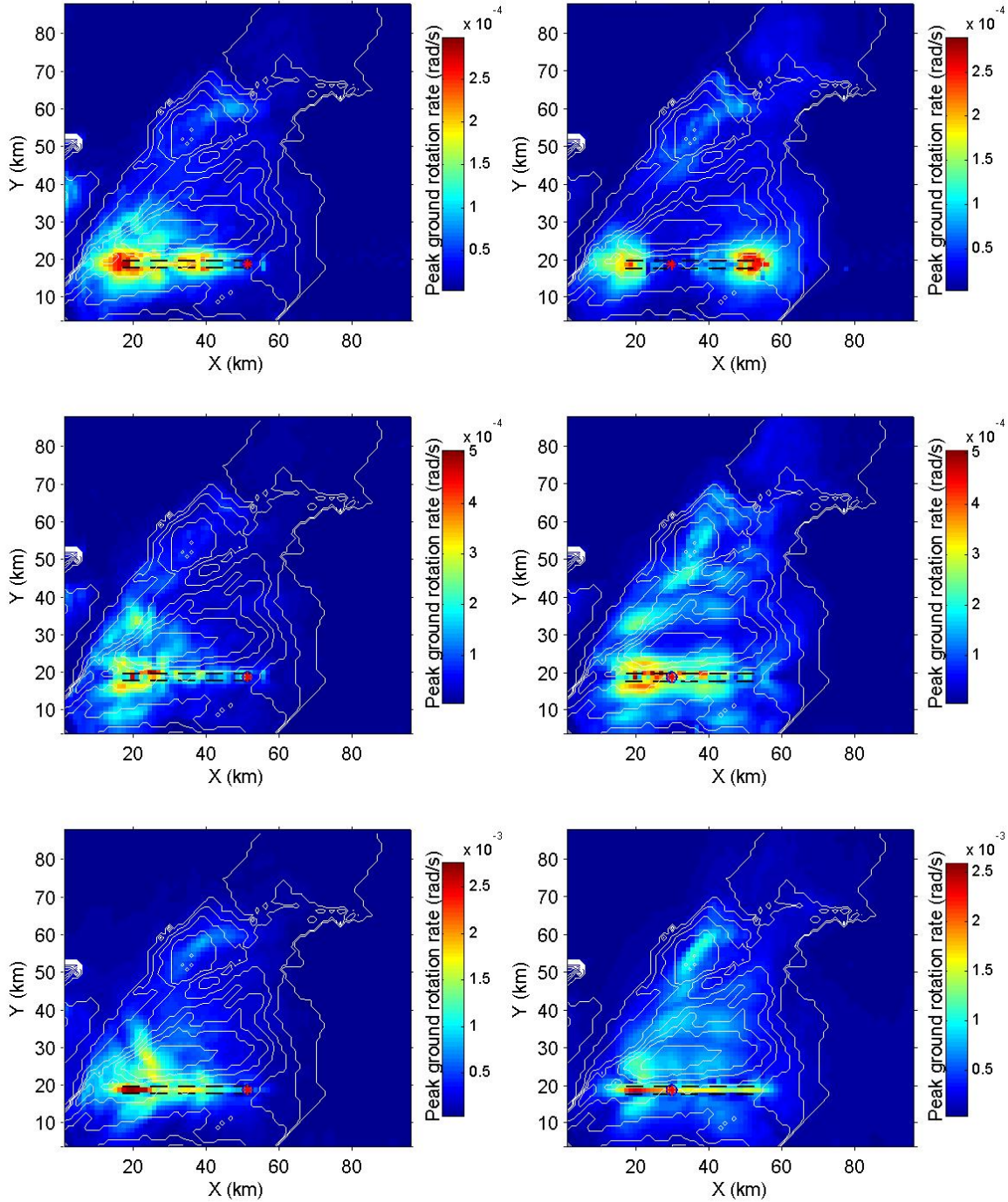


Figure 8.2: PGRR distributions for two example hypocentres. **Left.** H1 (Fig. 6.1). **Right.** H2 (Fig. 6.1). From top to bottom are x -, y - and z -components, respectively. The epicentres are indicated as red asterisks. The black dashed rectangle indicates the fault trace. Thin white lines are contours of the seismic velocity model. Note the color scale difference.

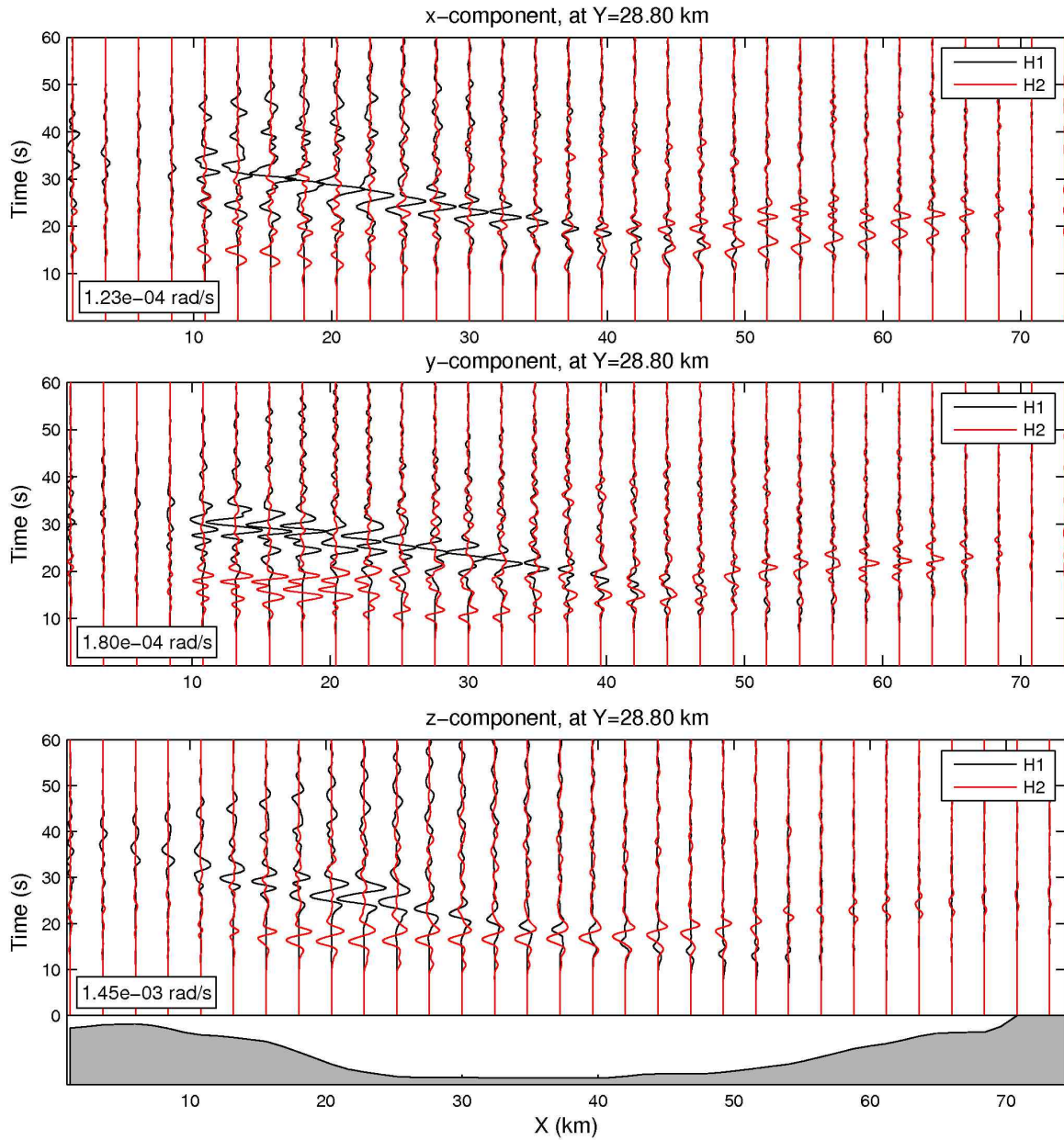


Figure 8.3: Rotation rate profile for the two example hypocentres: parallel to the fault trace. From top to bottom are the x -, y - and z -components, respectively. The shear wave velocity isosurface depth (at 2.0 km/s) is depicted in the bottom as the shadowed area. The maximum rotation rate amplitudes across this profile are shown with the inlet number.

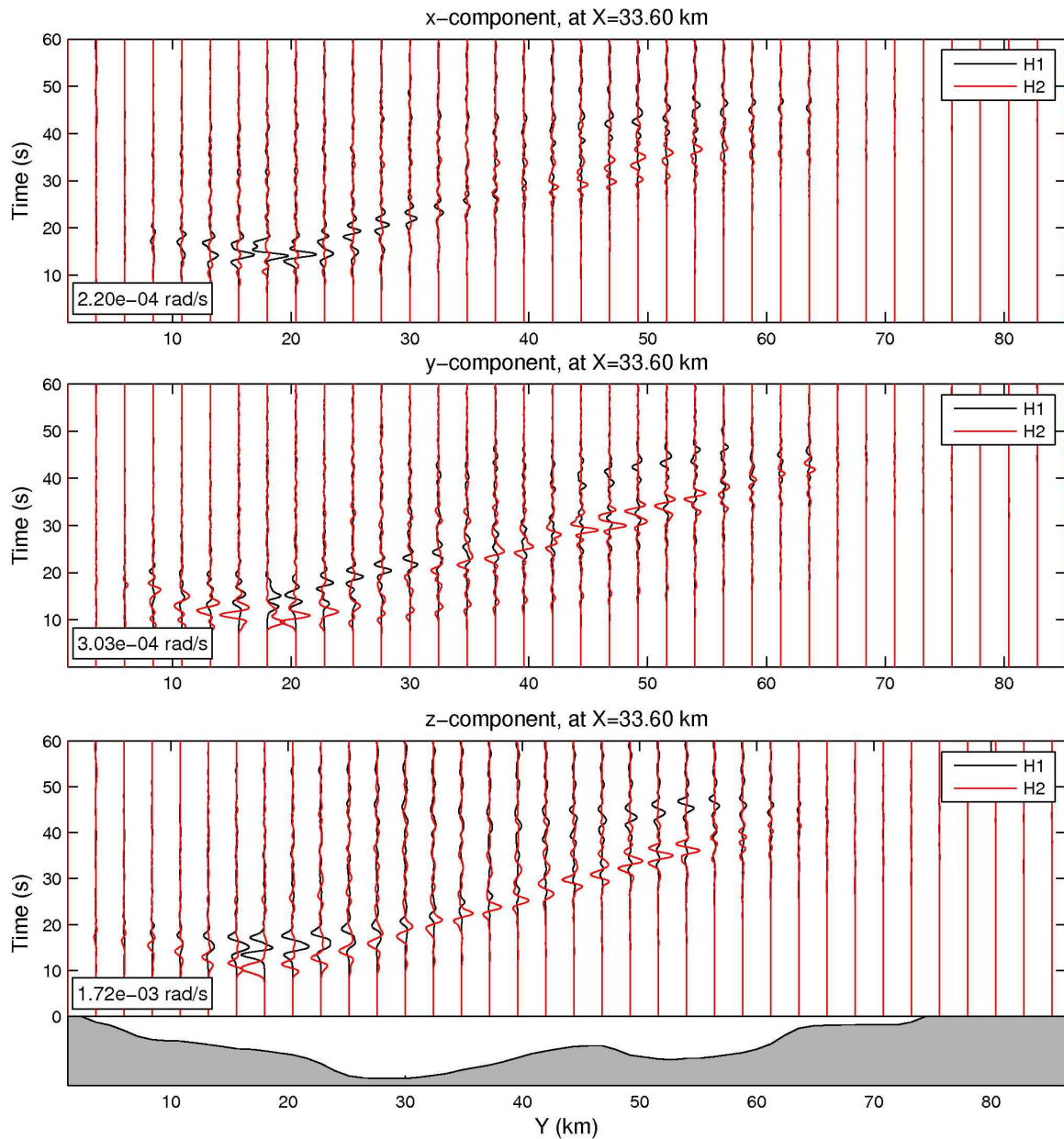


Figure 8.4: Rotation rate profile for the two example hypocentres: perpendicular to fault trace. From top to bottom are the x -, y - and z -components, respectively. The shear wave velocity isosurface depth (at 2.0 km/s) is decorticated in the bottom as the shadowed area. The maximum rotation rate amplitudes across this profile are shown with the inlet number.

basin wide shaking, fault-distance dependent ground motion, and peak motion uplifted by the slip asperity. Two ratios are calculated and shown to characterize the variations: R_{SD} – the one of the standard deviation relative to the mean value, and R_{max} – the one between the maximum value and the mean value.

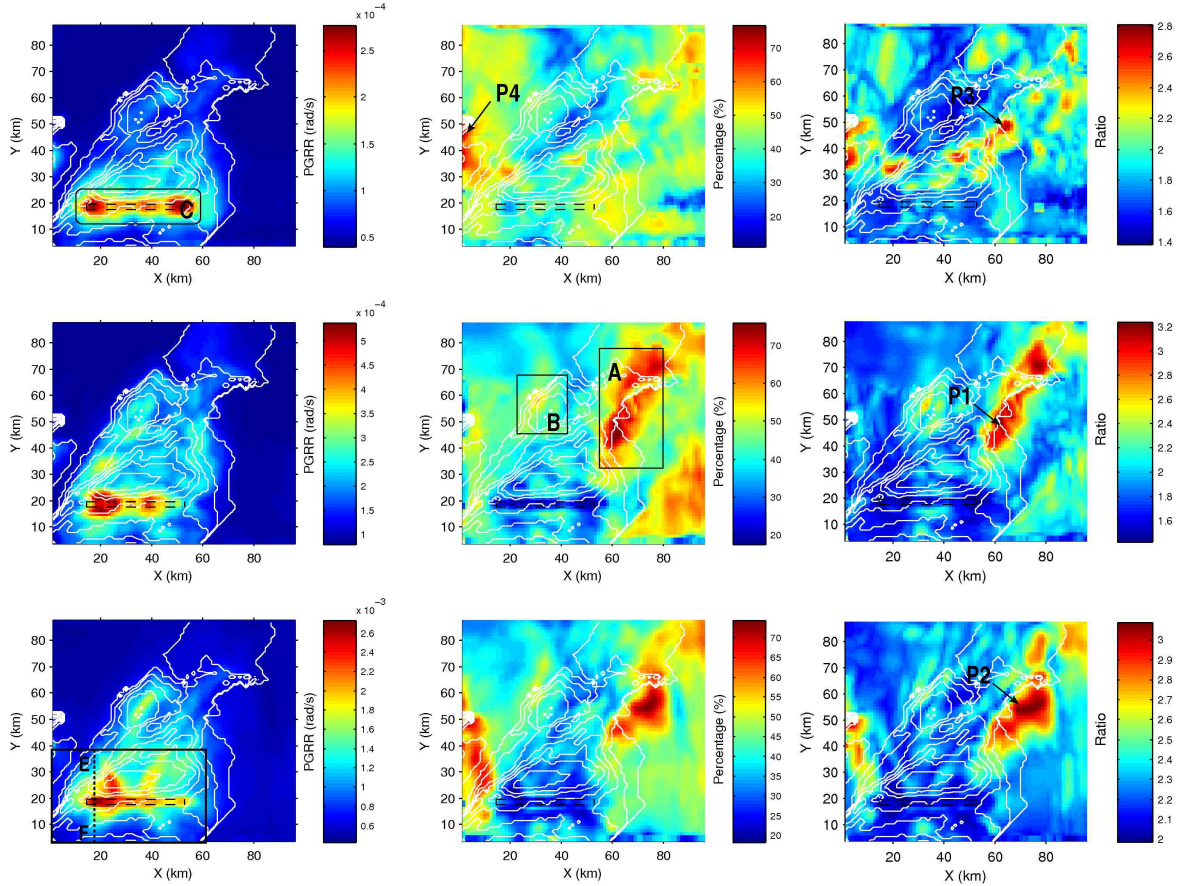


Figure 8.5: Properties of the PGRR distributions due to varying hypocentre. **Left.** Maximum value. **Middle.** The ratio between the standard deviation and the mean PGRR value (combination of all 24 simulations) in percent. **Right.** The ratio between the maximum value and the mean value. From top to bottom are x -, y - and z -components, respectively. The black dashed rectangle is used to indicate the fault trace to avoid masking the high values on the fault trace. Thin white lines are contours of the seismic velocity model. Region A, B and C and station P1, P2 and P3 are picked up for more detailed discussion. Station R1 and R2 are used to analyze the hypocentre depth effect on the ground rotation rate (amplitudes and seismograms). Profile EF is used to illustrate the rotation rate variation across the fault trace. Note the color scale difference.

The maximum rotation rate of the z -component is about 8 times larger than the x -component and 5 times larger than the y -component. Across the fault trace, the gradient of the z -component rotation rate is larger than the other two components. These two phenomena could be explained with the source mechanism – pure strike slip, and the fact that the rotation rate is the space derivative of the horizontal velocities.

In the region C (surrounding the fault trace), for the x -component (Fig. 8.5 top left),

the maximum PGRR distribution is symmetrical about the middle of the fault trace. That symmetry is not observed for the other two rotation rate components (Fig. 8.5 middle and bottom, left). For the y - and z -components (Fig. 8.5 middle and bottom, left), larger rotation rates are observed in the left part of region C (around the left tip of the fault trace) where the neighboring basin is deeper, than in the part right to the fault trace middle. This observation confirms that the fault parallel component of rotation rate receives more contributions from the directivity effect than the other two components.

The variation of the hypocentre-dependent ground motions is illustrated by showing the spatial distribution of two ratios R_{SD} and R_{max} (Fig. 8.5 middle and right). We take two example regions, A and B, where a dramatic basin depth variation is located. For the x -component, there is no obviously high values of ratio R_{SD} observed (Fig. 8.5 top right) inside these two regions. However for the y -component (Fig. 8.5 middle right) and the z -component (Fig. 8.5 bottom right), large R_{SD} is observed inside regions A and B, compared to their neighboring area. The largest R_{SD} , 75% for the y -component and 72% for the z -component, of the whole study area are all located inside region A. Right on the fault trace, the ratio R_{SD} for the x -component (Fig. 8.5 top, right) is compatible to its neighboring region, but not for the other two components (Fig. 8.5 middle and bottom, right). For all the three components, especially for the z -component, there are large R_{SD} found in the regions off the two tips of the fault trace.

The distributions in terms of ratio R_{max} are calculated and shown in Fig. 8.5 (right) for different component. The spatial distributions of this ratio for the y - and z -components (Fig. 8.5 middle and bottom, right) are quite similar to those of the ratio R_{SD} (Fig. 8.5 middle and bottom, middle): the largest value over the entire study area is observed at the same station (P1 for y -component and P2 for z -component); elevated rotation rate variations are observed in the small basin (region B); smaller variations are observed in the fault plane projection regions (region C) when compared to the neighboring area. But for the x -component, the difference between the distribution of R_{max} and R_{SD} is more obvious. The largest R_{max} happens at station P3 whereas the largest R_{SD} is at station P4. The spatial distributions of ratio R_{max} are coarser than those of the ratio R_{SD} . At the basin edge, about 2.8, 3.2 and 3.1 times larger than the mean ground rotation rate might be expected for the x -, y - and z -components, respectively, if the mean ground rotation rate could be predicted.

8.3.3 Rotation Rate Variations in the Near-Source Region

In Fig. 8.5 (bottom left), rotation rates attenuate rapidly with the increase of the distance from the fault plane. There is a slim band with very large rotation rates, right on the fault plane trace compared to the two flank areas. The highest rotation rate coincidences with the high slip asperity area (Fig. 6.1). To investigate how the rotation rates vary across the fault trace in more detail, we focus on the fault trace and zoom into a smaller area around the fault trace. The location of this smaller area is shown in Fig. 8.5 (bottom left), as black rectangle.

The peak ground rotation rate distributions for all the three components inside this smaller region are shown in Fig. 8.6. y -component (Fig. 8.6b) has very small values right on the fault trace. Right on the fault trace, the rotation rate value for the x -component Fig. 8.6a) is neither so small as the y -component, nor so large as the z -component (Fig. 8.6c). x -component rotation rates are large in the fault projection area and attenuate slower with distance than the other two components.

In Fig. 8.7, a seismogram profile EF (thick black dashed line, Fig. 8.5 bottom left) is

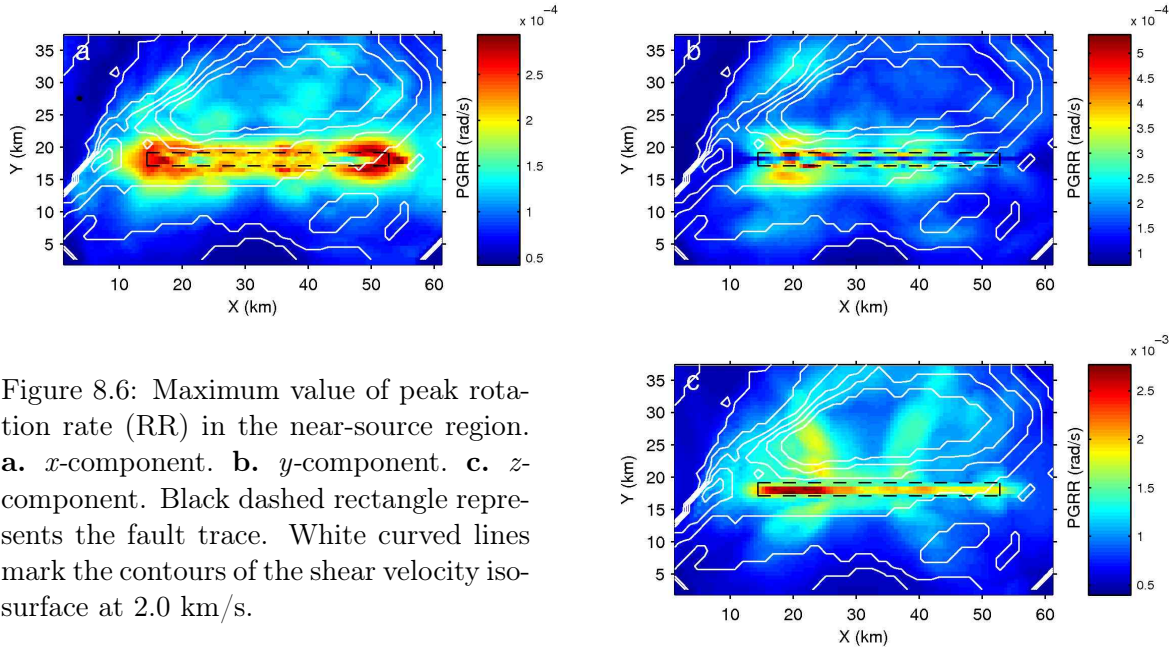


Figure 8.6: Maximum value of peak rotation rate (RR) in the near-source region. **a.** x -component. **b.** y -component. **c.** z -component. Black dashed rectangle represents the fault trace. White curved lines mark the contours of the shear velocity isosurface at 2.0 km/s.

extracted and the rotation rates on this profile are shown for the x -, y - and z -components. The fault is located at $y=18.0$ km. The depth of shear-wave isosurface (at value of 2.0 km/s) begins to decrease when y increases from 0 to 20 km. The basin effect is clearly observed in the x - and y -components, especially in the x -component. For the x -component, the amplification at the basin edge ($y \in [27, 32]$ km) is so obvious that the energy generated at this region is larger than the first arrival. For the two horizontal components, there is a phase change with the first arrival across the fault plane (located at 18.0 km) but not for the vertical component. For the y -component, almost no rotation rate is observed right on the fault plane.

8.3.4 Relationship between PGRR and Source Depth

We further investigate the relationship between the peak ground rotation rates (PGRR) and hypocentre depth. Two stations, indicated in Fig. 8.5 (bottom left) (R1, 40 km from the fault, inside the basin; R2, close to the center of the fault), are picked up for doing that. z -component rotation rate seismograms, at these two receivers and synthesized with the four hypocentres (same epicentre) as indicated in Fig. 6.1 (enclosed in the white rectangle) are shown in Fig. 8.8a and Fig. 8.8b. At station R1, the amplitudes are smaller than the station R1. But the duration times are much longer due to the reflection at the basin edge. The energy is diffused while at station R2, most shaking happens in a shorter time. The arrival time of the highest amplitude, at station R1, is later than R2. The difference of that arrival time between different hypocentres, at station R1, is much larger than R2.

The PGRRs (and variance) for all 24 simulations at stations R1 and R2 are displayed as a function of source depth in Fig. 8.8c, 8.8d, respectively. For the distant station R1 (Fig. 8.8c), the mean PGRR increases slightly with the hypocentre depth, while the variance is much larger for deeper events, indicating a stronger path-dependence for wave fields arriving from deep sources than from shallow sources. The opposite behaviours are observed for station R2 which is close to the fault in Fig. 8.8d.

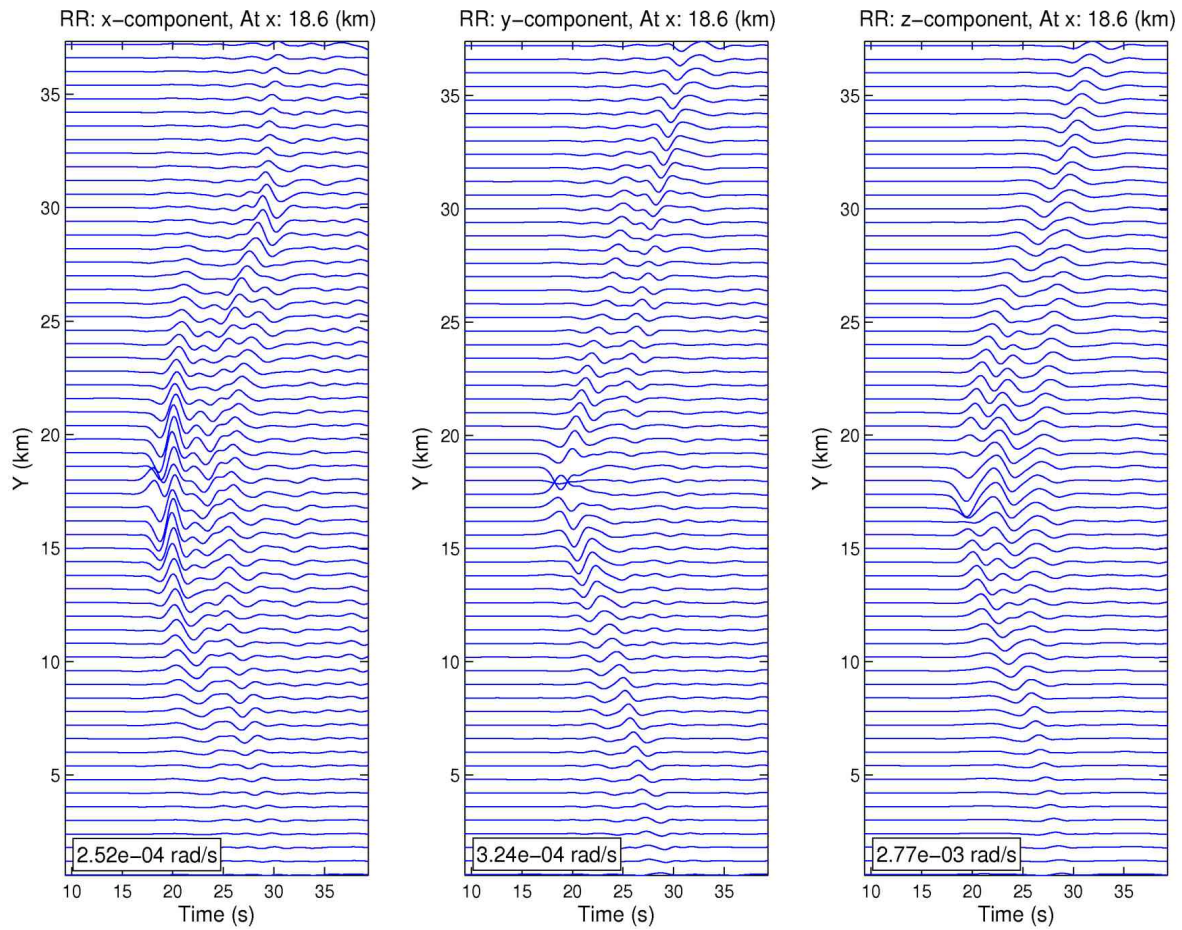


Figure 8.7: Rotation rate profiles (**EF**, Fig. 8.5 (bottom left), thick black dashed line). From left to right are the x -, y - and z -components. The inlet number is the maximum amplitude on this profile. The fault trace is located at $y = 18$ km.

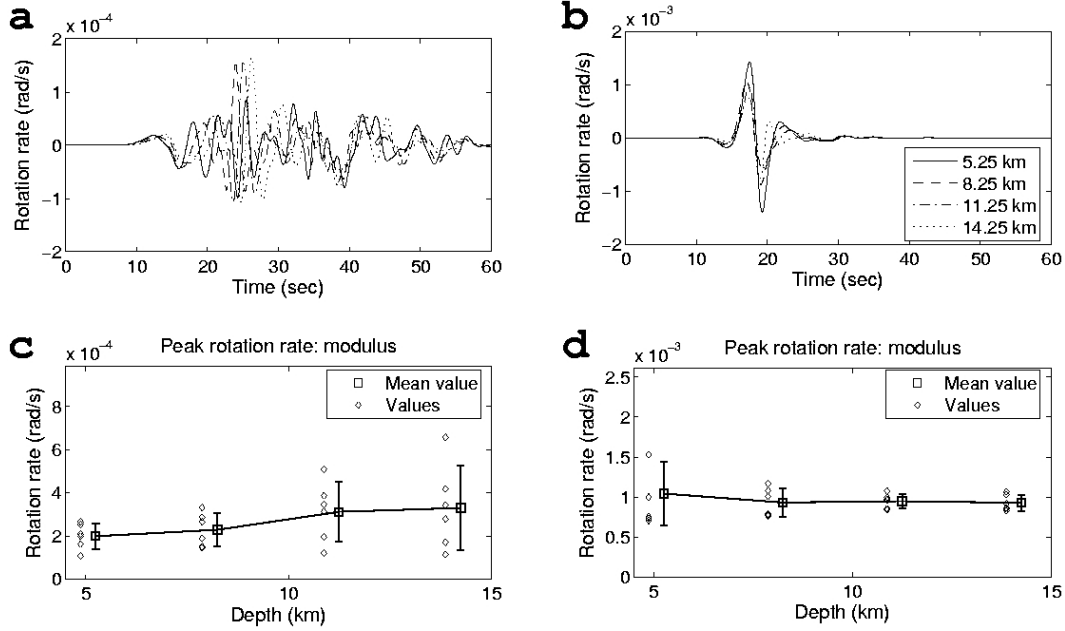


Figure 8.8: **a+b**: Rotation rate seismograms (z -component) for the M7 earthquakes with same epicentre but varying hypocentre depths (hypocentres enclosed by the white rectangle in Fig. 6.1) at stations R1 and R2 (indicated in Fig. 8.5 bottom left). **a**. R1, approx. 40 km off fault. **b**. R2, close to the fault trace. **c+d**: PGRR as well as mean and variance for all simulations. **c**. R1. **d**. R2. Mean and individual values are offset for illustrative reasons.

8.4 Slip History Effect

We design 20 slip histories (with hypocentre fixed, same as in chapter 7) with which ground rotation rates are calculated. The aim is to investigate the composite effect of the medium and the source complexity on the ground rotation rates, and to provide a possible range of the ground rotation rates introduced by the possible M7 earthquakes inside our study area. The results are shown and analyzed in the following sections.

8.4.1 Average PGRR Characteristics

The mean values of all 20 resulting peak ground rotation rates (PGRRs) on the surface are shown in Fig. 8.9 for three components. The area, with the mean PGRR (x -component) larger than 0.9×10^{-4} rad/s (black rectangle, Fig. 8.9 left), is the area towards which the rupture propagates and where the directivity plays the most important role (as explained in chapter 5). We name that area as A. The mean PGRR in this area for the x -component (fault parallel) is larger than other parts of the study area. Meanwhile, for another horizontal component, no such PGRR distribution is found. Elevated rotation rates are observed inside the basin but outside area A both for the y -component (largest value is located at the basin edge) and the vertical component. For the y -component, inside the region B, the rotation rates are even compatible to those right on the fault trace. Thus it can be concluded that the x - and z -components (fault-parallel) are dominated by the directivity effect and the y -component has significant contributions from the 3D structure (basin effects) and slip history.

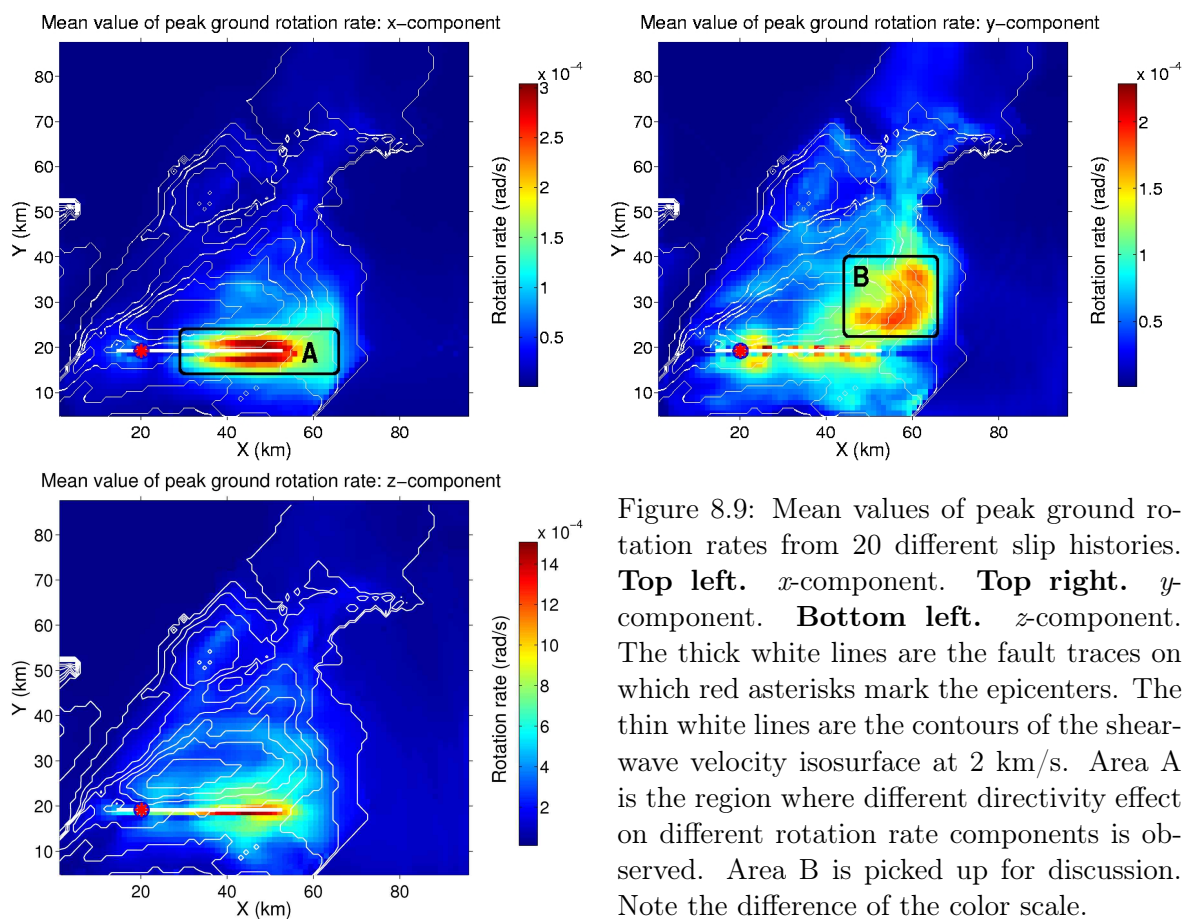


Figure 8.9: Mean values of peak ground rotation rates from 20 different slip histories. **Top left.** x -component. **Top right.** y -component. **Bottom left.** z -component. The thick white lines are the fault traces on which red asterisks mark the epicenters. The thin white lines are the contours of the shear-wave velocity isosurface at 2 km/s. Area A is the region where different directivity effect on different rotation rate components is observed. Area B is picked up for discussion. Note the difference of the color scale.

8.4.2 Source Dependent PGRR Variations

Four representative slip histories are taken as examples² and the resulting rotation rates are shown and compared in this section to investigate the effects of slip history on the ground rotation rate in more detail. The results are shown in Fig. 8.10. The final slip distributions are shown in the top line. These slip models are considered to be representative because of the following reasons: slip 5 has a distinct asperity area right in the middle of the fault plane; slip 7 has a smaller asperity area with very large slip close to the hypocentre; slip 10 is more uniform than the other three examples; slip 16 has two asperity areas and the major broken part occurs in the bottom half part of the fault.

For slip 16, over the entire study area, the rotation rates are smaller compared to the other three slip models in all three components. Right on the fault trace, at point D where high slip asperity is nearby, large x -component rotation rate is observed for the slip model 7, but not for the other three slip models (Fig. 8.10 second line). The z -component rotation rates are elevated by the slip asperity in the region C for the slip model 7 (Fig. 8.10 fourth line). There are not such elevations for the slip models of 10 and 16. For the y -component, at the point B, close to the asperity area of slip 5, large rotation rate is observed, compared to the other three slip models (Fig. 8.10 third line). Comparison between different components of PGRRs inside area A (Fig 8.9), suggests that the directivity plays a more important role on the x -component (the fault parallel one).

The characteristic properties of the peak ground rotation rates are summarized and shown here. The maximum, the standard deviation and the relative variations are adopted. Two ratios are calculated and shown to characterize the relative variations: R_{SD} – the one of the standard deviation relative to the mean value, and R_{max} – the one between the maximum value and the mean value. The aim is to provide the rotation rate range excited by these hypothetical M7 earthquakes. We show those ground rotation rate characteristics in Fig. 8.11 for different rotation rate components.

Both the largest rotation rate and the largest standard deviation of the entire study area for the vertical component are 4.5 times larger than those of the x -component and 6 times larger than those of the y -component. These largest ratios are located either right above (x - and z -component) or very close to the fault trace (y -component). For the vertical component, very large gradients of rotation rate are observed at the two sides of the fault trace. For the y -component, the largest rotation rate happens around the epicentre while that for the other two components is located a bit further from the epicentre (right on the fault trace, at the far end of the fault trace (with respect to the epicentre)). Similar spatial distributions are found in terms of the standard deviation, too. A bit further from the fault trace, e.g., at station E, there are still large standard deviations and maximum values for the y -component (Figure 8.11, middle) which are compatible to those on the fault trace. Large rotation rate values and standard deviations are also observed for the vertical component at this station. But for the x -component, these two variables are quite small compared to those on the fault trace.

The spatial distributions of ratio R_{SD} between the standard deviations and the mean values of all 20 simulations are shown in Fig. 8.11 (bottom) to characterize the variations in a relative meaning. The largest R_{SD} of the entire study area is 420% for the x -component, 50% for the y -component and 45% for the vertical component, respectively. The difference is where it happens. For the x -component, R_{SD} is very big inside the region F which is centered

²All the PGRR distributions corresponding to these 20 slip histories are shown in Appendix B.

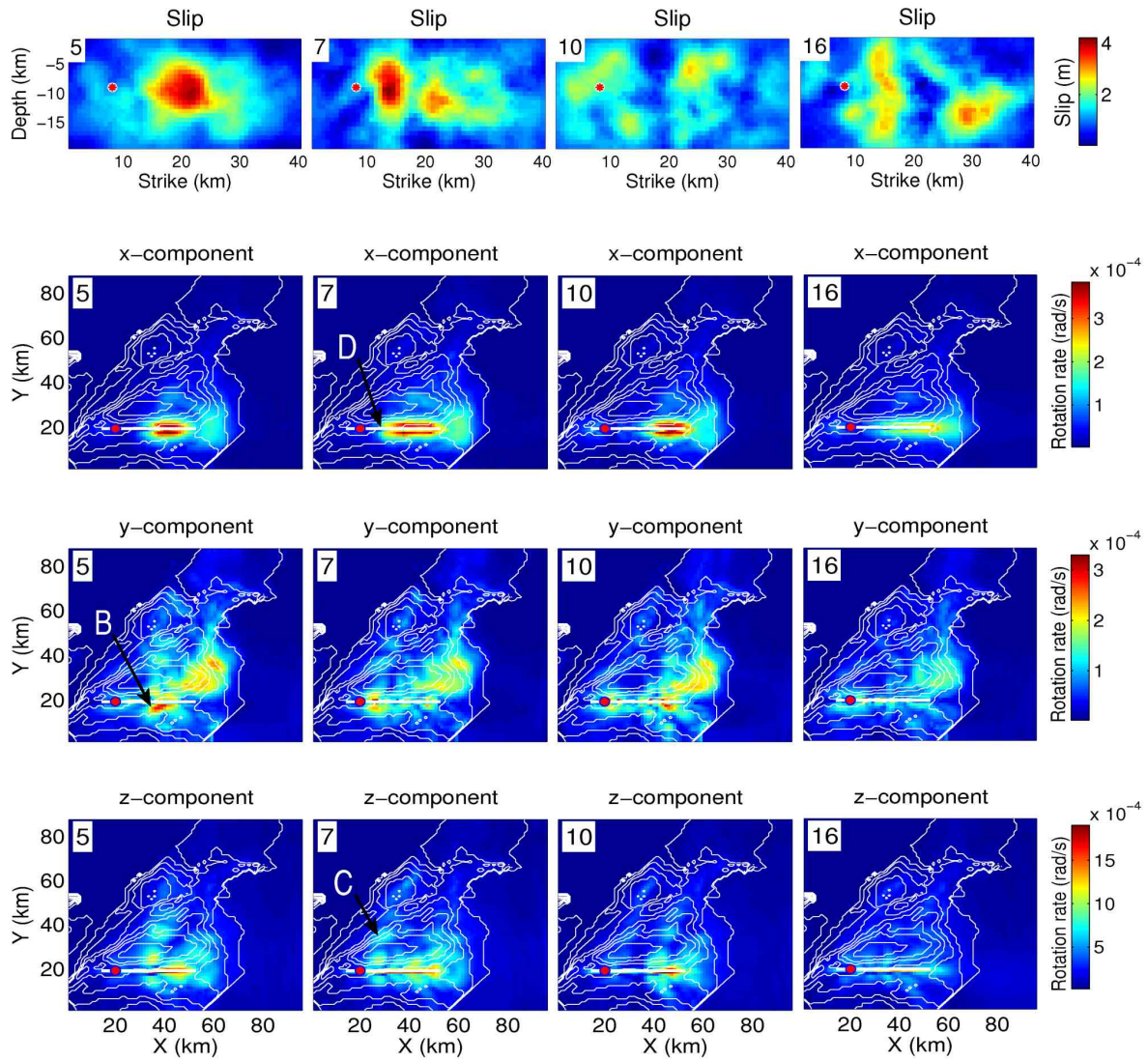


Figure 8.10: Peak ground rotation rate distributions from slip model 5, 7, 10 and 16. The corresponding slip distributions are shown in the top line. The thick white line is the fault trace on which red asterisk marks the epicentre. The thin white lines are the contours of the shear-wave velocity isosurface at 2 km/s. Region B, C, and D are picked up for discussion.

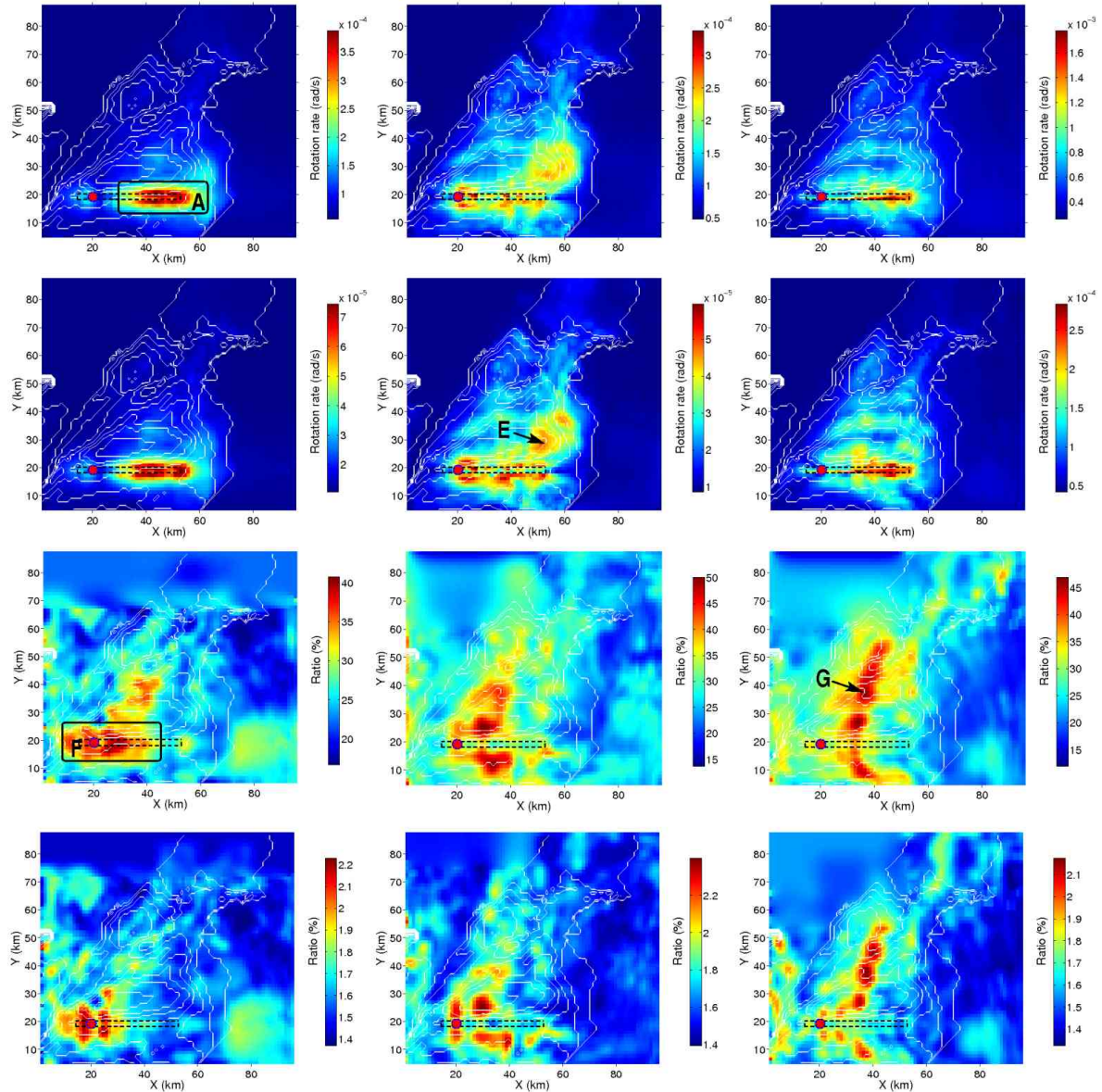


Figure 8.11: Peak ground rotation rate variation – maximum, standard deviation and variations (measured by two ratios: the one between the standard deviation and the mean value; and the one between the maximum value and the mean value). **Top.** Maximum value. **Second line.** Standard deviation. **Third line.** Ratio between the standard deviation and the mean value. **Bottom.** Ratio between the maximum value and the mean value of the individual PGRRs. From left to right are the x -, y -, and z -components. Fault trace is marked as black dashed rectangle and epicentre is shown with red asterisk. Thin white lines are the contours of the shear velocity isosurface at 2.0 km/s. Station E and G, and region A and F are picked up for more detailed discussion. Note the color scale difference.

with the epicentre. For the other two components, the high ratios are restricted inside the band region which is right across the fault trace at the center. At the point G (basin edge), high ratios are found for the y - and z -components, but not for the x -component.

The spatial distributions of the ratio R_{max} are also shown in Fig. 8.11 (bottom line) for different components. These distributions are quite similar to those in terms of R_{SD} : the largest values of the entire study area are observed at the same stations; similar source effects are observed between different components; and similar effects due to structure are also observed. The slight difference is the spatial distributions for this ratio are coarser than those for the ratio of R_{max} .

Considering the location of stations E and G (the basin edge), the following conclusion can be made: between different components, the source and the medium plays different role in the generation of surface rotation rate. The directivity effect will dominate the fault parallel component with the absolute amplitude while the medium has equivalent contribution to the variation. Meanwhile for the other two components, sub-surface structure will control the ground rotation rates, both in terms of absolute amplitude and variation.

8.5 Comparison with Translations

In the following, the vertical rotation rates are compared with the horizontal accelerations in detailed respects, such as the waveform similarity and how the amplitude ratio is related to the medium parameters. The possible hints mainly concern what could be revealed with the joint processing of these two groups of motions.

8.5.1 Seismogram Profiles

First, the waveform similarity is investigated by showing three seismogram profiles. All the seismograms are synthesized with the hypocentre H4 (Fig. 6.1). The rotation rate seismograms on these profiles (parallel to the y -axis and located at $x=19.2$ km, $x=42.0$ km and $x=55.2$ km) are plotted in Fig. 8.12 for the x -component acceleration and the vertical rotation rate. These two different groups of seismograms are all scaled by the maximum amplitudes of the respective profiles. On the profile $x=19.2$ km, both the acceleration and the rotation rate attenuates faster with the increase of y than the other two profiles. In the range of $y \in [22, 30]$, the major parts of the seismograms are similar between the acceleration and the rotation rate. On the profile $x=42.0$ km, the acceleration and rotation rate seismograms are almost identical when y is larger than 22 km, only 3 km from the fault trace. For stations ($y < 16$) the seismograms between these two groups of motions are also similar, but in an inverse way. On the profile $x=55.2$ km, for stations ($y > 50$ km), the accelerations and the rotation rates are almost identical. In the range $y \in [22, 50]$ km, the first half (in time) of the seismograms are not similar any more and the difference increases with the decrease of the distance from the fault trace. But the second halves of the seismograms are still similar. On all three profiles, the accelerations are totally different from the rotation rates in the range $y < 22$ km.

The y -component accelerations on the former three profiles are shown in Fig. 8.13 together with the vertical rotation rates. On the profile $x=19.2$ km, the waveforms are quite similar between the y -component acceleration and the vertical rotation rate. On the profile $x=42.0$ km, the accelerations are also similar to the rotation rates in waveform, except in the range surrounding the fault trace where large difference is observed between the one-impulse-like

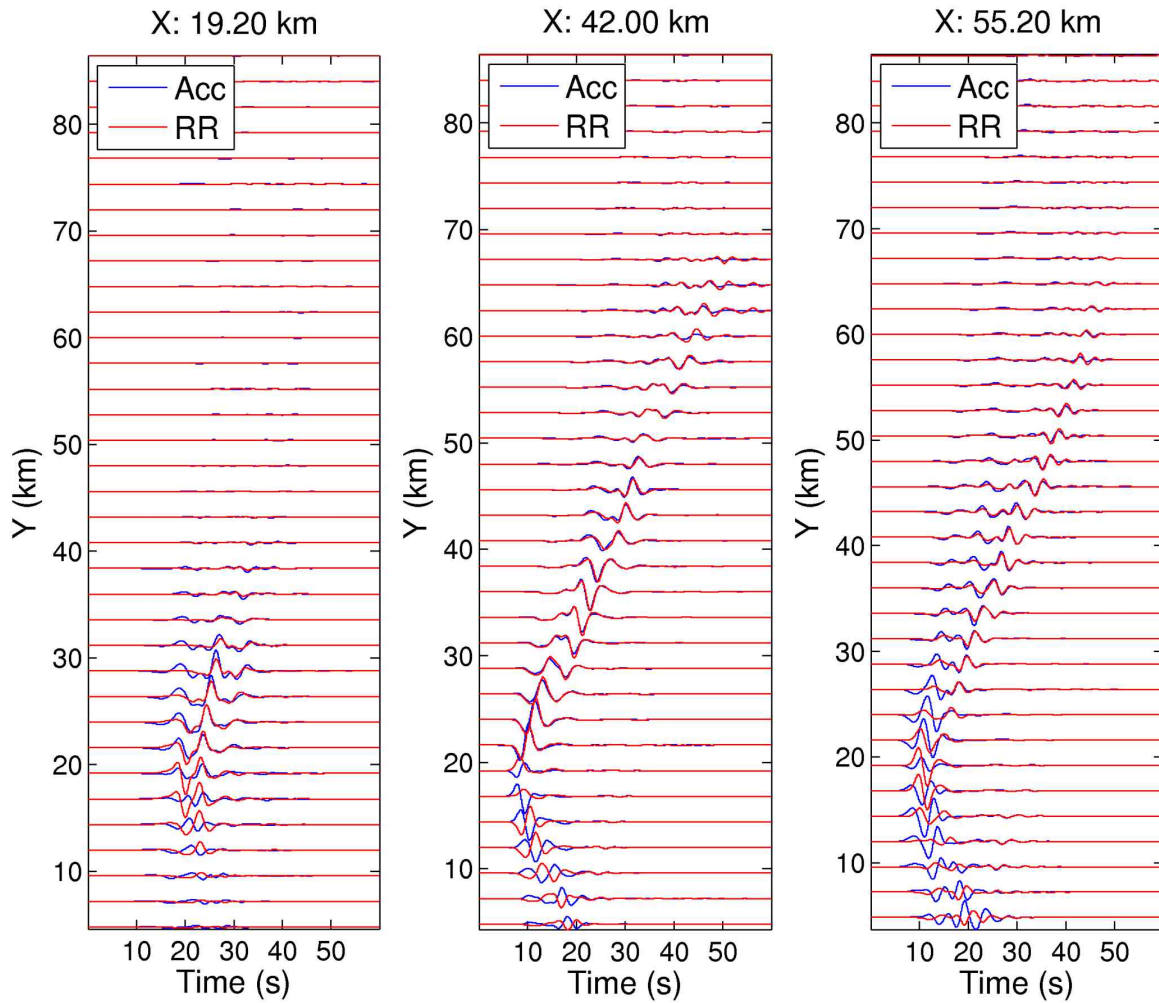


Figure 8.12: Acceleration (x -component) and rotation rate (z -component) profiles. The location of the profile is shown in the title. The accelerations and rotation rates are scaled by the maximum amplitude of the corresponding profile, respectively.

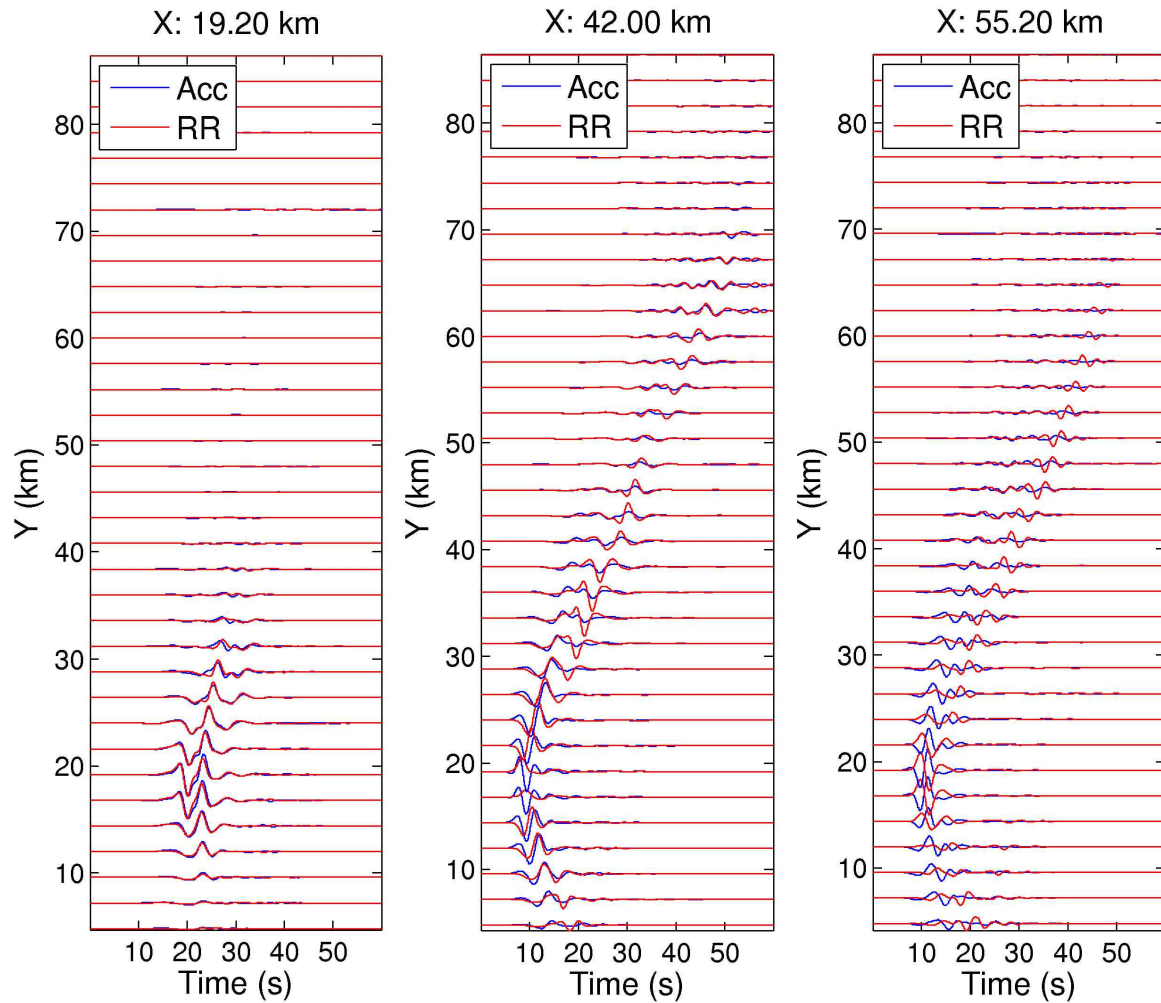


Figure 8.13: Acceleration (y -component) and rotation rate (z -component) profiles. The location of the profile is shown in the title. The accelerations and rotation rates are scaled by the maximum amplitude of the corresponding profile, respectively.

rotation rate and the two-impulses-like acceleration. For the profile $x=55.2$ km, almost no similarity is observed between the waveforms of the acceleration and the rotation rate.

8.5.2 Waveform Similarity

To measure the waveform similarity for the entire study area, the term peak correlation coefficient (PCC) between two seismograms (one horizontal acceleration and vertical rotation rate at a station of the study area) is calculated and the results are shown in Fig. 8.14 for two acceleration components, respectively. The higher the PCC, the more similar are the waveforms and PCC being 1 means that two seismograms are identical (without considering the amplitude difference and the possible time shifting). The hypocentre adopted, H4, is shown in Fig. 6.1.

For the x -component of acceleration (Fig. 8.14 Left), in most region, the PCCs are larger than 0.75. The highest PCC is found in the region right above the epicentre. Also large PCCs are found right below the epicentre, namely in region $x \in [35, 55]$ and $y \in [5, 20]$. Small PCCs are found in the regions between two lobes of the S-wave radiation pattern (Fig. 5.9), 45° to the fault trace from the epicentre.

For the y -component of acceleration (Fig. 8.14 Right), in the regions in front of and behind the rupture propagation, PCCs are larger than 0.75. The PCC changes very fast between the major region of low PCCs ($y \in [30, 83]$) and the regions of high PCCs (off the two tips of the fault trace). The points, where big gradients of PCC are found, are roughly aligned in an angle of 45° to the fault trace from the epicentre. In contrast to the x -component, large PCCs are found right inside one region surrounding the fault trace except for a very narrow zone (concentrated with the epicentre and perpendicular to the fault trace).

Roughly speaking, the regions with large PCCs ($>85\%$) for the y -component, plus those for the x -component cover the entire study area. This fundamental conclusion is the basis for the next step of work.

8.5.3 Amplitude Ratio and Medium Parameter

Since in most study area, the horizontal accelerations are quite similar to the vertical rotation rates, it should be insightful to show the amplitudes between the accelerations and the rotation rates. Based on the plane wave propagation, the amplitude ratio between the horizontal acceleration and the vertical rotation rate at a station is theoretically derived to be 2 times the phase velocity (Igel et al. (2005)). In the following, we plot out that ratio over the study area together with the basin depth (isosurface of the shear wave velocity at 2 km/s which the local phase velocity is strongly related with). Both the case of varying hypocentre and varying slip history are shown and compared with each other.

For each point on the surface, the mean value of the peak ground accelerations is denoted as M_{PGAx} for the x -component and M_{PGAy} for the y -component, respectively. And the mean value of the peak ground rotation rates (vertical component) is denoted as M_{PGRRz} . The ratios between them, M_{PGAx}/M_{PGRRz} and M_{PGAy}/M_{PGRRz} , are shown in Fig. 8.15 (top and middle), respectively. The results from the varying hypocentre case are shown in the left column and the results from the varying slip history case are shown in the right column (Fig. 8.15).

Inside the basin (small phase velocity is approximated) and far from the fault plane, for the x -component of acceleration (Fig. 8.15 top), the ratio is small, less than 2000 m/s. Outside of

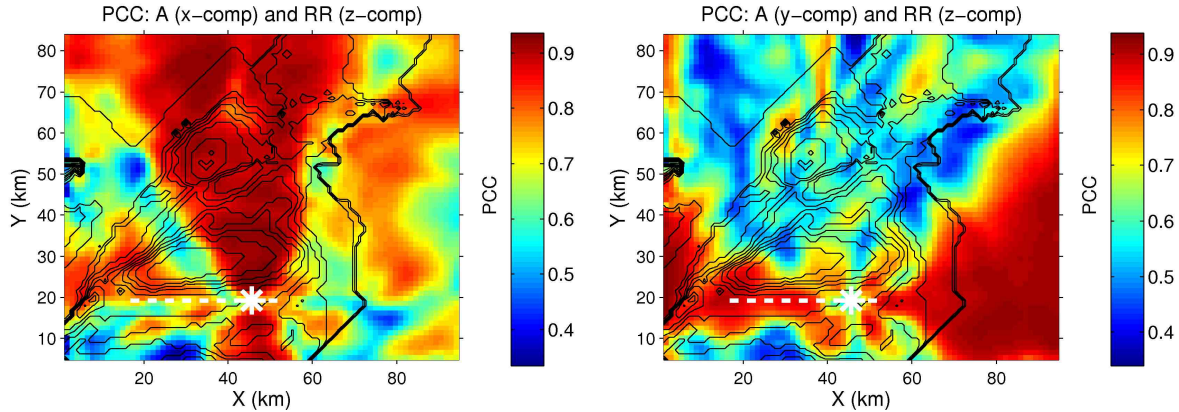


Figure 8.14: Peak correlation coefficient (PCC) between the waveforms of the horizontal accelerations and the vertical rotation rate over the entire study area for the hypocentre H4 (Fig. 6.1). **Left.** x -component of acceleration. **Right.** y -component of acceleration. The contours of the isosurface of shear wave velocity at 2.0 km/s are depicted with the thin black lines. The white thick dashed line marks the fault trace and the white asterisk marks the epicentre. Note the different color scale.

the basin, except for the region A, the basin depth is zero which means large phase velocity should be estimated. The ratio is also larger than 3000 m/s. In the region A where high phase velocity is estimated, the ratio is still low (< 1000 m/s). This region is right to the fault trace where directivity effect dominates the generation of the ground motion. In the region around the left tip of the fault trace and inside the basin, for both the case of varying hypocentre and the varying slip history, the ratio is distinctly larger than 4000 m/s and not compatible to the local phase velocity any more (Fig. 8.15 top).

For the y -component of acceleration, in the region B (outside the basin and thus large phase velocity is estimated), the ratio between the acceleration and the vertical rotation rate is less than 1700 m/s for the varying hypocentre case (Fig. 8.15 middle left). No strong relation between the amplitude ratio and the basin structure exists any more. But for the varying slip history case (Fig. 8.15 middle right), the ratios are much more compatible to the local phase velocities inside this region. In the band region C (surrounding the fault trace and right in front of the rupture propagation direction for the fixed hypocentre), the ratio are obviously higher than the local phase velocity.

The simple average between those two ratios, $(M_{PGA_x}/M_{PGRz} + M_{PGA_y}/M_{PGRz})/2$ are shown in (Fig. 8.15 bottom) for both varying hypocentre and varying slip history. A strong relation is observed over the entire study area between the amplitude ratio and the local phase velocity (Fig. 8.15 bottom) for both the varying hypocentre case and the varying slip history case, except for the regions around the two tips of the fault trace. The compatibility between the ratio and the local phase velocity holds over almost the entire study area. What should be mentioned is that, in the middle of region A, slight difference is found between the varying hypocentre case and the varying slip history case, the ratio of the varying slip history case is smaller than that of the varying hypocentre case (which is closer to the local phase velocity).

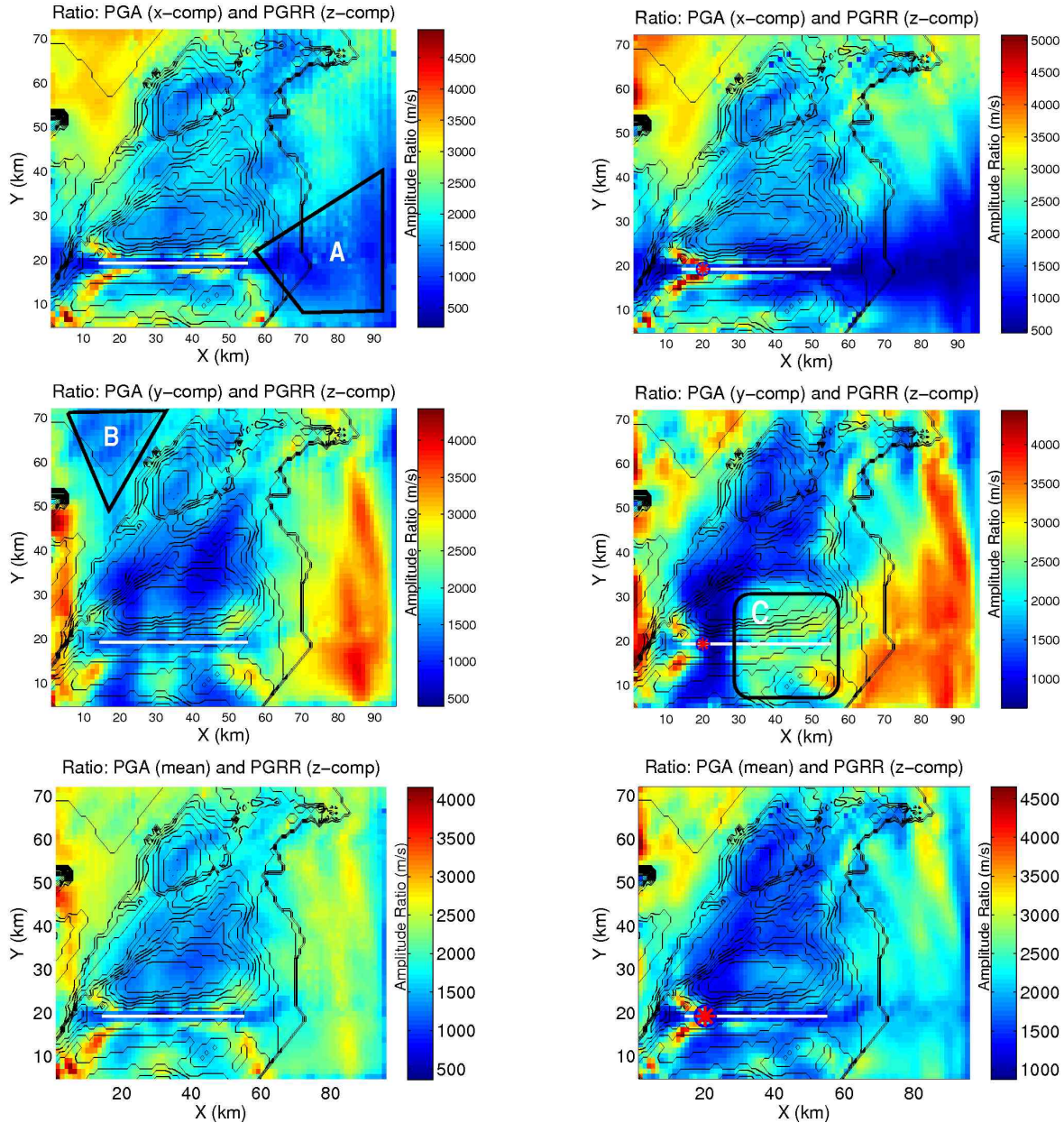


Figure 8.15: Ratio between peak acceleration and peak rotation rate. Rotation rate: z -component. **Top.** Acceleration: x -component. **Middle.** Acceleration: y -component. **Bottom.** Geometric mean of the two horizontal accelerations. **Left.** Varying hypocentre. **Right.** Varying slip history. The ratio is represented with the color-scale. Black curved lines mark the contours of the shear-wave velocity isosurface at value of 2.0 km/s . The red asterisk marks the epicentre for the case of varying slip history. Region A, B and C are picked up for illustration. Note the color scale difference.

8.5.4 Peak Ground Acceleration Distribution

The peak ground acceleration (PGA) distributions are shown in the following, together with the standard deviation (SD) and the variation distributions (measured by the ratio between the SD and the mean value). The spatial distribution comparisons between the accelerations and the rotation rates are described here with respects to varying hypocentre and varying slip history cases.

Varying Hypocentre

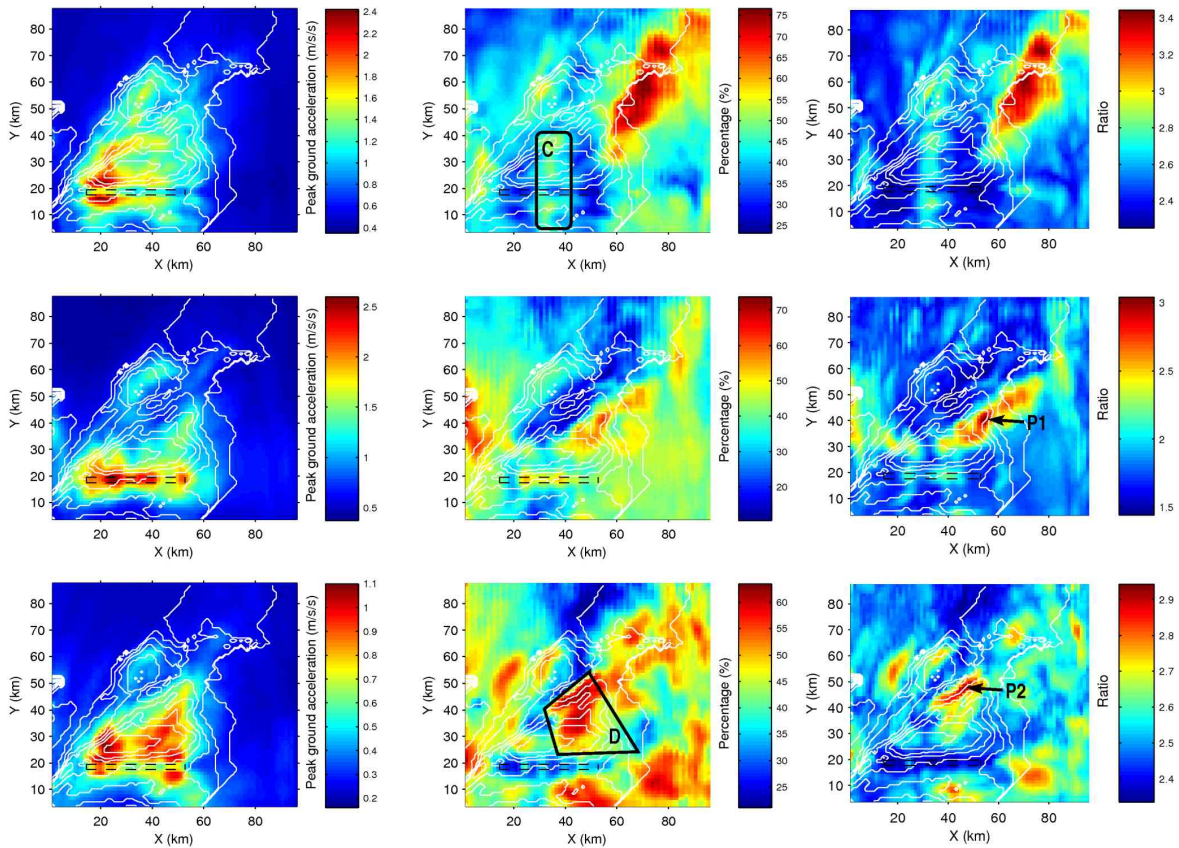


Figure 8.16: Peak ground acceleration variation due to varying hypocentre location. **Left.** Maximum value. **Middle.** Ratio between the standard deviation and the mean value (in percent). **Right.** Ratio between the maximum value and the mean value. From top to bottom are the x -, y -, and z -components, respectively. Fault trace is marked with the dashed black rectangle. Thin white lines are the contours of the shear velocity isosurface at 2.0 km/s. Region C and D, and stations P1 and P2, are picked up for more detailed discussion. Note the color scale difference.

The maximum PGA distributions and the variation distributions from the case of the varying hypocentre, are shown in Fig. 8.16. Two ratios are calculated and shown to characterize the variations: R_{SD} – the one of the standard deviation relative to the mean value, and R_{max} – the one between the maximum value and the mean value. First, as observed in the left

column of Fig. 8.16, the two horizontal components of acceleration are 2 times larger than the vertical component while the vertical rotation rate is at least 5 times larger than the horizontal components (Fig. 8.5, left column). Secondly, larger PGAs are found around the left tip of the fault trace in the x -component than around the right tip, like what is observed for the y -component of PGRRs. Also small values are observed right on the fault trace for both the x -component of acceleration and the y -component of rotation rate. Thirdly, the y -component of acceleration is more evenly distributed on the fault trace like the x -component of rotation rate does (Fig. 8.5, left). No similarity in terms of the spatial distribution is observed between the vertical rotation rate and the horizontal accelerations – the rotation rate decreases faster than the accelerations when moving across the fault trace.

The ratio distributions (R_{SD} , between the standard deviation and the mean value (in percent)) are shown in Fig. 8.16 (middle column). First, the spatial distribution of the x -component acceleration looks quite similar to that of the y -component. There are large R_{SD} observed in the two regions located at the basin edge (A and B, Fig. 8.5 middle column) for both the x -component of acceleration and the y -component of rotation rate. The ratios inside region C, compared to the neighboring area, are smaller for x -component acceleration than the y -component rotation rate. Secondly, the spatial distribution of the y -component acceleration ratio R_{SD} is similar to that of the x -component rotation rate, too. No large R_{SD} are found inside the region A at all. Right on the fault trace, the ratios of the y -component of acceleration and z -component of rotation rate, are compatible to the neighboring area, too. Thirdly, large R_{SD} are observed inside the basin, e.g., region D for the vertical component of acceleration while the rotation rate R_{SD} are quite small inside this region (Fig. 8.5 bottom middle). The spatial R_{SD} distribution of the vertical component of rotation rate is not similar to any component of acceleration.

The spatial distributions of ratio R_{max} (between the maximum value and the mean value) are shown in the right column of Fig. 8.16. Those distributions are quite similar to those of the ratio R_{SD} (Fig. 8.16 left column). But an extra emphasis on the structure effect is observed at stations P1 and P2 when compared to the left regions of the study area. Unlike observed for the rotation rates, the vertical R_{max} is distributed inside a much narrower region, [2.3, 2.9, than the two horizontal components ([1.5, 3.0 and [2.3, 3.4, respectively).

Varying Slip History

We also calculate the characteristic properties of all the 20 peak ground acceleration distributions and show the results in Fig. 8.17. First, the y -component (Fig. 8.17 middle column) is almost 2 times larger than the x -component (Fig. 8.17 left column) and 3 times larger than the vertical component (Fig. 8.17 right column) while for the rotation rates (Fig. 8.11), the vertical component is the largest one and the two horizontal components are approximately equivalent in amplitude. Secondly, both the largest acceleration and the largest standard deviation are found either right on or in the neighboring region of the fault trace. Thirdly, similar spatial distributions are observed between the x -component of rotation rate (Fig. 8.11 left column) and the y -component of acceleration (Fig. 8.17 middle column) for both maximum value and standard deviation. This similarity is thought to be the exhibition of the forward directivity effect like what has been concluded in chapter 7 for the velocities. Fourthly, the largest acceleration and standard deviation of the z -component are not on the fault trace like the rotation rate. Whereas right on the fault trace the accelerations and standard deviations are very small.

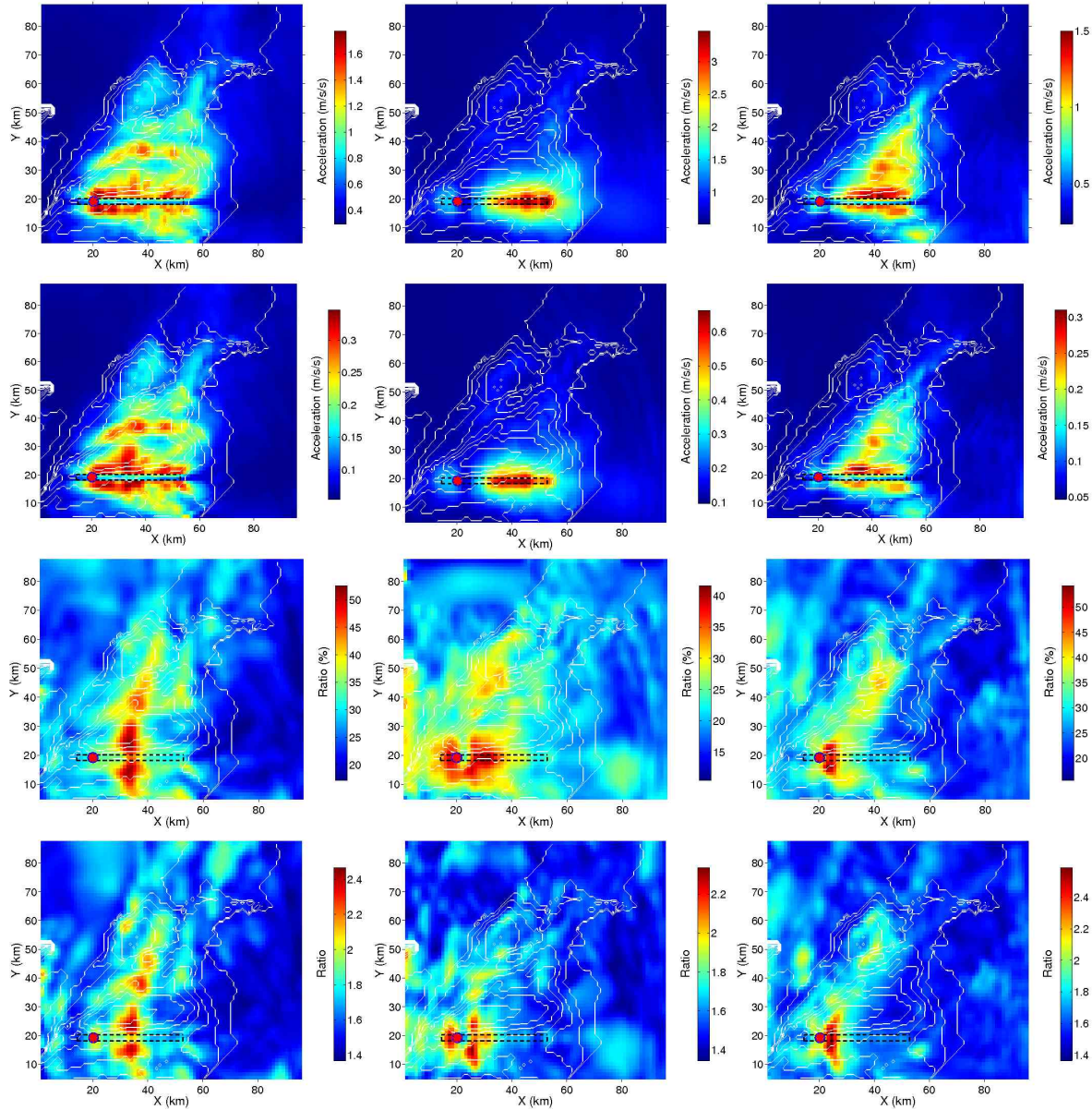


Figure 8.17: PGA – maximum, standard deviation and the variation (measured by two ratios: the one between the standard deviation and the mean value; and the one between the maximum value and the mean value) for different components. **Top.** Maximum value. **Second line.** Standard deviation. **Third line.** Ratio between the standard deviation and the mean value. **Bottom.** Ratio between the maximum value and the mean value of the individual PGVs. **Left.** x -component. **Middle.** y -component. **Right.** z -component. Fault trace is marked as dashed black rectangle and epicentre is shown with red asterisk. Thin white lines are the contours of the shear velocity isosurface at 2.0 km/s. Note the color scale difference.

In terms of the variation (measured by two ratios: the one of the standard deviation relative to the mean value, and the one between the maximum value and the mean value) the y -component has large values in the region F (black rectangle in Fig. 8.11) like the x -component of rotation rate exhibits. The variations for the rotation rates (x -component) are more widely elevated inside the basin than the accelerations (y -component). Right on the basin edge where the station G stands, high variations are observed both for all the acceleration and all the rotation rates.

8.5.5 Decay with Fault Distance

Finally, we illustrate the 2D peak value distribution with a simpler way – the peak value attenuating with the fault distance for the acceleration and rotation rate, respectively. The results are shown in Fig. 8.18 (top left for the x -component of acceleration, top right for the y -component of acceleration, bottom left for the vertical component of rotation rate). Meanwhile, in order to describe the relative variation at different fault distance, the ration between the standard deviation and the mean value at a fault distance is also shown in Fig. 8.18 (bottom right). The ground motions of all the points in the working area, simulated with the various hypocentre locations (Fig. 6.1), are shown as a function of fault distance both for the acceleration (horizontal) and rotation rate (vertical).

With the decrease of the fault distance, the amplitude of both the acceleration and the rotation rate stop to increase, or begin to saturate. For the two components of acceleration and the rotation rate, there are obvious high values in the fault distance range of [30, 50] km where the small basin is located. Inside this fault distance range, the maximum value happens at 40 km both for the acceleration and the rotation rate. Compare the acceleration and rotation rate at different fault distance, we can conclude that the rotation rate will follow the same rule to attenuate with the distance from the fault, except for the range very close to the fault. The peak amplitude of the x -component acceleration and the vertical rotation rate change more dramatically with the fault distance than the y -component of acceleration which can be seen from that ratio variation with fault distance shown in Fig. 8.18 (bottom left).

8.6 Conclusions

As what have been done for the translational motions in chapter 6 and 7, the ground rotation rates during possible M7 earthquakes in the near-source field are thoroughly investigated in this chapter. What affect the generation of the ground rotations are sub-divided into two groups: the hypocentre variations and the slip history complexity, together with the sub-surface structure. A few central questions are asked about that topic at the beginning of this chapter. The rotational motions are also recorded and stored during the building up of the numerical Green's function which enables us to fulfill that topic and answer those questions.

For two groups of parameters, namely the hypocentre location and slip scenario, the pure-strike slip source mechanism produces much larger (at least 4 times, 2.5×10^{-3} rad/s for the varying hypocentre case and 1.82×10^{-3} rad/s for the varying slip history case) vertical rotation rates than the other two components in terms of both the absolute amplitude and the standard deviation, while for the translational motions the horizontal components are larger than the vertical component. The absolute rotation rate is found to be in the same magnitude as calculated by Bouchon and Aki (1982) for layered medium. Secondly, the largest vertical rotation rate happens right on the fault trace, and there is always extremely high rotation

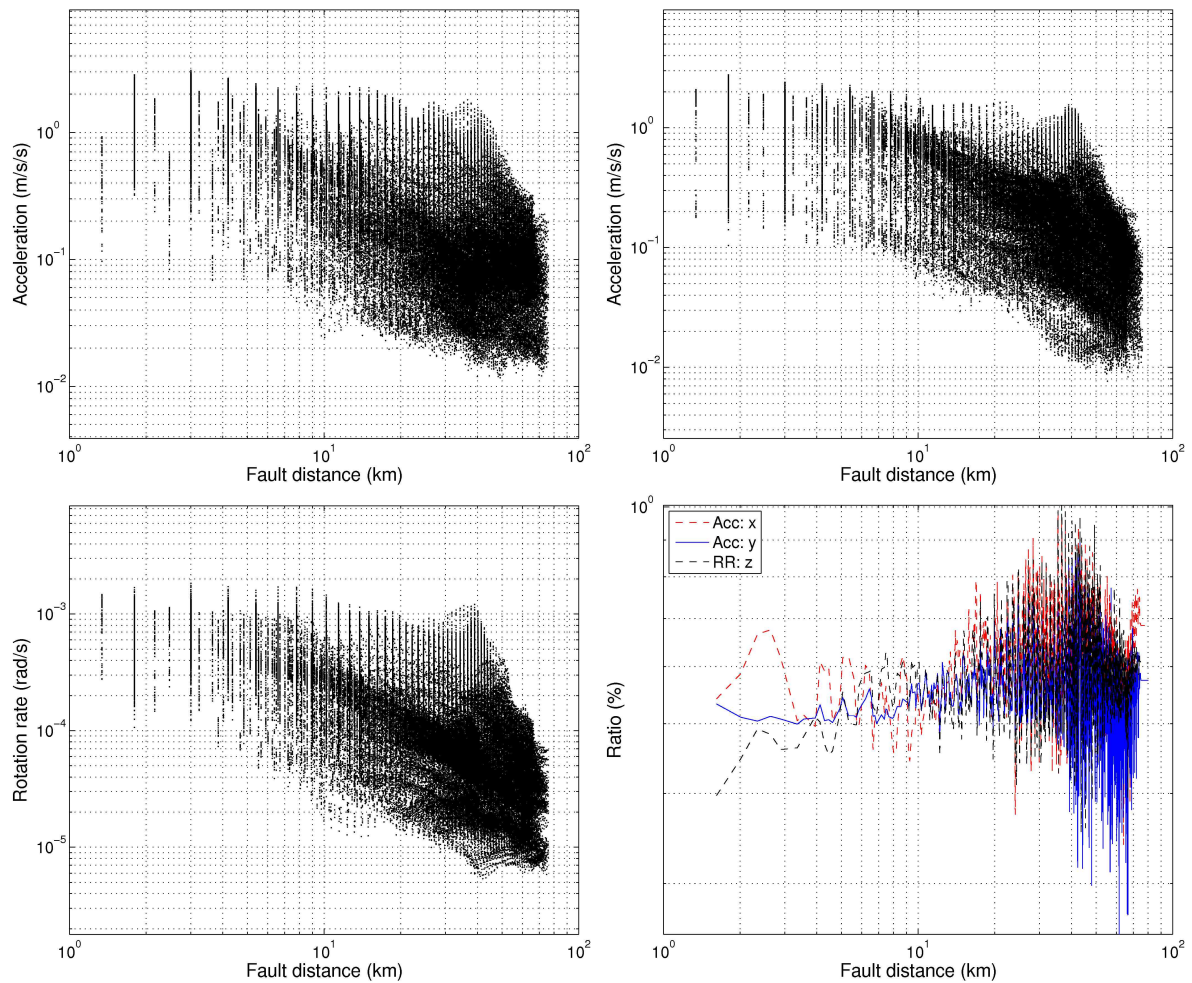


Figure 8.18: Peak ground acceleration and peak ground rotation rate as a function of the fault distance. **Top left.** Acceleration, x -component. **Top right.** Acceleration, y -component. **Bottom left.** Rotation rate, z -component. **Bottom right.** Ratio between the standard deviation and the mean value as function of fault distance.

rate gradient across the fault trace. The vertical rotation rate attenuates much faster with distance than the other two components and the translational motions.

The variation of the hypocentre location is first taken into account to investigate how the ground rotation rates are affected in the near-source field. At the regions off the two tips of the fault trace, high variations (relative to the mean values) are observed. The relative variation (ratio between the standard deviation and the mean value) are equivalent between the different components (with maximum value around 75%), which is the same for the accelerations. For the fault perpendicular component and the vertical component – the two components which are both theoretically predicted to be not affected by the forward directivity effect in chapter 5) – the basin structure elevates the variations obviously at the basin edge and thus produces the largest variation (relative to the mean value). Low variations are observed right on the fault trace and its neighboring regions where large absolute values are found both in terms of maximum absolute values and standard deviations.

The slip history complexity is taken into account as the second parameter which affects the ground rotation rates in the near-source field. Since the hypocentre is fixed to one side of the fault plane, strong directivity effect should be observed as for the velocity part in chapter 7. The forward directivity effect (depending on the hypocentre location) exhibits its distinct contributions at the far end of the fault trace and dominate the spatial distributions of the absolute values (maximum values and standard deviations) for the component which is predicted in a theoretical way to be affected mostly by this effect – the fault parallel component. However, for the other two components, much larger contributions from the sub-surface structure are observed in this region. Secondly, the variations (relative to the mean values) are found to be restricted inside the basin. There are also high variations across the fault trace at the middle point. The fact that the variations at the basin edge (20 km from the fault trace) are equivalent to those right on the fault trace, convinces us that the slip history complexity will play an equal role as the sub-surface structure in affecting the ground rotation rates. Finally, the largest variation is less than 45% for different components which is smaller than that for the varying hypocentre case (more than 70%).

We also compare these two different groups of motions. The aim is the potentiality to provide some hints into the local phase velocity as revealed by [Igel et al. \(2005\)](#) even the fundamental assumption of their – the plane wave propagation – doesn't hold in this near-source region any more.

The horizontal accelerations are compared to the vertical rotation rate in different terms. High waveform similarity between the horizontal acceleration and the vertical rotation rate, excited by a single earthquake, is observed in most of the study area, including the basin edge (strong effect from basin structure) and fault plane projection region (strong effect from the source). This similarity was explained in [Igel et al. \(2005\)](#) for the global earthquakes with a fundamental plane wave propagation assumption.

In the near-source region, the source complexity strongly affects the solution of the wave propagation. But considering the distinctly high waveform similarity over the entire study area as presented in ([Igel et al., 2005](#)), the amplitude ratio between these two kinds of motions could still be related to the media parameter, somehow. The calculations prove that that conclusion holds in most of the study area inside our frequency range.

The variations of the accelerations and the rotation rates are also compared with respect to the parameters: varying hypocentre and varying slip history, in terms of the maximum

value and ratio between the standard deviation and the mean value. Directivity effect on the variations of these two groups of motions are quite similar in terms of spatial distribution of the maximum values and standard deviations for both the varying hypocentre case and the varying slip history case. Sub-surface medium has larger contributions to the accelerations than the rotation rates. The pure-strike slip source mechanism dominates the rotation rate direction, mostly around the vertical axis while the translations are restricted in the horizontal directions. Also, this source mechanism leads to much higher gradient for the vertical rotation rates across the fault trace than for the accelerations.

Finally, how the rotational energy attenuates with the distance is extracted and compared to that of the accelerations. The same trend is found with which peak rotation rate attenuates with the fault distance, in most of our working area. As well as the waveform similarity between these two different groups of motions, this finding implies a possible way to design the rotation rate where no rotational instrument is running but plenty of accelerograph records are available.

The major inefficiency in this chapter is still frequency limitation exerted by the numerical method. In the future, more simulations should be carried out with smaller grid-length and thus high frequency could be included. If the acceleration and rotation rate still decay in the same way with the fault distance, our conclusions could be applied to a larger frequency range.

Chapter 9

Conclusions and Discussions

In the near-source region, both the source scenario and the sub-surface structure strongly affect the ground motion during an earthquake. As stated in the introduction, the complex variation of ground motion due to the source and the medium, for a seismic active region, is getting more and more attention and need to be investigated. At the present time, facing that challenge is still afflicted with dearth of the records from observations, especially in the near-source region. Among various technologies, the numerical tools will provide an alternative solution to eliminate the lack of data because of the capability of solving the wave propagation when a 3D medium is present. In the following we will summarize the basic idea developed to solve that task and the results about the near-source ground motion variation achieved in the different chapters of this study. Also we will discuss the deficiencies and limitations in this thesis.

Numerical Green's function method and verification

Due to the cost limitation determined by the numerical tools, scientists are restricted either to few simulations inside a heterogeneous medium, or a satisfying number of simulations inside a homogeneous medium. However a large number of simulations inside a 3D medium are fundamental to quantify the ground motion variation affected by the source and the medium. In order to accomplish that task we introduce the concept of numerical Green's functions (NGF) that can be applied to discretized faults or fault systems, allows the calculation of earthquake scenarios from arbitrary slip histories with 3D medium present. In chapter 3 we describe the theoretical basis for this method, deduce the basic equation used to combine the individual numerical Green's functions to synthesize the ground motion for a certain earthquake. The aim is a systematic study of source related uncertainties/variations of seismic hazard relevant wave field properties (peak ground velocities and peak ground rotation rates) which includes hypocentre location, varying slip distribution (e.g., asperity locations), slip and rupture velocity, etc.. The method for generating quasi-dynamic rupture processes published in [Guatteri et al. \(2004\)](#) is used to produce the necessary source scenarios.

The verification of the method in terms of the misfit introduced by the discretization of the fault plane has to be done before the numerical Green's function data base is build up. In chapter 4, an homogeneous medium is adopted for the first step to investigate how that misfit varies with different parameters. The fault plane of an M7 earthquake (with an assumption of pure-strike slip source mechanism) is discretized into equilateral sub-faults with increasing sizes. Source parameters such as the constant rupture velocity and hypocentre depth are

changed within reasonable range. The cut-off frequency of the filter function used to low-pass the resulting seismograms are also taken into account. Compared to the “continuous” solution, the following trends are found about how the misfit, led by the discretization of the fault plane, changes with the variations of different parameters:

1. High misfits are found behind the rupture propagation where backward directivity plays the main role;
2. At a given point on the surface, the misfit decreases with the increase of the rupture velocity;
3. Deeper hypocentre will lead to smaller, slightly, misfit to the calculated seismic motions;
4. The smaller is the frequency range considered, the smaller is the misfit introduced by the discretization.

For the Newport Inglewood fault system embedded in the Los Angeles basin area, the verification is carried out for a quasi-dynamic source scenario – the same one as adopted for the investigation of the ground motion variation due to the hypocentre location (chapter 6). Referring to the peak ground velocity distribution for the “continuous” solution, discretization with sub-fault of side-length of 1.5 km will introduce 5 percent of peak ground velocity misfit while the one with 1.8 km will introduce 10 percent in maximum over the study area. The velocity waveforms from the discretized solution and the “continuous” solution are quite similar. Thus the sub-fault with of 1.5×1.5 km is adopt as the basic element for the numerical Green’s function calculation.

Earthquakes with specific magnitude 7 are the topics of this study based on the knowledge that this magnitude of earthquake is widely believed to happen in the near future inside this study area. These earthquakes, with different source parameters, are designed and synthesized with the NGF data base. How the ground motions (velocity and rotation rate) vary inside this study area is thoroughly investigated. The answers to the central questions about the ground motion variations are generalized in the following for different kind of ground motion – first we focus on the ground velocity (translational part), then on the ground rotation rate (rotational part) and compare them.

Ground velocity variations: varying hypocentre location

The influence of hypocentre location on the ground motion is investigated by fixing the slip distribution while varying the hypocentre. The hypocentres are assumed to be uniformly distributed (4 in depth direction and 6 in strike direction) inside the seismogenic zone of the southern California. With the static displacement is fixed, quasi-dynamic source scenarios are created with respect to different hypocentres and implemented into the seismic motion synthesization process. The corresponding statistic results (maximum, the ratio between the standard deviation and the mean value of the seismic motions with respect to the different hypocentre locations), indicate complex behavior with dependence of absolute peak ground velocity (PGV) and its variation on asperity location, directivity effect and local structure. From the point of view of the source, changing the hypocentre location, where the rupture starts, affects the ground motions by the widely known effect – the directivity – which leads to narrow (short duration time) but high amplitude impulses in front of the rupture propagation,

but wide (long duration time) impulses with low amplitudes in the regions behind the rupture propagation.

In this study, large variations of ground motion are observed for the fault perpendicular and vertical component of velocity, in the regions off the two tips of the fault trace – where the rupture propagates towards for some (unilateral) scenarios. Inside these regions, the variation (ratio between the standard deviation and the mean value) is found to be about 65% for the fault perpendicular component and 55% percent for the vertical component. For the fault parallel component, the maximum variation over the study area is the largest one (about 73%) at the edge of the basin where the dramatic medium parameter gradient exists. Also large variations are found in the small basin which is located right above the fault trace where the directivity effect is the smallest of the entire study area. At last we conclude that the source and the basin structure play different roles on different components of velocity in terms of variations. The fault parallel component is dominated by the medium while the other two components receive large contributions from the source.

The maximum ground velocity of all the M7 earthquakes is shown for the entire study area. This variable is found to be elevated, obviously, by the sub-surface structure, especially for the fault parallel component. The two horizontal components have apparently larger (3 times) amplitude than the vertical component which is explained by the pure-strike slip source mechanism. In the neighboring regions of the high slip asperity area, the ground motions are elevated.

Finally we investigate how the depth of hypocentre affects the ground motions. The finding is that the hypocentral depth may affect PGV in a positive for the station close to the fault plane, or negative way for the station further from the fault plane and at the edge of the basin. Increasing the hypocentre depth also increases the variations for the station closer to the fault plane while decrease the variations for the station further from the fault plane.

Also, our calculations are compared to those predicted with the empirical tool (the ground motion attenuation with the distance from the fault). The peak acceleration response spectrum at period of 4 sec is adopted. The mean value of our calculations (geometric average of the two horizontal components, or the vertical component) fits well with the empirical prediction over the entire fault distance range of our study area. The near-source saturation of ground motion is also observed.

Ground velocity variations: varying slip history

In the near-source region, the slip history complexity introduces larger variations to the ground motion, too. Because the fault plane is buried under the surface, it is hard to invert the exact rupture process which describes how the fault plane moves during an earthquake. There are different models developed even for a single earthquake with which plenty of records are available. Thus the source complexity effect is the next question to be answered. Benefited from the tool developed by [Guatteri et al. \(2004\)](#), a quasi-dynamic rupture process can be generated instantly which partially incorporates the fault dynamics. As found in chapter 6, varying hypocentre introduces large variations to the ground motion, it is straight forward to fix the hypocentre. 20 slip histories are generated and implemented into the synthesization of ground motion using the numerical Green's functions. The conclusions are summarized in the following.

First, the mean and the maximum value of all 20 different simulations are picked up and used to illustrate the results. In front of the rupture propagation, the directivity effect is

confirmed to take an obvious control over the ground motion production. In the region around the fault tip further from the epicentre, the fault perpendicular component has obviously larger value (mean and maximum) than in the neighboring area. Also it is found to be 1.7 times larger than the fault parallel component whereas for the varying hypocentre case those two horizontal components are compatible in amplitude. As a result, the modulus component of the velocity (length of the vector) is quite similar to the fault perpendicular component in terms of the spatial distribution and absolute value. The fault parallel component and the vertical component receive more contributions from the basin structure.

Secondly, the ratio between the standard deviation and the mean value of all 20 simulations are computed to illustrate the variations due to the source scenario complexity. The biggest variation over the entire study area is found to be the same for the three different components (around 40%). The difference between the different components is the spatial distribution. For the fault perpendicular component (the largest one in terms of absolute value), high variations are found around the epicentre. In the region where high absolute values are found, the variation is quite small compared to the left area. For the fault parallel component, high variations are outlined by the basin edge. In the region surrounding the fault trace, relatively higher variations are located perpendicular to the fault trace and right across the fault trace at the center. For the modulus component, the variations are just the summation of the two horizontal components, high variations are found both around the epicentre and at the basin edge. Compared to the case of the varying hypocentre, the variations are smaller, especially for the fault parallel component.

Rotation rate variation

Some observations prove that the rotational part of ground motion causes damages to buildings during an earthquake. At the same time one instrument has been developed to be capable to record the rotation/rotation rate with sufficient accuracy. The rotation rates are also recorded during the process of building up the numerical Green's function. Thus we can systematically investigate the rotation rate variations in this study area caused by those parameters as discussed in the chapter 6 and chapter 7. The results are summarized in the following.

In the region surrounding the fault trace, the vertical component of rotation rates are 5 times larger than the other two horizontal components both for the case of varying hypocentre and slip history. Across the fault trace, extremely high gradient of rotation rates are found, especially for the vertical component. The pure-strike slip source mechanism dominates the ground rotation rates in this region. The absolute value is around the magnitude of 10^{-3} rad/s which is same to the one calculated by [Bouchon and Aki \(1982\)](#).

For the varying hypocentre case, the fault perpendicular and the vertical rotation rates have higher values (of all 24 simulations) at the fault tip near a sharp medium change area (left tip) than the other tip. Considering that a high slip asperity is close to the left tip of the fault trace, too, the elevation is explained by both the medium and the high slip asperity. These two amplifiers have no obvious effect on the fault parallel component which is dominated by the directivity effect. The medium amplification is also observed in terms of the variation (ratio between the standard deviation and the mean value of all 24 simulations). The largest variations (more than 70% for the fault perpendicular and the vertical component) are also located at the edge of the basin. In the regions where high absolute rotation rates are observed (normally the region surrounding the fault trace), the variations are small (no more than 20%).

For the varying slip history case, directivity effect is more obviously observed for the fault

parallel component (for the translational motion it is the fault perpendicular component). Smaller variations (between 40 to 50 in percentage) are observed than the case of the varying hypocentre, but compatible to the accelerations. Compared with the acceleration, the variations for the rotation rates are affected more strongly by the basin and thus normally higher variations are observed inside the basin than in the case of accelerations for all three components.

Comparison: acceleration and rotation rate

The rotation rates are compared to the accelerations as has been done for the global scale (Igel et al., 2005). The varying hypocentre case is taken as the first example. The waveform similarity (horizontal acceleration and vertical rotation rate) along a few profiles for one earthquake supports us to investigate the waveform similarity over the entire study area. The fault parallel components of accelerations are quite similar to the vertical rotation rate at those stations which is perpendicular to the fault trace. This similarity decreases with the increase of the angle between the station and the rupture propagation direction. The fault perpendicular component of accelerations are quite similar to the vertical rotation rates at those stations with small angles to the rupture propagation direction. To sum up, the high waveform similarity regions of the two horizontal accelerations cover the entire study area. The amplitude ratios between the horizontal accelerations and the vertical rotation rate are calculated over the entire study area and related to the medium property. The aim is to find out what the joint processing of the accelerations and the rotation rates can reveal. In our case, except for the very small region surrounding the fault trace, this amplitude ratio (mean value of horizontal accelerations and the vertical rotation rate) does have a strong relationship with the medium parameters.

The vertical rotation rates are plotted out as a function of the fault distance and compared to the accelerations. The basic trend about the attenuation of the rotation rate with the fault distance is quite similar to that of the accelerations. The standard deviations are also equivalent to those of the accelerations over the entire distance range. We conclude that the rotation rates will attenuate, with the distance term, in the same way as the accelerations.

Outlook

This study is subject to severe limitations. Amongst others, (1) the fault is approximated by a vertical plane and strike-slip source mechanism. (2) The lowest shear-velocity (1.4 km/s) is too high to be useful for realistic hazard estimates and the highest frequencies are only relevant for very tall buildings, bridges, etc.. (3) We limited ourselves to investigate only one M7 earthquake happening on the same fault. Yet, the main purpose of this study is to illustrate the potential functionalities of an NGF data base and the possibilities to systematically investigate source related uncertainties in 3D areas with high seismic hazard. Source related uncertainty in 3D media is an issue that has so far not been addressed properly, partly due to limitations of computational resources. It is important to note that such NGF data bases only make sense if the crustal structure is sufficiently well known, moreover that the NGFs would need to be recalculated with every model update (it might be possible to devise approximate updates of the NGFs). Nevertheless, we suggest that this methodology may be useful also on a larger scale particularly for mega-faults in subduction zones with tsunami-generating potential.

Appendix A

Peak Ground Motions: Varying Hypocentre

All the 24 peak ground motions distributions (according to the varying hypocentre case described in chapter 6) are summarized in this appendix for the three components. The first three figures concern the peak ground velocity. The second three figures show the results of the peak ground rotation rate. Epicentre is represented with the red asterisk. Curved white lines mark the iso-surface of the shear wave velocity at 2.0 km/s. Dashed black rectangles represent the fault trace. Hypocentre coordinates, corresponding to the top left corner of the fault plane, are represented with the numbers shown at the center of each peak ground velocity distribution, respectively. The setup about the source scenarios and the medium are referred to chapter 6.

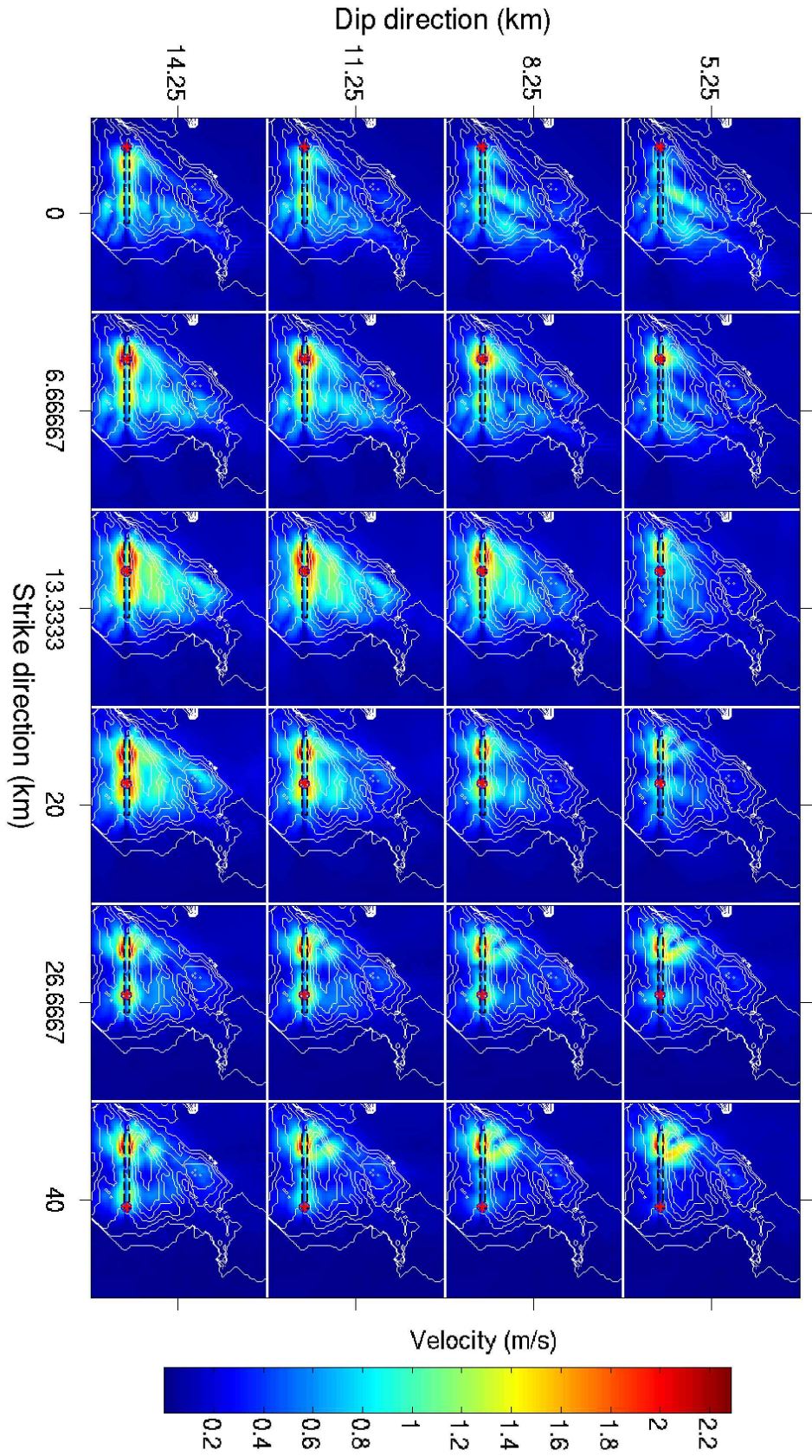


Figure A.1: Peak Ground Velocity distributions for the varying hypocentre: *x*-component.

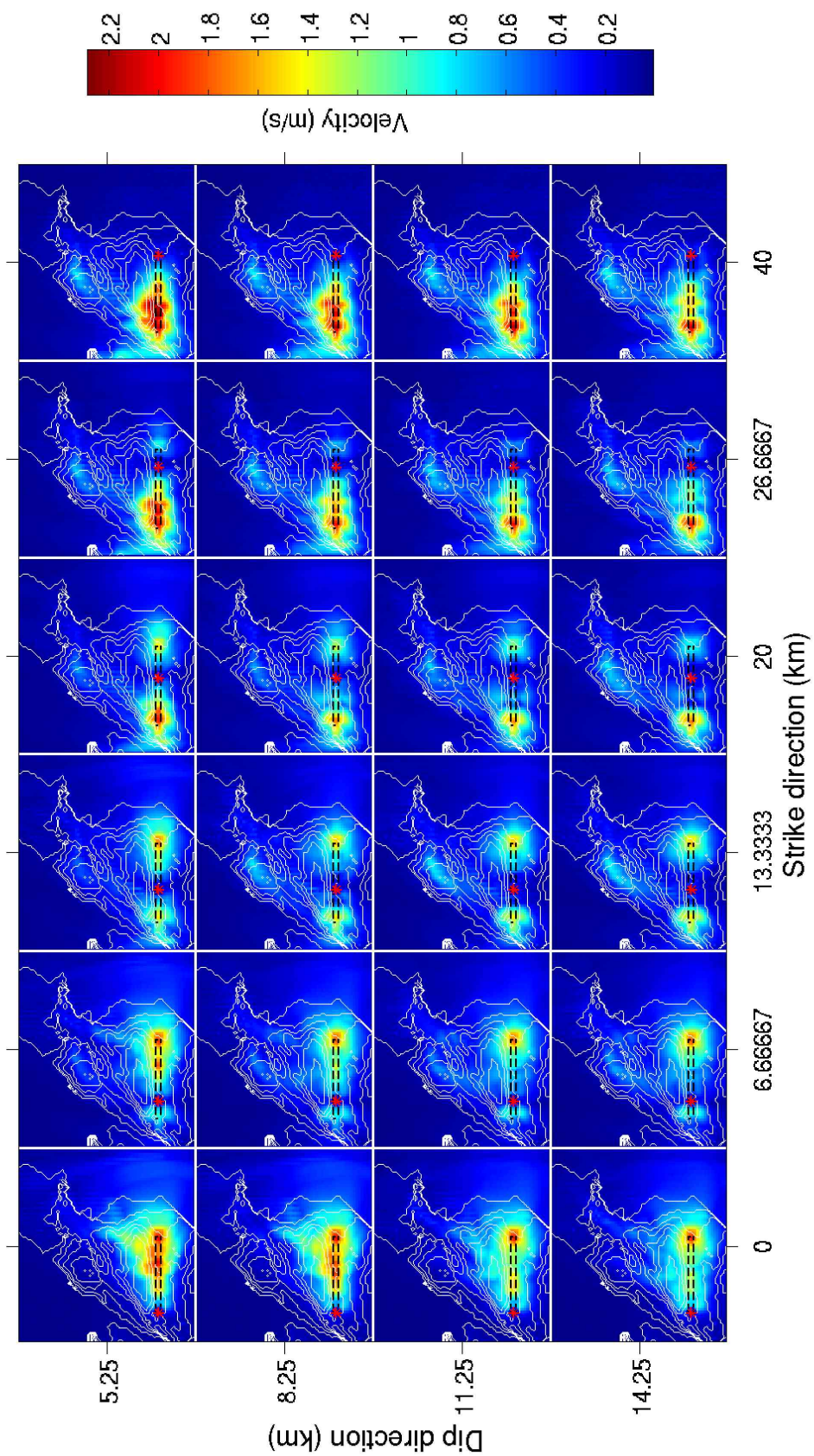


Figure A.2: Peak Ground Velocity distributions for the varying hypocentre: y -component.

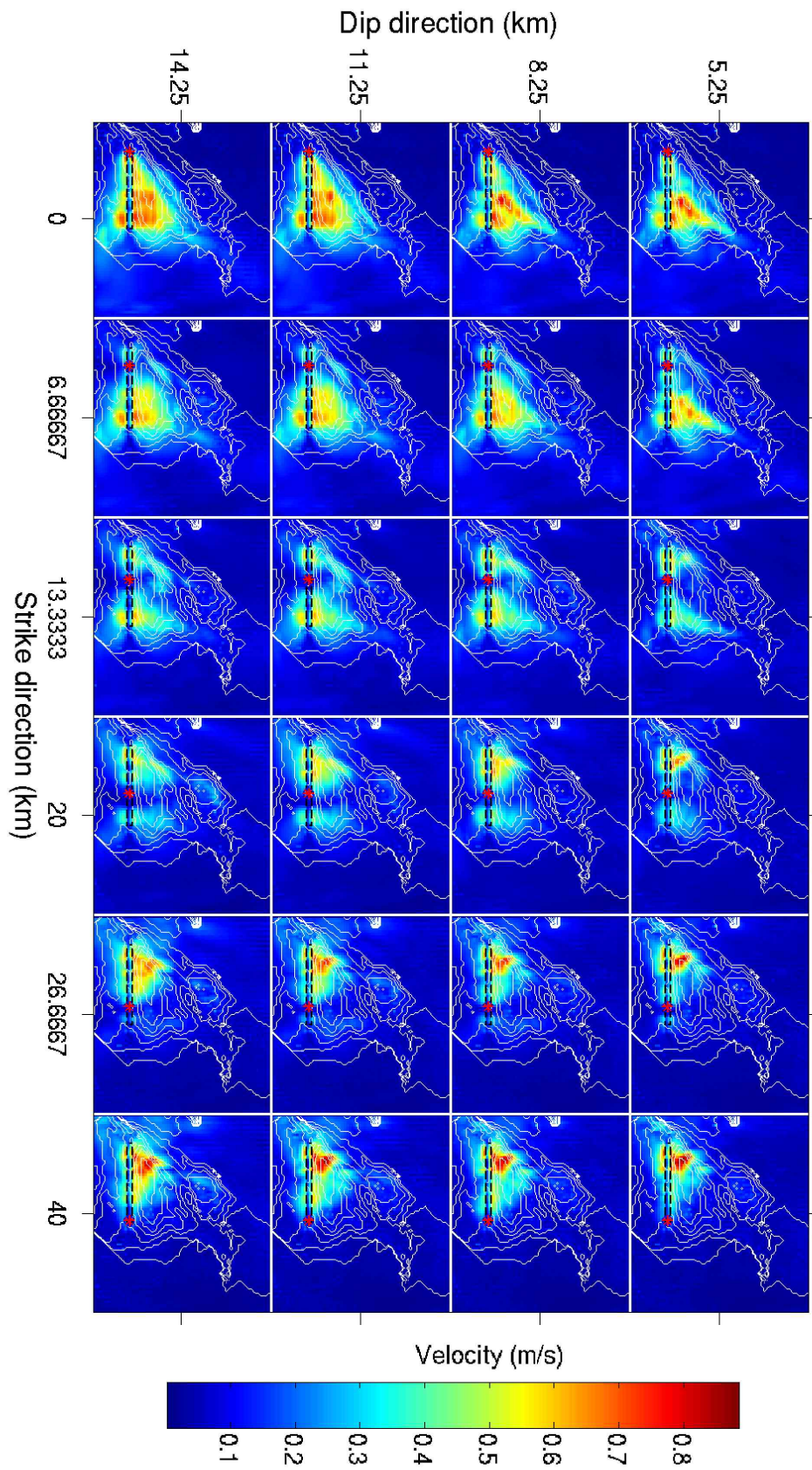


Figure A.3: Peak Ground Velocity distributions for the varying hypocentre: z-component.

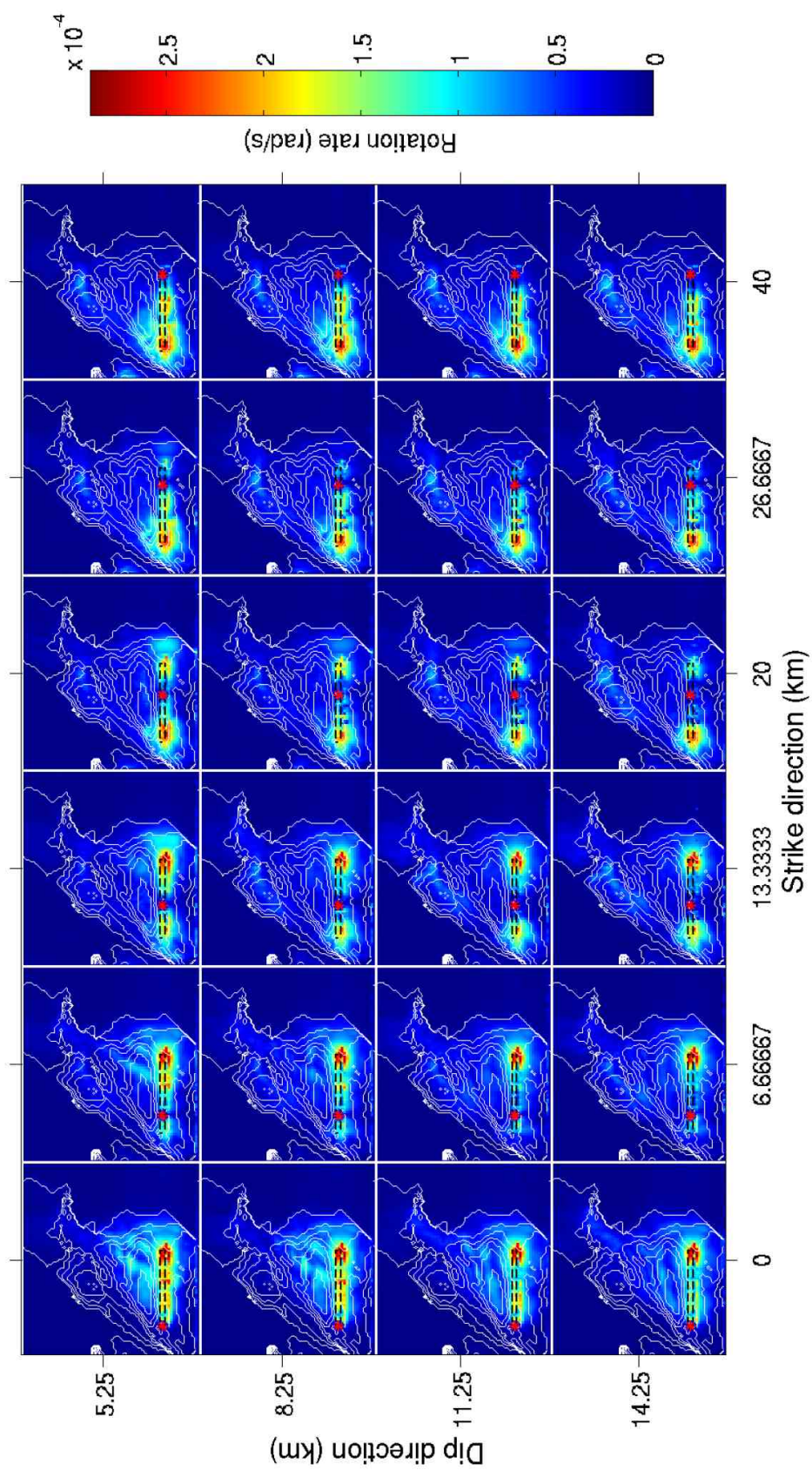


Figure A.4: Peak Ground Rotation Rate distributions for the varying hypocentre: *x*-component.

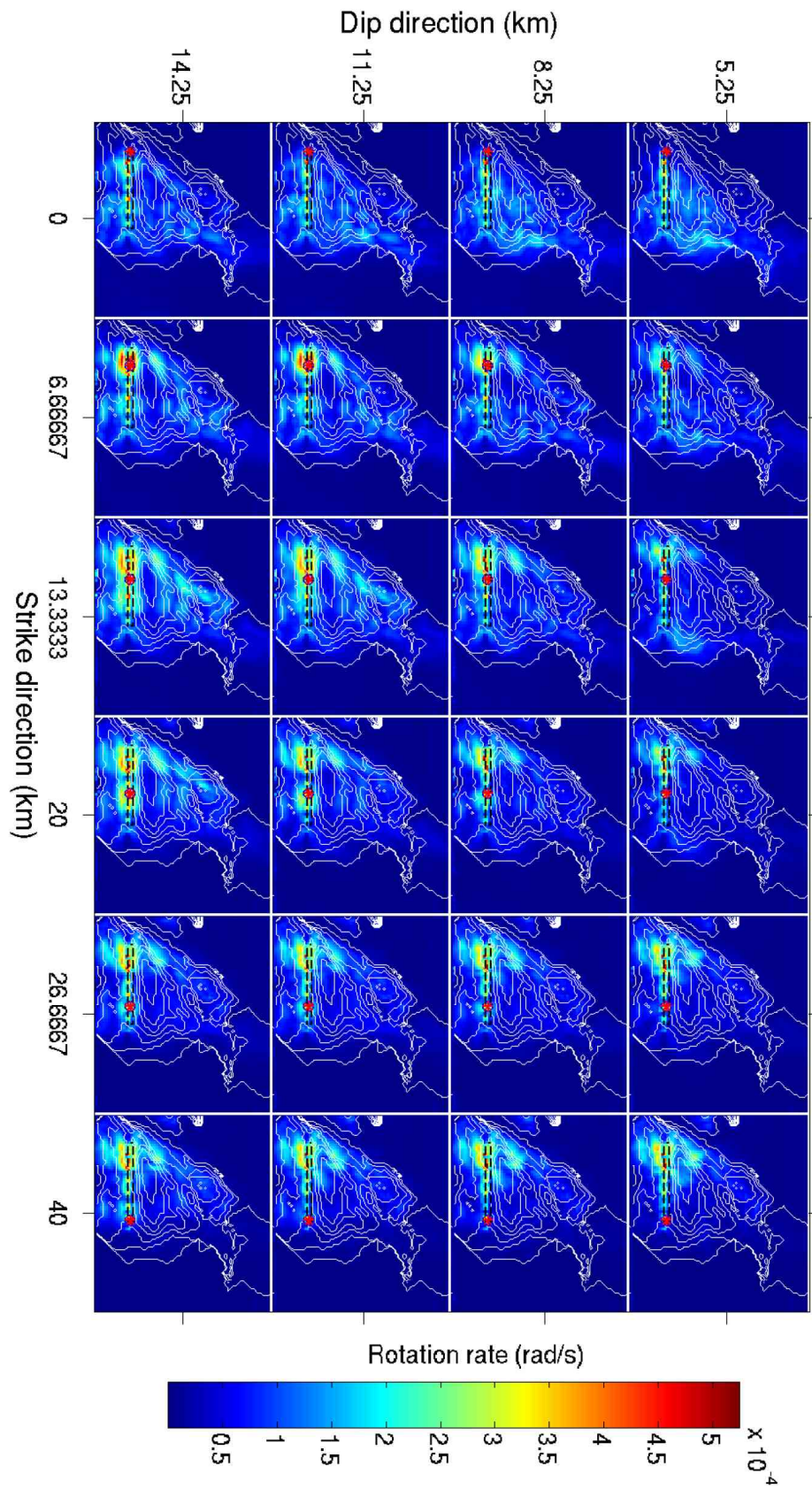


Figure A.5: Peak Ground Rotation Rate distributions for the varying hypocentre: y -component.

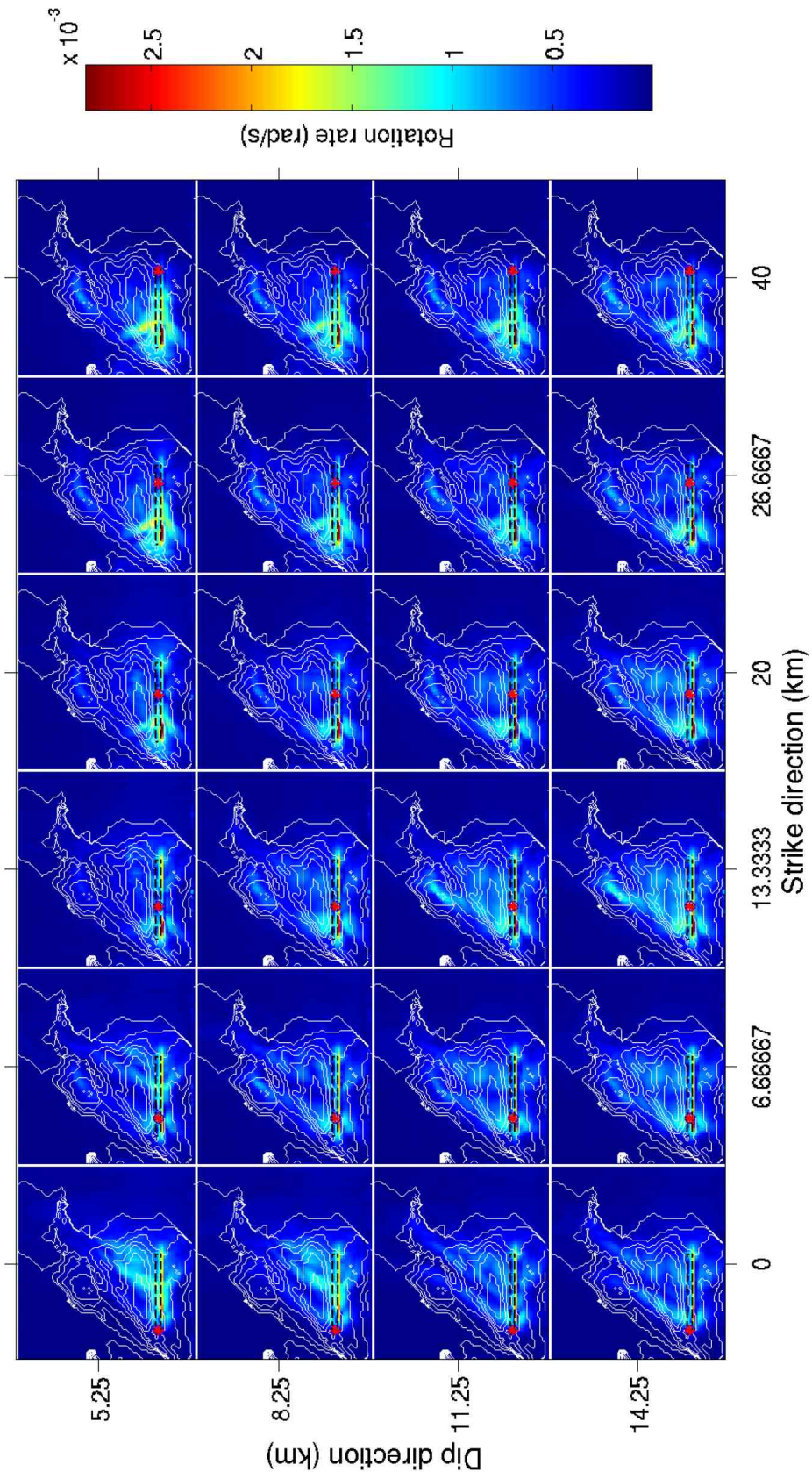


Figure A.6: Peak Ground Rotation Rate distributions for the varying hypocentre: z -component.

Appendix B

Peak Ground Motions: Varying Slip History

The peak ground motions simulated with the varying slip histories are shown in this appendix. In total, 20 peak ground motions are summarized into one figure according to different slip scenario adopted. The first three figures concern the peak ground velocity (PGV) and the second three the peak ground rotation rate (PGRR). The number in the white rectangle represents the slip scenario adopted (Fig. 7.1). Epicentre is marked with the red asterisk. Curved white lines mark the iso-surface of the shear wave velocity at 2.0 km/s. Dashed black rectangles represent the fault trace.

Other informations can be found in chapter 7.

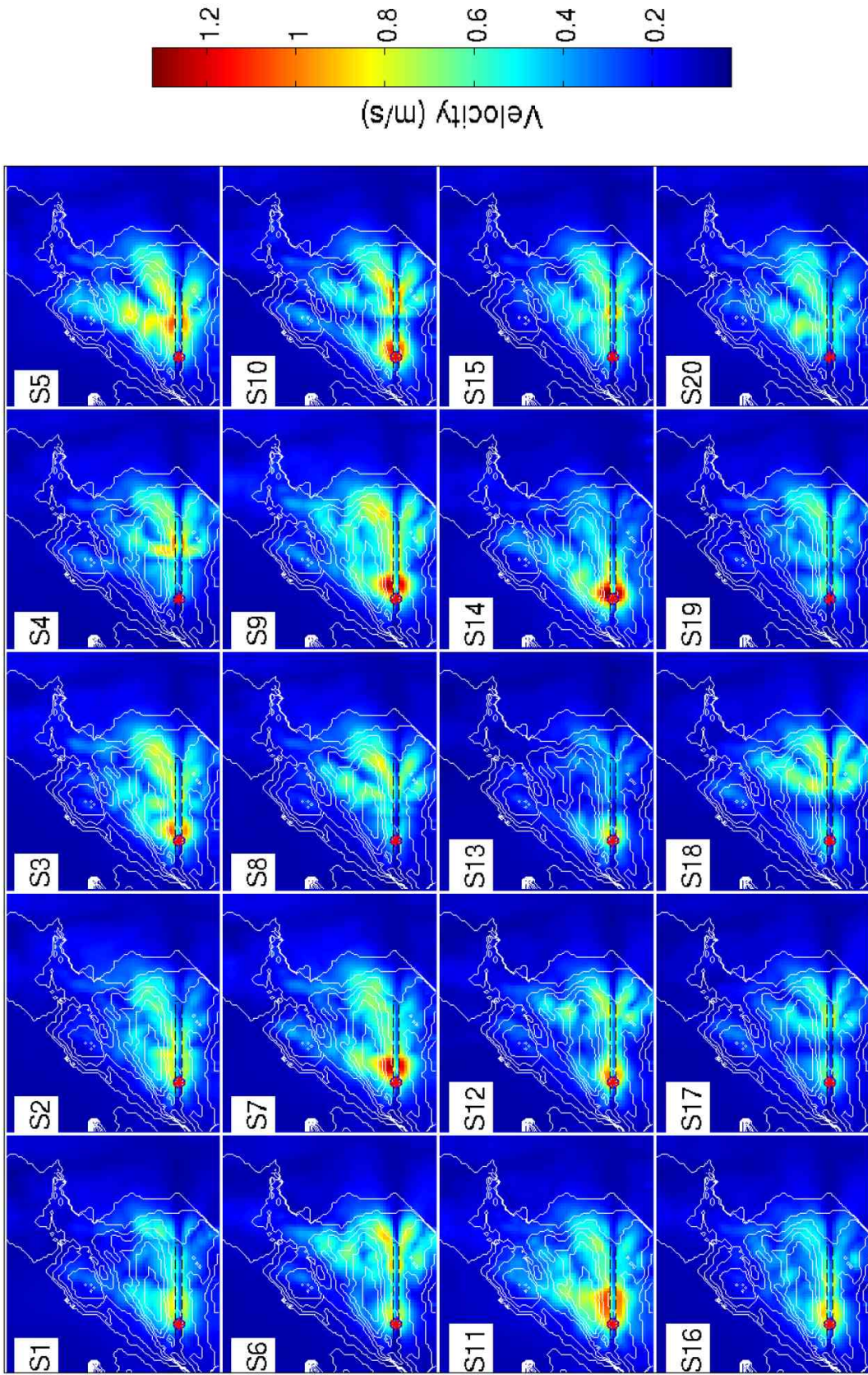


Figure B.1: Peak Ground Velocity distributions for the varying slip history: x -component.

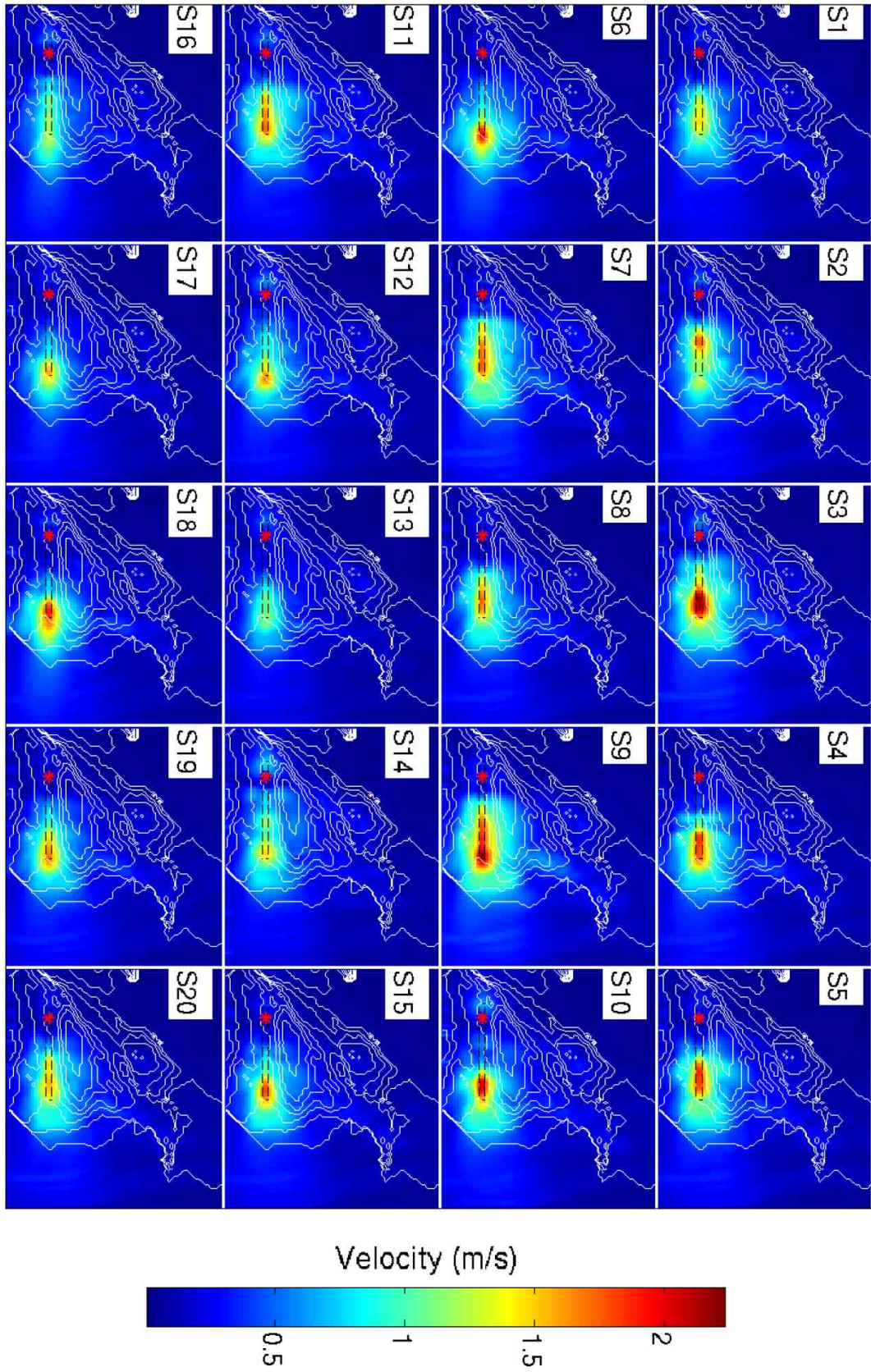


Figure B.2: Peak Ground Velocity distributions for the varying slip history: y -component.

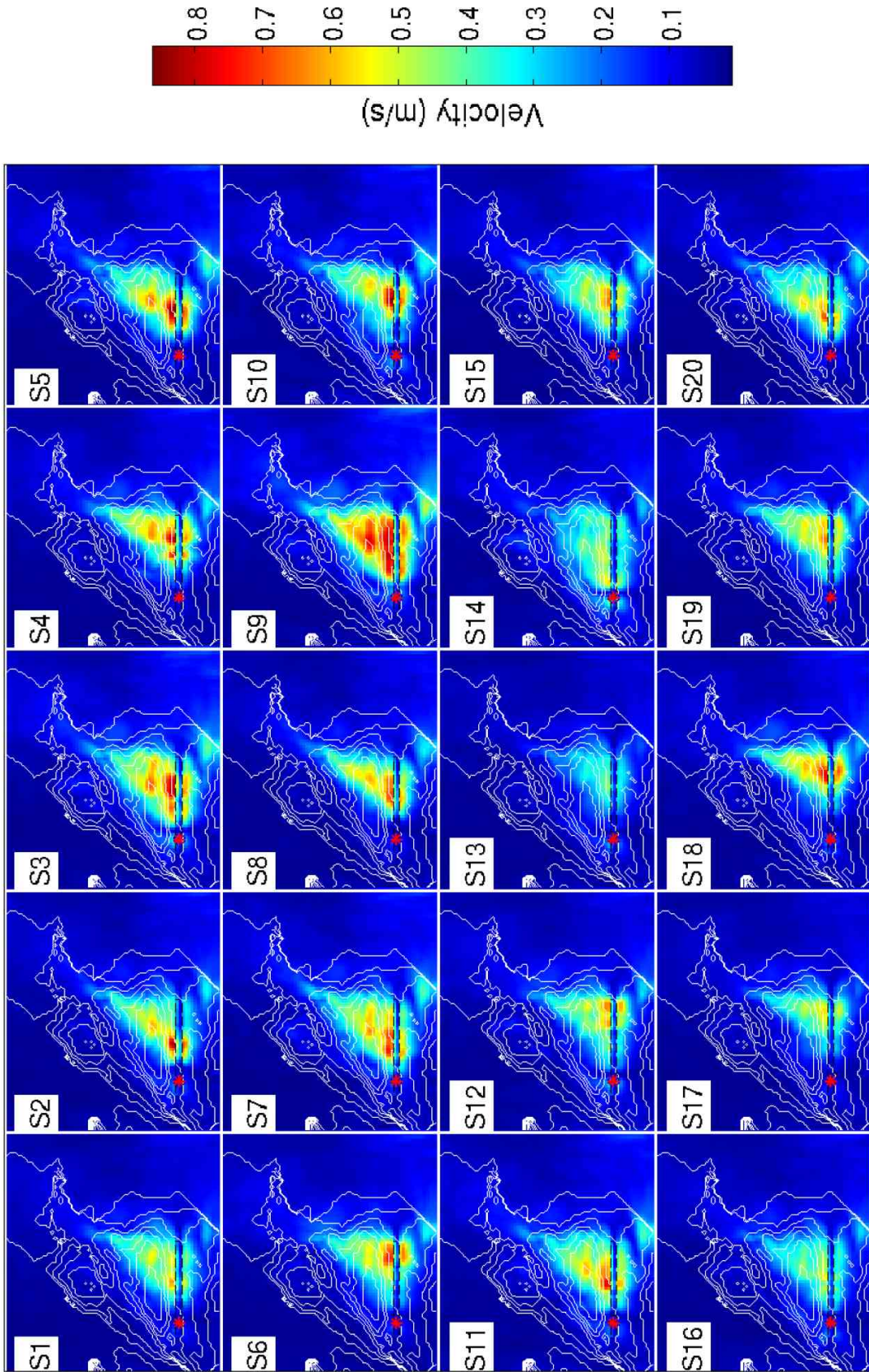


Figure B.3: Peak Ground Velocity distributions for the varying slip history: z -component.

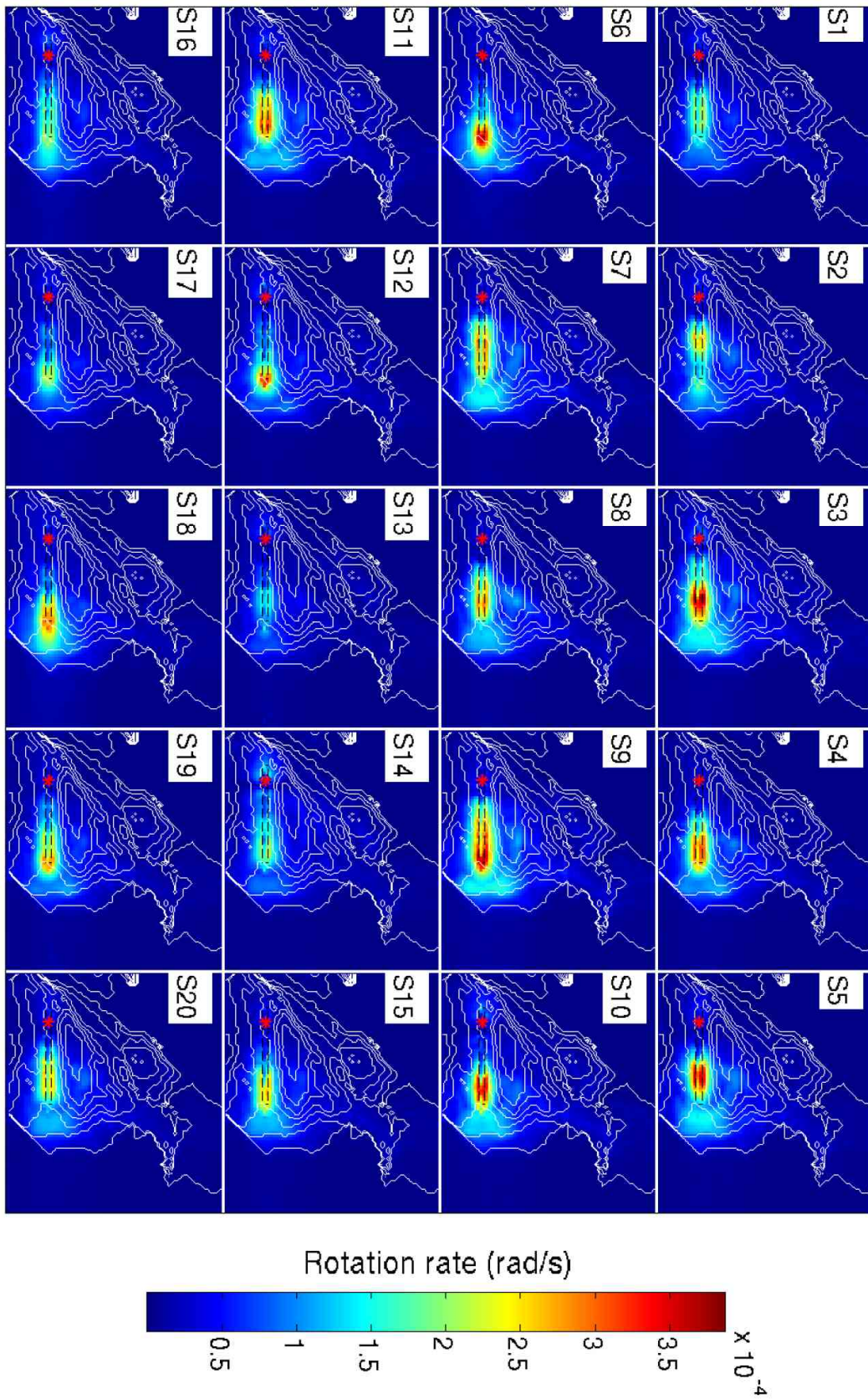


Figure B.4: Peak Ground Rotation Rate distributions for the varying slip history: x -component.

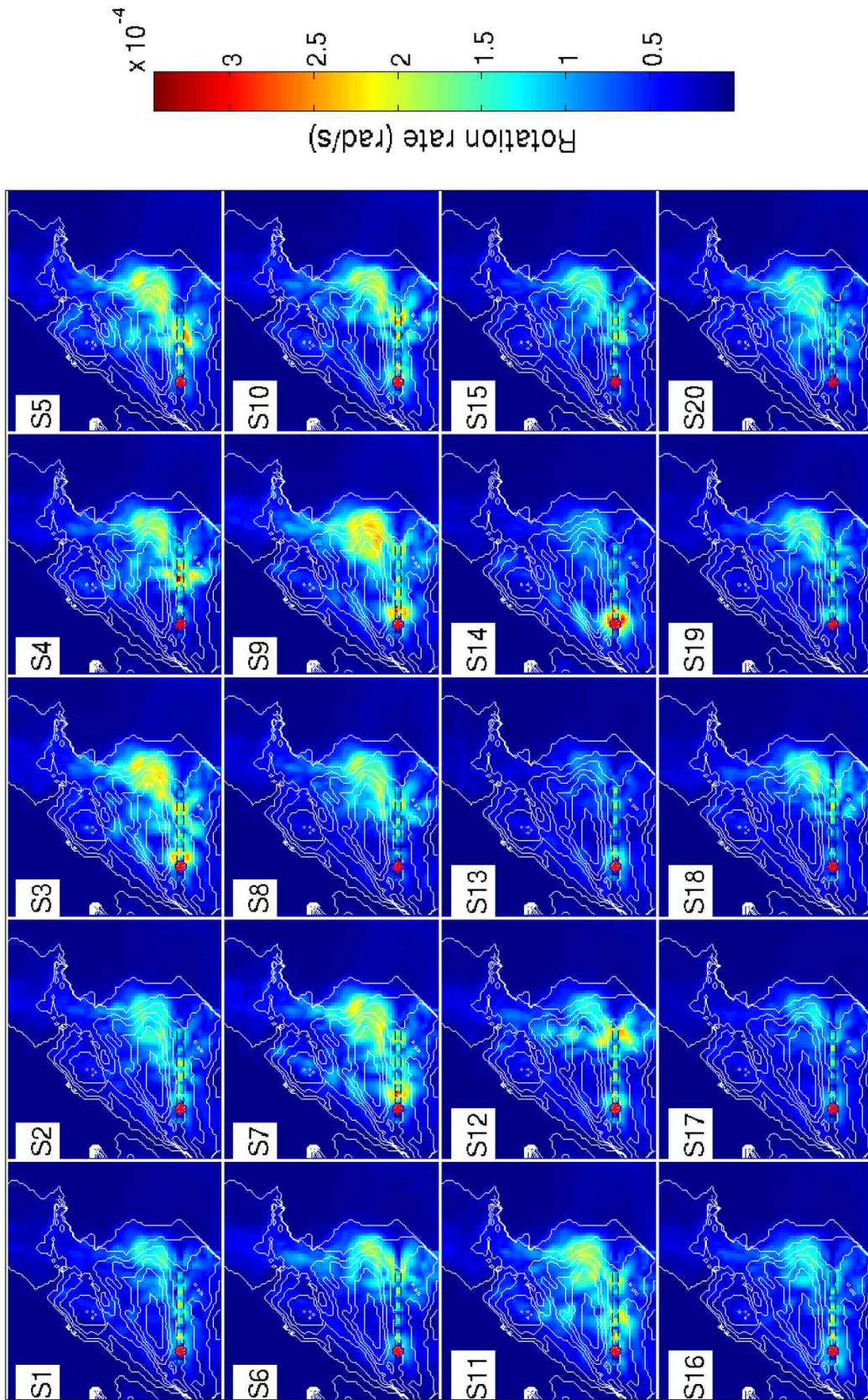


Figure B.5: Peak Ground Rotation Rate distributions for the varying slip history: y -component.

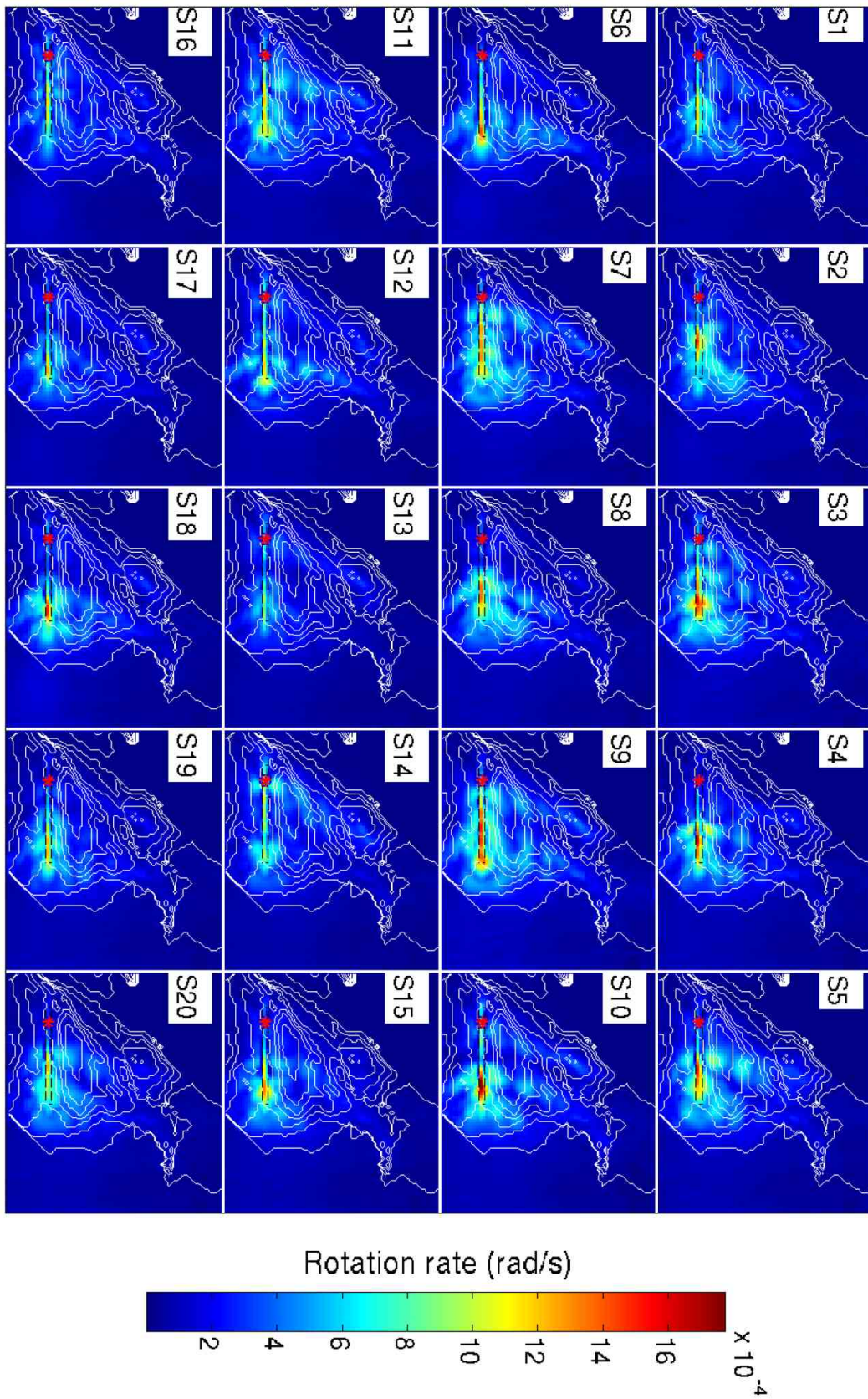


Figure B.6: Peak Ground Rotation Rate distributions for the varying slip history: z-component.

List of Tables

4.1	for the homogeneous case	22
5.1	Verification setup for the heterogeneous model in the Los Angeles basin	36
6.1	Depth for aftershocks	45
6.2	Coefficients and Statistical Parameters for the PSA attenuation relationship	56

List of Figures

2.1	Procedure for generating the quasi-dynamic rupture	12
2.2	Slip rate function adopted in the quasi-dynamic process	13
3.1	Schematic illustration of the Numerical Green's Function method	19
4.1	Study area for the verification of the hypothetical homogeneous medium	22
4.2	Schematic set-up for the homogeneous case	22
4.3	Fault plane discretization with sub-fault of different sizes	22
4.4	Source time function adopted	23
4.5	Final slip distribution for the benchmarking	24
4.6	Velocity profiles from two discretized solutions	25
4.7	Fourier amplitude spectra from different solutions	26
4.8	Hypocentre depth effect on the ground motion accuracy	27
4.9	Rupture velocity effect on the ground motion accuracy	28
4.10	Cut-off frequency effect on the ground motion accuracy	29
5.1	Los Angeles area, modeled region and the idealized Newport-Inglewood fault . .	34
5.2	Depth of shear wave velocity isosurface at 2.0 km/s	34
5.3	Newport Inglewood fault plane	35
5.4	Optimal sub-fault size determination for an M7 earthquake	37
5.5	Numerical Green's function calculation setting up	38
5.6	Verification of the optimal sub-fault size for an M7 earthquake in terms of acceleration	38
5.7	Cartesian and spherical polar coordinates for analysis of radial and transverse components of displacement radiated by a shear dislocation of area A and av- erage slip \mathbf{u} (Aki and Richards, 2002).	39
5.8	Radiation pattern: radial component of displacement	40
5.9	SH wave displacement radiation pattern	40
5.10	Velocity histories of Rinaldi ground motion and El Centro ground motion . . .	41
5.11	Radiation pattern: static rotation	42
6.1	Final slip distribution of an M7 earthquake on NI fault and hypocentre grid . .	46
6.2	Velocity snapshots of y -component	47
6.3	PGV distributions for two example hypocentres	48
6.4	Fault parallel velocity profile for two example hypocentres	49
6.5	Fault perpendicular velocity profile for two example hypocentres	50
6.6	Statistics of the PGV distributions due to varying hypocentres	51

6.7	Statistics of the PGV distributions due to varying hypocentres: modulus component	53
6.8	Hypocentre depth effect illustration	54
6.9	Acceleration amplitude spectra examples	55
6.10	Comparison with empirical results in terms of acceleration response spectrum	57
7.1	Numbered slip histories used in the simulations	61
7.2	Mean value of PGV distributions from 20 different slip histories	62
7.3	PGV distributions for a few example slips	64
7.4	PGV – maximum, standard deviation and the variation	65
8.1	Effect of sub-fault size on rotation rate	71
8.2	PGRR distributions for two example hypocentres	73
8.3	Rotation rate profile for the two example hypocentres: parallel to the fault trace	74
8.4	Rotation rate profile for the two example hypocentres: perpendicular to fault trace	75
8.5	Properties of the PGRR distributions due to varying hypocentre	76
8.6	Maximum value of peak rotation rate in the near-source region	78
8.7	Rotation rate profile: parallel to y -axis	79
8.8	Hypocentre depth effect on rotation rate	80
8.9	Mean values of peak ground rotation rates from 20 different slip histories	81
8.10	Peak ground rotation rate distributions from four slip models	83
8.11	Peak Ground Rotation Rate variation due to slip histories	84
8.12	Acceleration (x -component) and rotation rate (z -component) profiles	86
8.13	Acceleration (y -component) and rotation rate (z -component) profiles	87
8.14	Similarity between the waveform of the horizontal accelerations and the vertical rotation rate for one example hypocentre	89
8.15	Ratio between peak acceleration and peak rotation rate	90
8.16	Peak Ground Acceleration variation due to varying hypocentre location	91
8.17	Peak Ground Acceleration variation due to varying slip history	93
8.18	Peak ground acceleration and peak ground rotation rate as a function of the fault distance	95
A.1	PGVs for the varying hypocentre: x -component	104
A.2	PGVs for the varying hypocentre: y -component	105
A.3	PGVs for the varying hypocentre: z -component	106
A.4	PGRRs for the varying hypocentre: x -component	107
A.5	PGRRs for the varying hypocentre: y -component	108
A.6	PGRRs for the varying hypocentre: z -component	109
B.1	PGVs for the varying slip history: x -component	111
B.2	PGVs for the varying slip history: y -component	112
B.3	PGVs for the varying slip history: z -component	113
B.4	PGRRs for the varying slip history: x -component	114
B.5	PGRRs for the varying slip history: y -component	115
B.6	PGRRs for the varying slip history: z -component	116

Bibliography

- Abrahamson, N. A. and W. J. Silva, 1997: Empirical response spectral attenuation relations for shallow crustal earthquakes. *Seismological Research Letters*, **68**, 94–127.
- Aki, K., 1967: Scaling law of seismic spectrum. *Geophys. Res. Lett.*, **72**, 1217–1231.
- Aki, K. and P. G. Richards, 2002: *Quantitative Seismology: theory and methods*, 2nd. University Science Books.
- Anderson, J. G., 2003: *International Handbook of Earthquake and Engineering Seismology*. Volume 81B, Chapter 57, ISBN: 0-12-440658-0, ACADEMIC PRESS.
- Anderson, J. G. and J. E. Luco, 1983a: Parametric study of near-field ground motion for a strike slip dislocation model. *Bull. Seism. Soc. Am.*, **73**, 23–43.
- Anderson, J. G. and J. E. Luco, 1983b: Parametric study of near field ground motions for oblique-slip and dip-slip dislocation models. *Bull. Seism. Soc. Am.*, **73**, 45–57.
- Andrews, D., 1976: Rupture propagation with finite stress in antiplane strain. *Journal of Geophysical Research*, **81**, 3575–3582.
- Andrews, D. J., 1980: A stochastic fault model, I. Static case. *Journal of Geophysical Research*, **85**, 3867–3877.
- Archuleta, R. J., 1984: A faulting model for the 1979 Imperial Valley earthquake. *Journal of Geophysical Research*, **89**, 4559–4585.
- Archuleta, R. J. and S. H. Hartzell, 1981: Effects on fault finiteness on near-source ground motion. *Bull. Seism. Soc. Am.*, **71**, 939–957.
- Atkinson, G. M. and I. A. Beresnev, 1998: Compatible ground-motion time histories for new national seismic hazard maps. *Canadian J. civil Eng.*, **25**, 305–318.
- Atkinson, G. M. and D. M. Boore, 1997: Stochastic point-source modeling of ground motions in the Cascadian region. *Bull. Seism. Soc. Am.*, **68**, 74–85.
- Atwater, T., 1989: Plate tectonic history of the northeast pacific and western North America, in *The eastern Pacific ocean and hawaii*, edited by Winterer, E. L., D. M. Hussong, and R. W. Decker. *The Geological Society of America*.
- Barrows, A. G., 1974: A review of the geology and earthquake history of the Newport-Inglewood structural zone, southern California: California Division of Mines and Geology Special Report.

- Bennett, R. A., R. E. Reilinger, W. L. Rodi, Y. Li, M. N. Toksoz, and K. W. Hudnut, 1995: Coseismic fault slip associated with the 1992 Mw = 6.1 Joshua Tree, California, earthquake: Implications for the Joshua Tree - Landers earthquake sequence. *Journal of Geophysical Research*, **100**, 6443 – 6461.
- Beresnev, I. A. and G. M. Atkinson, 1997: Modeling finite-fault radiation from the ω^n spectrum. *Bull. Seism. Soc. Am.*, **87**, 67–84.
- Beresnev, I. A., G. M. Atkinson, P. A. Johnson, and E. H. Field, 1998: Stochastic finite-fault modeling of ground motions from the 1994 Northridge, California, earthquake. ii. widespread nonlinear response at soil sites. *Bull. Seism. Soc. Am.*, **88**, 1402–1410.
- Beroza, G. C. and P. Spudich, 1988: Linearized inversion for fault rupture behavior: Application to the 1984 Morgan Hill, California, earthquake. *Journal of Geophysical Research*, **93**, 6275 – 6296.
- Bird, P. and R. W. Rosenstock, 1984: Kinematics of present crust and mantle flow in southern California. *Bull. Seism. Soc. Am.*, **95**, 946–957.
- Bolt, B. A. and N. A. Abrahamson, 1982: New attenuation relations for peak and expected accelerations of strong ground motion. *Bull. Seism. Soc. Am.*, **72**, 2307–2322.
- Boore, D. M., 1983: Stochastic simulation of high-frequency ground motions based on seismological models of the radiated spectra. *Bull. Seism. Soc. Am.*, **73**, 1865–1894.
- Boore, D. M., 1986: Short period *P*- and *S*-wave radiation from large earthquakes: implications for spectral scaling relations. *Bull. Seism. Soc. Am.*, **76**, 43–64.
- Boore, D. M., 1996: SMSIM-fortran programs for simulating ground motions from earthquakes: version 1.0. *U.S. Geol. surv. Open-file Rept.*
- Boore, D. M., 2003: Simulation of ground motion using the stochastic method. *Pure and Applied Geophysics*, **160**(3 4), 635–676.
- Boore, D. M. and G. Atkinson, 1987: Stochastic prediction of ground motion and spectral response parameters at hard-rock sites in Eastern North America. *Bull. Seism. Soc. Am.*, **77**, 440–467.
- Boore, D. M. and W. B. Joyner, 1984: A note on the use of random vibration theory to predict peak amplitudes of transient signals.
- Boore, D. M., W. B. Joyner, and T. E. Fumal, 1997: Equations for estimating horizontal response spectra and peak acceleration from western North American earthquakes: A summary of recent work. *Seismological Research Letters*, **68**, 128–153.
- Boratyński, W. and R. Teisseyre, 2004: Generalized continuum with defects and asymmetric stresses. *Acta Geophys Pol*, **52**, 185–195.
- Bouchon, M. and K. Aki, 1982: Strain, tilt, and rotation associated with strong ground motion in the vicinity of earthquake faults. *Bull. Seism. Soc. Am.*, **72**, 1717–1738.

- Bouchon, M., M. N. Toksoz, H. Karabulut, M. P. Bouin, M. Dietrich, M. Aktar, and et M. Edie, 2000: Seismic imaging of the 1999 izmit (turkey) rupture inferred from near-fault recordings. *Geophys. Res. Lett.*, **27**, 3013 – 3016.
- Bour, M. and M. Cara, 1997: Test of a simple Empirical Green's function method on moderate-sized earthquakes. *Bull. Seism. Soc. Am.*, **87**, 668–683.
- Brune, J. N., 1970: Tectonic stress and the spectra of seismic shear waves from earthquakes. *Journal of Geophysical Research*, **75**, 4997–5010.
- Campbell, K. W., 1981: Near-source attenuation of peak horizontal acceleration. *Bull. Seism. Soc. Am.*, **71**, 2039–2070.
- Campbell, K. W., 1997: Empirical near-source attenuation relationships for horizontal and vertical components of peak ground acceleration, peak ground velocity, and pseudo-absolute acceleration response spectra. *Seismological Research Letters*, **68**, 154–179.
- Campbell, K. W. and Y. Bozorgnia, 2003: Updated near-source ground-motion (attenuation) relations for the horizontal and vertical components of peak ground acceleration and acceleration response spectra. *Bull. Seism. Soc. Am.*, **93**, 314–331.
- Campbell, K. W. and C. M. Duke, 1974: Bedrock intensity attenuation and site factors from San Fernando earthquake records. *Bull. Seism. Soc. Am.*, **64**, 173–185.
- Campbell, R. H. and R. F. Yerkes, 1976: Cenozoic evolution of the Los Angeles basin area Relation to plate tectonics, in *Aspects of the Geologic History of the California Continental Borderland, Misc. publ. 24*, edited by D. G. Howell, Pacific Section, American Association of petroleum Geologists, Los Angeles, Calif.
- Carcione, J. M. and H. B. Helle, 1999: Numerical solution of the poroviscoelastic wave equation on a staggered mesh. *J. comput. Phys.*, **154**, 520–527.
- Cerjan, C., D. Kosloff, R. Kosloff, and M. Reshef, 1985: A nonreflecting boundary condition for discrete acoustic wave and elastic-wave equation. *Geophysics*, **50**, 705–708.
- Cheng, A., D. D. Jackson, and M. Matsu'ura, 1987: Aseismic crustal deformation in the Transverse Ranges of southern California. *Tectonophysics*, **144**, 159–180.
- Chew, W. and Q. Liu, 1996: Perfectly matched layers for elastodynamics: a new absorbing boundary condition. *Journal of Computational Acoustics*, **4**(4), 341–359.
- Chiou, B. S. J., C. Roblee, N. Abrahamson, and M. S. Power, 2004: The Research Program of "Next Generation of Ground-Motion Attenuation Models" . *Geotechnical Engineering for Transportation Projects, Proceedings of Geo-Trans 2004, July 27-31, 2004, Los Angeles, CA*, **2**, 768–777.
- Cline, M. W., R. A. Snay, and E. L. Timmerman, 1984: Regional deformation of the earth model for the Los Angeles Region, California. *Tectonophysics*, **107**, 10,279–10,314.
- Cochard, A., H. Igel, A. Flaws, B. Schuberth, J. Wassermann, and W. Suryanto, 2006: Rotational motions in seismology, in: *Earthquake source asymmetry, structural media and rotation effects*, Teisseyre *et al.*, eds., Springer Verlag, in press, 2006.

- Collino, F. and C. Tsogka, 2001: Application of the PML absorbing layer model to the linear elastodynamic problem in anisotropic heterogeneous media. *Geophysics*, **66**, 294–307.
- Das, S. and B. V. Kostrov, 1987: On the numerical boundary integral equation method for three-dimensional dynamic shear crack problems. *Jour. Appl. Mech.*, **54**, 99–104.
- Davis, T. L., J. Namson, and R. F. Yerkes, 1989: A cross-section of the Los Angeles area: seismically active fold and thrust belt, the 1987 Whittier Narrows earthquake, and earthquake hazard. *Journal of Geophysical Research*, **94**, 9644–9664.
- Day, S., 1982: Three-dimensional simulation of spontaneous rupture: the effect of nonuniform prestress. *Bull. Seism. Soc. Am.*, **72**, 1881–1902.
- Dolan, J. F., K. Sieh, T. K. Rockwell, R. S. Yeats, J. Shaw, J. Suppe, G. J. Huftile, and E. M. Gath, 1995: Prospects for larger or more frequent earthquakes in the Los Angeles metropolitan region. *Nature*, **267**, 199–205.
- Donnellan, A., B. H. Hager, R. W. King, and T. A. Herring, 1993: Geodetic measurement of deformation in the Ventura basin region, southern California. *Journal of Geophysical Research*, **98**, 21,727–21,739.
- Duke, C. M., J. E. Luco, A. R. Carriveau, P. J. Hradilek, R. Lastrico, and D. Ostrom, 1970: Strong earthquake motion and site conditions: Hollywood. *Bull. Seism. Soc. Am.*, **60**, 1271–1289.
- Emerman, S. H., W. Schmidt, and R. A. Stephen, 1982: An implicit finite-difference formulation of the elastic wave equation. *Geophysics*, **53**, 625–637.
- Espinosa, A. F., 1980: Attenuation of strong horizontal ground accelerations in the Western United States and their relation to M_L . *Bull. Seism. Soc. Am.*, **70**, 583–616.
- Esteva, L., 1970: Seismic risk and seismic design. In: *Seismic Design for Nuclear Power Plants*, ed. R. Hansen, MIT Press, Cambridge.
- Ewald, M., H. Igel, H. K. G., and F. Scherbaum, 2006: Basin-related effects on ground motion for earthquake scenarios in the lower rhine embayment. *Geophys. J. Int.*, **166**, 197–212.
- Feigl, K. L., D. C. Agnew, Y. Bock, D. Dong, A. Donnellan, B. H. Hager, T. A. Herring, D. D. Jackson, T. H. Jordan, R. W. King, S. Larsen, K. M. Larson, M. H. Murray, Z. Shen, and F. H. Webb, 1993: Measurement of the velocity field of central and southern California. *Journal of Geophysical Research*, **98**, 21,677–21,712.
- Fischer, P. J. and G. I. Mills, 1991: The offshore Newport–Inglewood–Rose Canyon fault zone, California: structure, segmentation and tectonics, in *Environmental Perils San Diego Region*, P. L. Abbott and W. J. Elliot (Editors), San Diego Association of Geologists, San Diego, Geological Society of America Annual Meeting.
- Frankel, A., 1995: Simulating strong motions of large earthquake using recordings of small earthquakes: the Loma Prieta main-shock as a test case. *Bull. Seism. Soc. Am.*, **85**, 1144–1160.

- Gallovič, F. and J. Brokešová, 2004: The k^{-2} rupture model parametric study: example of the 1999 Athens earthquake. *Stud. Geophys. Geod.*, **48**, 589–613.
- Gallovič, F. and J. Brokešová, 2007a: Hybrid k-squared Source Model for Strong Ground Motion Simulations: Introduction. *Phys. Earth Planet. Interiors*, **160**, 34–50.
- Gallovič, F. and J. Brokešová, 2007b: Probabilistic Aftershock Hazard Assessment II: Application of Strong Ground Motion Modeling. *submitted to J. Seismology*.
- Gerstenberger, M. C., S. Wiemer, L. M. Jones, and P. A. Reasenber, 2005: Real-time forecasts of tomorrow's earthquakes in California. *Nature*, **435**, 328–331.
- Gottschämmer, E. and K. B. Olsen, 2001: Accuracy of explicit planar free-surface boundary condition implemented in a fourth-order staggered-grid velocity-stress finite-difference scheme. *Bull. Seism. Soc. Am.*, **91**, 617–623.
- Grant, L. B. and P. M. Shearer, 2004: Activity of the offshore Newport - Inglewood Rose Canyon fault zone, coastal Southern California, from relocated microseismicity. *Bull. Seism. Soc. Am.*, **94**, 747–752.
- Graves, R. W., 1996: Simulating seismic wave propagation in 3D elastic media using staggered-grid finite differences. *Bull. Seism. Soc. Am.*, **86**, 1091–1106.
- Graves, R. W. and D. J. Wald, 2001: Resolution analysis of finite fault source inversion using one- and three-dimensional Greens functions 1. Strong motions. *Journal of Geophysical Research*, **106**, 8745–8766.
- Guatteri, M., P. M. Mai, and G. C. Beroza, 2004: A pseudo-dynamic approximation to dynamic rupture models for strong ground motion prediction. *Bull. Seism. Soc. Am.*, **94**, 2051–2063.
- Gupta, I. D. and M. D. Trifunac, 1987: Statistical analysis of response spectra method in earthquake engineering. *Dept Civil Eng, Univ Southern California, Los Angeles CA, Report*.
- Gupta, I. D. and M. D. Trifunac, 1988: A note on computing the contribution of rocking excitation to earthquake response of simple buildings. *Bull Indian Soc Earthq Tech*, **25:2**, 73–89.
- Gupta, I. D. and M. D. Trifunac, 1990: Probabilistic spectrum superposition for response analysis including the effects of soil-structure interaction. *J Probabilistic Eng Mech*, **5**, 9–18.
- Gupta, V. K. and M. D. Trifunac, 1989: Investigation of building response to translational and rotational earthquake excitations. *Dept Civil Eng, Univ Southern California, Los Angeles CA, Report*.
- Gupta, V. K. and M. D. Trifunac, 1991: Effects of ground rocking on dynamic response of multistoried buildings during earthquakes. *Struct Eng/Earthq Eng (JSCE)*, **8:2**, 43–50.
- Gutenberg, R. and C. F. Richter, 1956: Magnitude and energy of earthquakes. *[J]. Ann Geofis*, **9**, 1–15.

- Hanks, T. C. and R. K. McGuire, 1981: The character of high frequency strong ground motion. *Bull. Seism. Soc. Am.*, **71**, 2071–2095.
- Hartzell, S. H., 1978: Earthquake aftershocks as Green's functions. *Geophys. Res. Lett.*, **5**, 1–4.
- Hartzell, S. H. and T. H. Heaton, 1983: Inversion of strong ground motion and teleseismic waveform data for the fault rupture history of the 1979 Imperial Valley, California, earthquake. *Bull. Seism. Soc. Am.*, **73**, 1553–1583.
- Haskell, N. A., 1969: Elastic displacements in the near-field of a propagating fault. *Bull. Seism. Soc. Am.*, **59**, 865–908.
- Hastings, F., J. Schneider, and S. Broschat, 1996: Application of the perfectly matched layer (PML) absorbing boundary condition to elastic wave propagation. *Jour. Acoust. Soc. Am.*, **100**(5), 3061–3069.
- Hauksson, E., 1990: Earthquakes, faulting, and stress in the Los Angeles Basin. *Journal of Geophysical Research*, **95**, 15,365–15,394.
- Hauksson, E. and S. Gross, 1991: Source parameters of the 1933 Long Beach earthquake. *Bull. Seism. Soc. Am.*, **81**, 81–98.
- Heaton, T. H., 1982: The 1971 San Fernando earthquake; a double event? *Bull. Seism. Soc. Am.*, **72**, 2037–2062.
- Herrero, A. and P. Bernard, 1994: A kinematic self-similar rupture process for earthquakes. *Bull. Seism. Soc. Am.*, **84**, 1216 – 1228.
- Housner, G., 1975: Measures of severity of ground shaking, Proceeding of the US National Conference on Earthquake Engineering, Earthquake Engineering Research Institute.
- Hu, Y. X., S. C. Liu, and W. M. Dong, 1996: *Earthquake Engineering*. E & FN SPON.
- Huftile, G. J. and R. S. Yeats, 1995: Convergence rates across a displacement transfer zone in the western Transverse Ranges, Ventura basin, California. *Journal of Geophysical Research*, **100**, 2043–2067.
- Hutchings, L., 1991: “Prediction” of strong ground motion for the 1989 Loma Prieta earthquake using Empirical Green's functions. *Bull. Seism. Soc. Am.*, **81**, 88–121.
- Hutchings, L., 1994: Kinematic earthquake models and synthesized ground motion using Empirical Green's functions. *Bull. Seism. Soc. Am.*, **84**, 1028–1050.
- Hutchings, L. and F. Wu, 1990: Empirical green's functions from small earthquakes — a waveform study of locally recorded aftershocks of the San Fernando earthquake. *Journal of Geophysical Research*, **95**, 1187–1214.
- Idriss, I. M., 1991: Selection of Earthquake Ground Motions at Rock Sites, Report prepared for the Structures Division, Building and Fire Research Laboratory, National Institute of Standards and Technology, Department of Civil Engineering, University of California, Davis.

- Igel, H., P. Mora, and B. Riollet, 1995: Anisotropic wave propagation through finite-difference grids. *Geophysics*, **60**, 1203–1216.
- Igel, H., U. Schreiber, A. Flaws, B. Schuberth, A. Velikoseltsev, and A. Cochard, 2005: Rotational motions induced by the M8.1 Tokachi-oki earthquake, September 25, 2003. *Geophys. Res. Lett.*, **32**.
- Irikura, K., 1983: Semi-empirical estimation of strong ground motions during large earthquakes. *Bull. Disaster Prevention Res. Inst. Kyoto Univ.*, **33**, 63–104.
- Jennings, C. W., 1994: Fault activity map of California and adjacent Areas with location and ages of recent volcanic eruptions. *California Geologic Data Map Series*, **6. California Division of Mines and Geology**.
- Joyner, W. B. and D. M. Boore, 1986: On simulating large earthquakes by Green's-function addition of smaller earthquakes, in *Proceedings of the Fifth Maurice Ewing Symposium on Earthquake Source Mechanics*, S. Das, J. Boatwright, and C. Scholz. *American Geophysical Union*.
- Kanai, K., 1961: An empirical formula for the spectrum of strong earthquake motions. *Bull. Eq. Res. Inst.*, **39**, 85–95.
- Kanamori, H., 1977: The energy release in great earthquakes. *Journal of Geophysical Research*, **82**, 2981 – 2987.
- Karrenbach, M., 1999: Full wave form modeling in complex media: 68th Ann. Internat. Mtg., *Soc. Expl. Geophys.*, **Expanded Abstracts**, 1444–1447.
- Kohler, M., H. Magistrale, and R. Clayton, 2003: Mantle heterogeneities and the SCEC three-dimensional seismic velocity model version 3. *Bull. Seism. Soc. Am.*, **93**, 757–774.
- Larsen, S., R. Reilinger, H. Neugebauer, and W. Strange, 1992: Global Positioning System measurements of deformations associated with the 1987 Superstition Hills earthquake: Evidence for conjugate faulting. *Geophys. Res.*, **97**, 4885 – 4902.
- Levander, A. R., 1988: Fourth-order finite-difference P-SV seismograms. *Geophysics*, **53**, 1425–1436.
- Lisowski, M., J. C. Savage, and W. H. Prescott, 1991: The velocity field along the San Andreas fault in central and southern California. *Journal of Geophysical Research*, **93**, 8369–8389.
- Liu, Q. and J. Tao, 1997: The perfectly matched layer for acoustic waves in absorptive media. *Jour. Acoust. Soc. Am.*, **102**(4), 2072–2082.
- Madariaga, R., 1976: Dynamics of an expanding circular fault. *Bull. Seism. Soc. Am.*, **66**, 163–182.
- Madariaga, R., 1983: High frequency radiation from dynamic earthquake fault models. *Annales Geophysicae*, **1**, 17–23.
- Mai, P. M. and G. C. Beroza, 2000: Source scaling properties from finite-fault rupture models. *Bull. Seism. Soc. Am.*, **90**, 605–614.

- Mai, P. M. and G. C. Beroza, 2002: A spatial random field model to characterize complexity in earthquake slip. *Journal of Geophysical Research*, **107**, no. B11, 2308, doi 10.1029/2001JB000588.
- Marcinkovich, C. and K. B. Olsen, 2003: On the implementation of Perfectly Matched Layers in a 3D fourth-order velocity-stress finite-difference scheme. *Journal of Geophysical Research*, **108**, 2276–2293.
- Marone, C. and C. H. Scholz, 1988: The depth of seismic faulting and the upper transition from stable to unstable slip regimes. *Geophys. Res. Lett.*, **15**, 621–624.
- McLeod, D. P., G. E. Stedman, T. H. Webb, and U. Schreiber, 1998: Comparison of standard and ring laser rotational seismograms. *Bull. Seism. Soc. Am.*, **88**, 1495–1503.
- Milne, W. G. and A. Davenport, 1969: Distribution of earthquake risk in Canada. *Bull. Seism. Soc. Am.*, **59**, 729–754.
- Morton, P. K. and R. V. Miller, 1981: Geologic map of Orange County California, showing mines and mineral deposits. *Calif. Div. Mines Geol. Bull.*, **204**, plate 1.
- Namson, J. S. and T. L. Davis, 1988: Seismically active fold and thrust belt in the San Joaquin Valley, central California. *Geol. Soc. Soc. Amer. Bull.*, **100**, 257–273.
- Newmark, N. M. and H. J. Hall, 1969: Seismic design criteria for nuclear reactor facilities. Proc. Fourth World conf Earthq Engrg. Santiago, Chile.
- Newmark, N. M. and E. Rosenblueth, 1971: Fundamentals of earthquake engineering Prentice-Hall, Englewood Cliffs.
- Nigbor, R. L., 1994: Six-degree-of-freedom ground-motion measurement. *Bull. Seism. Soc. Am.*, **84**, 1665–1669.
- Ohnaka, M. and T. Yamashita, 1989: A cohesive zone model for dynamic shear faulting based on experimentally inferred constitutive relation and strong motion source parameters. *Journal of Geophysical Research*, **94**, 4089–4104.
- Olsen, K. B., 2000: Site amplification in the Los Angeles basin from 3D modeling of ground motion. *Bull. Seism. Soc. Am.*, **90**, S77–S94.
- Olsen, K. B. and R. J. Archuleta, 1996: 3D-simulation of earthquakes in the Los Angeles fault system. *Bull. Seism. Soc. Am.*, **86**, 575–596.
- Quin, H. and S. Das, 1989: A hybrid boundary integral equation method for the computation of source time functions for 3D rupture propagation. *Geophys. J. R. Astr. Soc.*, **96**, 163–177.
- Randall, C. J., 1989: Absorbing boundary condition for the elastic wave equation: velocity-stress formulation. *Geophysics*, **54**, 1141–1152.
- Sadigh, K., C.-Y. Chang, J. A. Egan, F. Makdisi, and R. R. Youngs, 1997: Attenuation relationships for shallow crustal earthquakes based on California strong motion data. *Seismological Research Letters*, **68**, 180–189.

- Sany, R. A., M. W. Cline, C. R. Philipp, D. D. Jackson, Y. Feng, Z.-K. Shen, and M. Lisowski, 1995: Crustal velocity field near the Big Bend of California's San Andreas fault. *Journal of Geophysical Research*.
- Schnabel, P. B. and H. B. Seed, 1973: Accelerations in rock for earthquakes in the western United States. *Bull. Seism. Soc. Am.*, **63**, 501–516.
- Schneider, J. F., W. J. Silva, and C. Stark, 1993: Ground motion model for the 1989 *M*6.9 Loma Prieta earthquake including effects of source, path, and site. *Earthquake Spectra*, **9**, 251–287.
- Scholz, C. H., 1990: *The Mechanics of Earthquakes and Faulting*. Cambridge university press, The Edinburgh Building. Cambridge CB2 2RU, UK.
- Shen, Z., 1991: Regional tectonic deformation in southern California, inferred from terrestrial geodesy and the Global Positioning System, Ph.D. thesis.
- Silva, W. J., 1990: Engineering characterization of earthquake strong ground motions with applications to the Pacific Northwest, in *Proceedings of the Third NEHRP Workshop on Earthquake Hazards in the Puget Sound/Portland Region*, W. Hays (Editor). *U.S. Geol. Surv. Open-File Rept.*
- Somerville, P., 2002: Characterizing Near Fault Ground Motion for the Design and Evaluation of Bridges, Third National Conference and Workshop on Bridges and Highways, Portland, Oregon.
- Somerville, P., M. Sen, and B. Cohee, 1991: Simulations of strong ground motions recorded during the 1985 Michoacan, Mexico and Valparaiso, Chile, earthquakes. *Bull. Seism. Soc. Am.*, **81**, 1–27.
- Somerville, P. G., N. F. Smith, R. W. Graves, and N. A., 1997: Modification of empirical strong ground motion attenuation relations to include the amplitude and duration effects of rupture directivity. *Seism. Res. Lett.*, **68**, 199–222.
- Spillman, W. B., D. R. Huston, and J. Wu, 1998: Very long gauge length fiber optic seismic event detectors. *Proceedings of the SPIE*, **3555**, 311–321.
- Spudich, P. and N. Frazer, 1984: Use of ray theory to calculate high-frequency radiation from earthquake sources having spatially variable rupture velocity and stress drop,. *Bull. Seism. Soc. Am.*, **74**, 2061–2082.
- Spudich, P., L. K. Stek, M. Hellweg, J. B. Fletcher, and L. M. Baker, 1995: Transient stresses at Parkfield, California, produced by the *M* 7.4 Landers earthquake of June 28, 1992: Observations from the UPSAR dense seismograph array. *Journal of Geophysical Research*, **100**, 675–690.
- Stedman, G. E., Z. Li, and H. R. Bilger, 1995: Sideband analysis and seismic detection in a large ring laser. *Applied Optics*, **34**, 5375–5385.
- Takeo, M., 1998: Ground rotational motions recorded in near-source region of earthquakes. *Geophys. Res. Lett.*, **25**, 789–792.

- Teisseyre, R., 2004: Spin and twist motions in a homogeneous elastic continuum and cross-band geometry of fracturing. *Acta Geophys Pol*, **52**, 173–183.
- Virieux, J., 1984: SH wave propagation in heterogeneous media: velocity-stress finite-difference method. *Geophysics*, **49**, 1933–1957.
- Virieux, J., 1986: P-SV wave propagation in heterogeneous media: velocity-stress finite-difference method. *Geophysics*, **51**, 889–901.
- Wald, D. J., D. V. Helmlinger, and T. H. Heaton, 1991: Rupture model of the 1989 Loma Prieta earthquake from the inversion of strong-motion and broadband teleseismic data. *Bull. Seism. Soc. Am.*, **81**, 1540 – 1572.
- Wald, D. J. and P. G. Somerville, 1995: Variable-slip rupture model of the great 1923 Kanto, Japan earthquake; geodetic and body-waveform analysis. *Bull. Seism. Soc. Am.*, **85**, 159–177.
- Weldon, R. and E. Humphreys, 1986: A kinematic model of southern California. *Tectonics*, **5**, 22–48.
- Wells, D. L. and K. J. Coppersmith, 1994: New empirical relationships among magnitude, rupture length, rupture width, rupture area, and surface displacement. *Bull. Seism. Soc. Am.*, **84**, 974–1002.
- Wenerberg, L., 1990: Stochastic summation of Empirical Green’s Functions. *Bull. Seism. Soc. Am.*, **80**, 1418–1432.
- Wössner, J., M. Treml, and F. Wenzel, 2002: Simulation of $M_w = 6.0$ earthquakes in the Upper Rhinegraben using empirical Green functions. *Geophys. J. Int.*, **151**, 487–500.
- Wright, T., 1987: Geologic evolution of the petroleum basins of southern California, in *petroleum geology of coast southern california*, edited by T. Wright and R. Heck. *The Pacific Section American Association of Petroleum Geologists*, **1-20**.
- Yamaguchi, R. and T. Odaka, 1974: Field study of the Izu-Hanto-oki earthquake of 1974. *Special Bull Earthq Res Inst, Univ Tokyo*, **14**, 241–255.
- Yeats, R. S., 2001: *Living with Earthquakes in California*, Oregon State University Press, Corvallis.
- Yomogida, K. and J. T. Etgen, 1993: 3-D wave propagation in the Los Angeles Basin for the Whittier-Narrows earthquake. *Bull. Seism. Soc. Am.*, **83**, 1352–1344.
- Yoshida, S., K. Koketsu, T. Kato, B. Shibazaki, T. Sagiya, and Y. Yoshida, 1996: Joint inversion of near- and far-field waveforms and geodetic data for the rupture process of the 1995 Kobe earthquake. *J. Phys. Earth*, **44**, 437–454.
- Zembaty, Z. and G. Boffi, 1994: Effect of rotational seismic ground motion on dynamic response of slender towers. *Europ Earthquake Engng*, **8**, 3–11.
- Zembaty, Z. B., 2006: Deriving seismic surface rotations for engineering purposes. *Earthquake source Asymmetry Structural Media and Rotation Effects*, Springer Verlag.

- Zeng, Y., J. G. Anderson, and G. Yu, 1994: A composite source model for computing realistic strong ground motion. *Geophys. Res. Lett.*, **21**, 725–728.
- Zeng, Y. and Q. Liu, 2001: A staggered-grid finite-difference method with perfectly matched layers for poroelastic wave equations. *Jour. Acoust. Soc. Am.*, **109**(6), 2571–2580.
- Ziony, J. I. and R. F. Yerkes, 1985: Evaluating of earthquake and surface-faulting potential, in *Evaluating Earthquake Hazards in the Los Angeles Region: An Earth-Science Perspective*, edited by J. I. Ziony, U.S. Geol. Surv. Prof. pap.

Lebenslauf

Persönliche Daten

Name	Wang, Haijiang
Anschrift	LMU-Institut für Geophysik, Theresienstr. 41 80333, München Tel. 0152 0765 9669 Email. haijiang@geophysik.uni-muenchen.de
Geburtsdatum	Juli 3, 1977
Geburstort	Hebei, V.R. CHINA
Familienstand	Ledig
Staatsangehörigkeit	V.R. CHINA

Ausbildung

09.2002 – 2007	Studium an der Ludwig-Maximilians-Universität München, Fakultät für Geowissenschaften, Sektion Geophysik. Titel der Doktorarbeit: Source-dependent variations of M7 earthquakes in the Los Angeles Basin.
09.1999 – 07. 2002	Master studium der Erdbebeningenieurwesen an der Geophysik Institut, China Seismologie Behörde. Thesis title: Attenuation relation of the Diffusive Earthquakes (in Chinese).
09.1995 – 07. 1999	Bachelor studium an der Daqing Erdölinstitut, Fakultät für Erdölerforschung. Thesis title: Using the bore-hole data to inverse the geological tomography (in Chinese).

Schulbildung

09. 1992 – 07. 1995	Gymnasium, Yongnian, Hebei, V.R. CHINA.
09. 1988 – 07. 1992	Grundschule, Yongnian, Hebei, V.R. CHINA.
09. 1983 – 07. 1988	Grundschule, Yongnian, Hebei, V.R. CHINA.